AN ATOMISTIC STUDY OF THE MECHANICAL BEHAVIOR OF

CARBON NANOTUBES AND NANOCOMPOSITE INTERFACES

A Dissertation

by

AMNAYA P. AWASTHI

Submitted to the Office of Graduate Studies of
Texas A&M University
in partial fulfillment of the requirements for the degree of

DOCTOR OF PHILOSOPHY

December 2009

Major Subject: Materials Science and Engineering

AN ATOMISTIC STUDY OF THE MECHANICAL BEHAVIOR OF

CARBON NANOTUBES AND NANOCOMPOSITE INTERFACES

A Dissertation

by

AMNAYA P. AWASTHI

Submitted to the Office of Graduate Studies of
Texas A&M University
in partial fulfillment of the requirements for the degree of

DOCTOR OF PHILOSOPHY

Approved by:

Chair of Committee,	Dimitris C. Lagoudas
Committee Members,	John D. Whitcomb
	Amine A. Benzerga
	Tahir Çağin
Intercollegiate Faculty Chair,	Tahir Çağin

December 2009

Major Subject: Materials Science and Engineering

ABSTRACT

An Atomistic Study of the Mechanical Behavior of

Carbon Nanotubes and Nanocomposite Interfaces. (December 2009)

Amnaya P. Awasthi, B.Tech. , Indian Institute of Technology, Guwahati, India

Chair of Advisory Committee: Dr. Dimitris C. Lagoudas

The research presented in this dissertation pertains to the evaluation of stiffness of carbon nanotubes (CNTs) in a multiscale framework and modeling of the interfacial mechanical behavior in CNT-polymer nanocomposites. The goal is to study the mechanical behavior of CNTs and CNT-polymer interfaces at the atomic level and to utilize this information to develop predictive capabilities of material behavior at the macroscale. Stiffness of CNTs is analyzed through quantum mechanical (QM) calculations while the CNT-polymer interface is examined using molecular dynamics (MD) simulations. CNT-polymer-matrix composites exhibit promising properties as structural materials and constitutive models are sought to predict their macroscale behavior. The reliability of determining the homogenized response of such materials depends upon the ability to capture accurately the interfacial behavior between the nanotubes and the polymer matrix. In the proposed work, atomistic methods are used to investigate the behavior of the interface by utilizing appropriately chosen atomistic representative volume elements (RVEs). Atomistic simulations are conducted on the RVEs to study mechanical separation with and without covalent functionalization between the polymeric matrix and two filler materials, namely graphite and a (12,0) Single Wall zig zag CNT. The information obtained from atomistic studies of separation is applicable for higher level length scale models as cohesive zone properties. The results of the present research have been correlated with available experimental data from characterization efforts.

To The Invisible, that manifests as Parents who nourish,

The Guru who shows the path and Knowledge that seeks discovery.

ACKNOWLEDGMENTS

First and foremost, I would like to acknowledge my advisor Prof. Dimitris C. Lagoudas who played the most vital role in developing me both personally as well as professionally. His continued guidance has been the indispensable ingredient of this research, both in developing the technical merit as well as scientific maturity. His mentorship has progressed me into learning the art of scientific discovery through patient persistence and steady progress. It was a unique experience to work with him and looking back on the whole track of the doctoral program, I feel that it was an honor to be part of his group and learn science under his guidance.

I thank my committee members, Drs. Amine A. Benzerga, John D. Whitcomb and Tahir Çağin for helping me progress by providing me inputs from perspective of different disciplines, ranging from discrete modeling at the atomistic scale up to continuum issues at the macroscale. I am deeply thankful to Dr. Lisa Pérez, Manager, Laboratory of Molecular Simulations (LMS) at Texas A&M University for helping in getting trained in performing molecular simulations and being always available selflessly, as a backbone of support, especially in critical times.

I am indebted to Dr. Daniel C. Hammerand, whose continued interaction during research meetings contributed significant grounds in the development of this research and my progress in personal and professional maturity. The help of Drs. Eun-Suok Oh and George Chatzigeorgiou was not just indispensable in the production of manuscripts – their inclination for technical help and discussions for improvements was an experience worth learning. Interactions with Dr. Sarah J. Frankland were extremely useful in understanding the art of molecular simulation especially during long discussions both in person as well as on email, were substantially contributive

in understanding of the subject matter.

My area of molecular simulation used to be the topic of active discussion amongst the founder members of the nano group, namely my colleagues Piyush Thakre and Dr. Gary D. Seidel. Not just discussions on technical topics, we spent some unforgettable moments in our offices discussing philosophy, culture and life in general. Piyush and I underwent extended hours of discussing different aspects of Indian culture and philosophy. Piyush and his wife Abhidha are the most handsome couple I've ever met. I highly commend Gary and his wife Bridget for helping the international students like me get closely involved with the international student community. As real Aggie, Gary gave a lot of vision to the nano group and his brainstorming on technical matters, in organizing meetings, preparing reports and presentations for conferences will always be acknowledged. I will always remember Aggieland for my roommate Dr. Piyush Goel, with whom I would forget the passage of time and hours of long discussions would sweep by like minutes.

I want to thank Olivier Bertacchini for extending his help during critical times and Darren Hartl, Brent Volk and Parikshith Kumar for being the source of spirit and motivation in our group. Interactions with Krishnendu Haldar have played an important role in reinforcing the objective of human life in the spiritual context. Francis Phillips has been a very patient learner and I wish him the very best in his professional career.

I extend my gratitude to Dr. K. Srinivasan, professor, mechanical engineering at Indian Institute of Technology (IIT), Guwahati for introducing me to nanotechnology and Dr. Saikat Ray, my friend at IIT who motivated me into performing doctoral research. I want to express sincere gratefulness to Dr. Milind Kulkarni and Mrs. Manasi Kulkarni who have fueled my spirit into active performance during difficult times.

I have also been fortunate to be involved with the Indian community in the Brazos

Valley, which played a major role in my growth and development. In particular I want to thank Mrs. Shobhana and Dr. Mahendra Thakrar who treated me like their own son, Mrs. Jashmina and Mr. Jagdish Bhai Patel who were more than a family and Dr. Hari Dhar who was my meditation guru. I thank Dr. S. Girimaji, Dr. N. K. Anand and Dr. M. M. Rao for instilling motivation, discipline and regard for higher ideals of life.

Texas A&M University has been a unique place of experiencing growth. I want to thank the management, especially the leaders who have upheld quality education through improved advising, leadership values and state of the art facilities. I wish this university the best in attaining the 2020 vision in full glory. I am fortunate to have met some great friends here, namely Mariana Ceballos, Rohit Saha, Priyanka Doshy, Parijat Sinha, Lakshminarasimhan Krishnan, Pudhuma Karunakaran and Mayank Lal who have stood by me selflessly in times of need and support. There have been countless significant people who have helped in shaping my life's journey here in Aggieland and some have played such an important role that it is hard to remember their contribution. I pledge them with silent acknowledgement.

The current work would have not been possible without the sacrifices of my family – mother, Dr. Prema Awasthi, father, Late Dr. Daya Shankar Shastri and sisters Suvijna and Upajna who encouraged me during difficult times and upheld my spirits inexhaustibly during all climates, helping me emerge successful. These are the pillars whom I will always look up as ideals.

Amnaya P. Awasthi

College Station, TX.

TABLE OF CONTENTS

LIST OF TABLES

LIST OF FIGURES

CHAPTER I

INTRODUCTION

A.   Carbon nanotubes

Carbon nanotubes (CNTs) are energetically stable structures idealized as rolled-up cylindrical sheets of graphene and exist as single walled (SWCNTs), multiwalled (MWCNTs) and ropes [1]. Information about the nature of chemical bonding in the carbon nanotubes reflects that these structures should have high stiffness, as evident from a few experimental observations [2–5] and theoretical modeling efforts [6].

Several efforts have focused on the theoretical modeling of SWCNTs as an equivalent continuum, in order to reduce computational cost incurred in atomistic simulations. Arroyo and Belytschko [7] modeled the SWCNT as a continuum hyper-elastic membrane using crystal lattice dynamics and transitioning stiffness of atomistic bonds from atomistic potentials to the continuum level. The elastic properties of SWCNTs have been evaluated using thermodynamics and continuum stress deformation behavior, [8] using the Tersoff-Brenner (TB) potential. Meo and Rossi [9] investigated the influence of tube diameter and chirality of SWCNTs on the Young's modulus of SWCNTs by modeling the carbon-carbon bond using finite elements with stiffnesses derived from the TB potential.

The structural stiffness of SWCNTs has been obtained using the second derivative of strain energy. The energy based method (as it will be referred in the present work) has been used together with quantum mechanical calculations in obtaining the Young's modulus for a SWCNT[10–12], where the SWCNT was subjected to axial tension and compression. The energy, interpreted as strain energy was evaluated for

_____

The journal model is *IEEE Transactions on Automatic Control.*

each deformation by a quantum mechanical theory.

Central to the procedure in obtaining stiffness of CNTs through the energy method is the evaluation of the second derivative of the strain energy of the structure with respect to strain. To evaluate the second derivative for atomistic systems, the technique employs evaluation of the minimum energy structure (optimized structure) as the starting point. The structure is then axially stretched under small deformations, both in tension as well as in compression, and the energy for each stretched state is recorded. From the plot of energy versus strain in the vicinity of zero strain, the second derivative is obtained by performing a curve fit of the energy-strain profile. The Young's modulus has been evaluated by assuming a cross sectional thickness of the SWCNT over which the axial forces were assumed to be applied. In this procedure the energy is computed at each stretched state after structural optimization and the optimization step is repeated for the several number of points needed on the energy-strain plot.

The energy based method has also been utilized with molecular mechanics methods that employ force-fields to model interatomic interactions. In the research by Odegard et al. [13] and Li and Chou, [14] the bonds between carbon atoms in a SWCNT were replaced by equivalent trusses and the resulting truss structure was utilized to evaluate the Young's modulus through the energy approach. This method of using the equivalent truss structure has been used to further evaluate torsional and bending rigidities of CNTs [15] and observe sensitivity to temperature effects [16].

B. Carbon nanotube polymer composites

Polymer nanocomposites have been known to exhibit enhancements in mechanical, thermal, electrical and magnetic properties with respect to neat polymer [17]. They

have found potential applications as structural materials in the aerospace [18] and automotive [19] industries, and as sensors, actuators and optical components in the electronics [20] industry. The enhancement in properties exhibited by the polymer nanocomposites is mainly governed by two factors: the properties of the constituent phases and the interfacial interactions between the filler and the matrix. Usually the properties of the matrix phase are known, but those of the nanoscale filler and that of the interface between the filler and matrix are difficult to assess, due to experimental limitations in probing material behavior at the nanoscale. The interfacial behavior is mainly governed by atomistic level interactions and therefore atomistic simulations can potentially provide information about the interfacial interactions. However, the theoretical prediction of bulk behavior in nanocomposites relies not only on the availability of the nanoscale interfacial information but also on adequate incorporation of this information into continuum level modeling.

CNT polymer nanocomposites have gained immense popularity in the past decade for structural applications due to the stable structure and high stiffness of CNTs [21, 22]. Several methods for fabricating CNT-polymer nanocomposites have been developed [23] and the effect of modifying the interface between the CNTs and polymer has been studied using different chemical functional groups [24–28]. The mechanical response of these materials has been investigated using several techniques including Dynamical Mechanical Analysis (DMA) [27], Raman micromechanical test [29] and nanoindentation [30]. Lately, CNTs have been used in carbon fiber fabric composites [31] and efforts have been made to assess the shear strength of CNT fabric composites experimentally [32].

To evaluate the bulk mechanical response of the CNT-polymer system, atomistic simulations have been performed by many investigators. Odegard et al [13] evaluated effective mechanical properties of CNT-polymer composites by performing energy

equivalence between atomistic and continuum models. In [33], [34], [35] and [36] the stress-strain behavior of CNT-polymer composite was studied, by deforming the computational domain and evaluating the average mechanical response. In the work by Jeff Hinkley and coworkers[37] the stress-strain behavior of CNTs embedded in a polymer matrix was studied over different loading rates and temperatures. These simulations, which mainly modeled the bulk response have shown that the addition of CNTs results in increasing the stiffness of the system compared to neat polymer. However, atomistic models predicting overall response of the composite system do not provide information about the interfacial behavior with respect to separation.

C. Interfacial properties of CNT polymer nanocomposites

Atomistic simulations for the interfacial behavior between the CNT and polymer have shown that the surface of CNTs is highly attractive and causes the polymer to attain higher density near the interface [38]. The strength of the interface between the CNT and polymeric matrix has been determined by evaluating the work of adhesion [39, 40] as the energy required to completely separate the CNT from the influence of the polymer [41]. To evaluate the shear strength of the interface, pullout tests have been performed using atomistic simulations [42–46]. These pullout tests have provided the force versus displacement response [47, 48] during separation and parameters like the threshold shear stress to cause separation, and critical length of nanotube for significant load transfer [49, 50] have been evaluated. Information from the pullout tests have further been incorporated into higher scale modeling as shear characteristics of the interface [48, 51]. These atomistic studies for separation have mainly dealt with separation in the shear (sliding) mode within the framework of pull out tests, and have not investigated normal (opening) separation. Moreover, separation under combined

loading has not been investigated using atomistic methods for CNT polymer systems.

Cohesive laws of separation have been evaluated for graphene planes using the Van der Waals potential, and extended to multi-walled CNTs by incorporating curvature effects [52]. These laws were evaluated for both opening as well as sliding modes of separation for both finite-sized as well as infinite planes of graphene and infinitely long CNTs. Van der Waals based cohesive laws have also been evaluated for CNT-polymer systems [53, 54], wherein both the CNT as well as the polymer were assumed to be rigid. These studies were based on static atomistic structures of CNT and polymer, and the effects of atomic motion near the interface were not incorporated.

Research for the graphite-polymer system has shown that atomisitic simulations can provide information about structural [55, 56], conformational [57] and mobility [58, 59] characteristics of the polymer interacting with stationary layer(s) of graphite, which has surface morphology similar to CNTs. However, information about separation, where the graphite layers displace relative to the matrix, has been limited only to the evaluation of work of adhesion [60]. Studies of separation providing force versus displacement behavior for the graphite-polymer system have not been reported using atomistic methods.

Evaluation of interfacial characteristics for the CNT-polymer or graphite-polymer systems using experimental methods is also available, but limited in number due to difficulties in accessing individual interfaces. Efforts have been made to conduct pull out tests of multi walled CNTs (MWCNT) through polymer using scanning probe microscopy (SPM) [61] and conducting tensile tests of MWCNT-polymer thin films and characterizing using *in-situ* transmission electron microscopy (TEM) [62, 63]. Real time observations of the nanoscale phenomena of the separation process provided information about the maximum force needed to pull out CNTs from the matrix, shear

strength of the interface and energy needed to pull out the CNTs through the matrix.

Atomistic simulations have been performed to evaluate the interfacial behavior in crystalline, mostly metallic solids, e.g., for copper [64] and aluminum [65]. The information from atomistic simulations is utilized as separation laws for continuum scale cohesive zone models. Cohesive zone models developed by Dugdale [66] and Barenblatt [67] assume a generic relationship between forces and displacements occurring at the interface during separation. The models have been further elaborated and used by Needleman [68], Ortiz [69] and Tvergaard [70] to study interface debonding, microcracking and fiber pull out tests. Incorporation of atomistically-evaluated cohesive law into these models provides specific interfacial behavior for the chosen material system. Atomistic simulations for metals are lesser complex compared to polymeric systems, because they are based on the crystal lattice and the nature of metallic bonding allows the interactions to be represented by a pair potential which is computationally less demanding. In contrast, for polymeric systems, the amorphous structure brings in additional complication in modeling the polymer structure, and the interatomic potential that accounts for covalent bonding is more complex than metallic systems.

The current state of the art in modeling mechanical behavior of CNT polymer nanocomposites with interface effects is limited, in that, interfacial behavior through atomistic simulations is not available for general loading i.e., beyond pull-out tests, which corresponds to shearing loads. Moreover, simulations that consider combined loading behavior [13, 33, 34] mainly model the effective response of the composite, and therefore do not explicitly provide interfacial behavior for separation. Finally, micromechanical models, which predict effective response of nanocomposites, assume the interface to be fully or partially bonded [71–73], or use results from the available pullout tests [47].

D.   Objectives of present research and significance

The research presented in this dissertation pertains to the evaluation of mechanical properties of CNTs and investigation of interfacial behavior for load transfer for CNT polymer nanocomposites. The mechanical properties of CNTs have been studied using quantum level computations, and central to the present investigation is the development of a multiscale approach, called the atomistic Hessian matrix method. The objective is to obtain elastic stiffness of nanoscale material systems using quantum mechanical tools better computational efficiency and higher accuracy, compared to existing multiscale methods. The interfacial behavior in CNT polymer nanocomposites was evaluated using molecular dynamics (MD) methods, employing the classical force field Consistent Valence Force Field (CVFF) as well as the reactive force field ReaxFF. MD simulations were performed for different loading conditions to examine the interfacial behavior for both non-bonded as well as interfacially bonded systems. Additionally, the mechanical response of the interface was evaluated for both straight chain amorphous polymer as well as network polymer.

Interfacial studies of SWCNT pull out from polymer were performed to examine the traction separation response of the interface and observe parameters like the peak shear traction and energy of separation. These studies were extended to a more general framework, to examine the interfacial behavior for a representative structure of graphene and polymer where separation was studied as a combination of both sliding as well as normal modes. Studies were also made to evaluate the effect of tension and compression on sliding mode separation, thereby obtaining the response for combined loading. Efforts were made to assess the effects of differences in application of boundary conditions on the force-separation response of the molecular representative volume element (RVE). Investigation is also undertaken to determine the minimum

RVE needed in obtaining cohesive zone parameters namely peak traction and work of separation that tend to be independent of the size of computational window. This is an effort towards determining the interfacial constitutive behavior for CNT-polymer interfaces, which can be utilized in higher scale modeling after appropriate transitions incorporating curvature and waviness of the CNTs. The separation behavior will be made applicable to higher scale micromechanical models in the form of separation laws within a cohesive zone modeling framework. It is for the first time that MD simulations incorporating atomistic motion have been performed for opening and sliding separation along with combined loading for the graphene-polymer system to evaluate interfacial load-displacement behavior.

E.   Dissertation outline

Chapter II contains a description of tools required to perform atomistic studies at the nanoscale. Chapter III describes the atomistic Hessian matrix method and its application in obtaining elastic stiffness of SWCNTs with numerical examples for determination of linear elastic stiffness in extension and torsion using the atomistic Hessian method. The chapter describes the determination of the atomistic Hessian matrix using experimental data and comparison with that derived from *ab initio* and molecular statics methods. Chapter IV describes studies of interfacial behavior of SWCNT pull out from polymer matrix using molecular dynamics and Chapter V describes atomistic studies performed to investigate the mechanical behavior of the graphene polymer interface using molecular dynamics.

CHAPTER II

TOOLS FOR INVESTIGATING MATERIAL BEHAVIOR AT THE NANOSCALE

A.   Atomistic methods to evaluate material behavior at the nanoscale

1.   *ab-initio* methods

The *ab-initio* methods are computational chemistry based methods that are based on the fundamental laws of quantum mechanics and use approximation techniques to solve the fundamental equations [74–76]. In these methods, the electrons are assumed to possess wave nature and are therefore their behavior is modeled using the Schrödinger wave equation. Solving the Schrödinger wave equation provides many physical properties of the atomistic system, including the energy states on which the electrons exist. The behavior of the nuclei is governed by the Born Oppenheimer approximation which separates the motion of the electrons with that of the nuclei, since the nuclei are several orders of magnitude larger than the electrons. The nuclei are assumed to possess particulate nature.

Solving the Schrödinger wave equation gives the potential energy surface generated by electrons in a field of fixed nuclei. The nuclei move on this potential energy surface and this describes vibrational, translational and rotational states of the nuclei. The *ab-initio* methods are computationally very intensive, and can be used to simulate only up to 500 atoms. In the present research, the *ab-initio* method called the Hartree Fock (HF) method has been used.

2.   Molecular mechanics

Molecular mechanics treats every atom as a point mass and interactions between them are described through a potential field, known as a force field. A force field
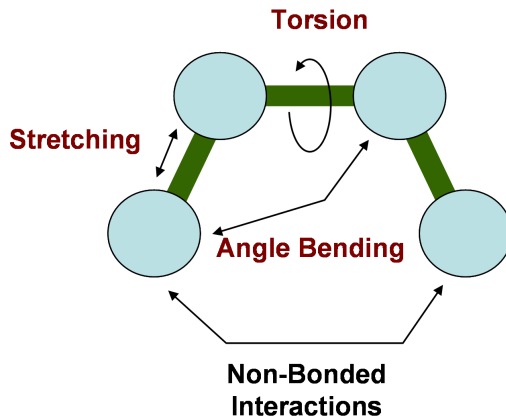
Fig. 1.: Components of the force field employed in MD simulations.

is a set of parameters describing the interactions between the atoms which are obtained either using experiments or *ab-initio* calculations [75] and are interpreted as springs. The behavior of the atomistic system is then described by Newtons law, by which static equilibrium can be studied (molecular statics) or incorporating motion, the dynamic behavior can be analyzed (molecular dynamics). Molecular mechanics facilitates simulation of larger number of atoms and the behavior of up to a billion atoms can be computed, using parallel computation architectures.

a.   Classical force-fields

Classical force-fields are parametric representations of interatomic bonds that do not have the capability for bond-dissipation or bond-formation. These force-fields contain parameters describing covalent bond as a collection of different stiffnesses which are shown in Fig. 1.

The Consistent Valence Force Field (CVFF) potential [77] employed for modeling the interactions between atoms in the current study, consists of the following energy components (Fig. 1):

Bond stretching potential: This portion of the force-field models the stretch between two atoms that are covalently bonded. The expression for the bond-stretching energy is given as

$$E_B = \sum_{i=1}^{n_B} K_B^{(i)} \big(r^{(i)} - r_0^{(i)}\big)^2 \tag{2.1}$$

where $r^{(i)}$ denotes the separation between the atoms constituting the ith covalent bond, $r_0^{(i)}$ denotes the equilibrium separation, $K_B^{(i)}$ represents the stiffness of the ith bond and n_B is the total number of covalent bonds.

Angle bending potential: This component models the stiffness of the angle formed by two covalent bonds of three adjacent atoms. The expression for the angle bending energy is given as

$$E_A = \sum_{i=1}^{n_A} K_A^{(i)} \big(\theta^{(i)} - \theta_0^{(i)}\big)^2 \tag{2.2}$$

where $\theta^{(i)}$ is the angle between the ith pair of adjacent covalent bonds which is $\theta_0^{(i)}$ at equilibrium, $K_B^{(i)}$ is the angular stiffness of the ith covalent bond and n_A is the total number covalent bond pairs.

Torsional rotation potential: This term models the stiffness of the angle formed between four adjacent atoms that are covalently connected. The torsional angle is also known as the *dihedral*. The expression for the torsional (dihedral) potential is given as

$$E_T = \sum_{i=1}^{n_T} K_T^{(i)} \big[1 + d^{(i)} \cos n^{(i)} \big(\phi^{(i)} - \phi_0^{(i)}\big)\big] \tag{2.3}$$

where $\phi^{(i)}$ is the torsion angle between the planes formed by first-second and second-third adjacent bonds for which $\phi_0^{(i)}$ is the equilibrium value. $K_T^{(i)}$ is the torsional stiffness of the ith covalent bond, $d^{(i)}$ and $n^{(i)}$ are integers parameterized for specific atomistic systems and n_T is the total number of torsional angles in the system.

Non-bonded (pair) potentials: The non-bond potentials employed for this study are pair potentials acting between two non covalently bonded atoms. The range of inter-

action for the non-bond potentials is dictated by the cut-off distance, beyond which these potentials are switched off to zero. The non-bonded energy comprises of the Van der Waals potential and the electrostatic potential.

Van der Waals pair potential: The expression for energy associated with atoms connected with Van der Waals interactions is given as

$$E_{P_V} = \frac{1}{2} \sum_{i=1, j \neq i}^{N} \left[\frac{A_{ij}}{r_{ij}^{12}} - \frac{B_{ij}}{r_{ij}^6} \right] \tag{2.4}$$

where r_{ij} is the distance between the two atoms, N is the total number of atoms in the atomistic system, $A_{ij} = \sqrt{A_i A_j}$ and $B_{ij} = \sqrt{B_i B_j}$, and A and B are parameters for different atom types given by the subscripts i and j.

Electrostatic pair potential: The electrostatic pair potential also known as the Coulombic interaction between a pair of charged atoms is given as

$$E_{P_C} = \frac{1}{2} \sum_{i=1, j \neq i}^{N} \frac{1}{4 \pi \epsilon_0} \frac{q_i q_j}{r_{ij}} \tag{2.5}$$

where r is the distance between two atoms i and j, q_i and q_j are the partial charges on the atoms i and j respectively, ϵ_0 is the permittivity of free space, and N is the total number of atoms in the atomistic system. The factor of $\frac{1}{2}$ is introduced in both the pair potentials to eliminate double counting of pair energies.

The complete potential is represented by the sum of all the components as

$$E = E_B + E_A + E_T + E_{P_V} + E_{P_C} \tag{2.6}$$

The parameters in CVFF used to represent interactions between constituent atoms used in the present work are given in table on page 150.

b.   Reactive force-fields

Traditional force fields do not have the capability to break or create bonds and during a simulation with the traditional force fields, an atomic bond stretch infinitely if the atoms are separated. Reactive force fields have been developed to overcome this limitation such that atomistic properties can be predicted more reasonably without having to perform computationally intensive quantum level computations.

The Tersoff Brenner Potential [78, 79], the Reactive Empirical Bond Order (REBO) [80] and the ReaxFF [81] are the commonly used reactive potentials in the literature. In the present work, the ReaxFF is used to model the interfacial behavior in carbon nanotube polymer systems. The ReaxFF potential can model the breaking and formation of chemical bonds depending on the correct energetics of the system and proximity of atoms.

Many investigations of CNT polymer interaction have been performed [47, 49, 82, 83] using the Tersoff Brenner (TB) potential. The TB potential has been extensively used for CNT, and CNT polymer systems as it was parameterized for hydrocarbons. This potential predicts the equilibrated structure of the nanosystem well, however it does not contain the appropriate information to model bond breaking and formation. Additionally, the TB potential does not include non-bonded interactions (which act in the long range) like Van der Waals and Coulombic interactions and for each of these studies, an additional Lennard-Jones term was added to the TB potential to incorporte the long range effects.

The reactive force field ReaxFF [81] is a recent advancement in the development of atomistic potentials which includes both, long range interaction as well description about bond breaking and formation. The reaction parameters in ReaxFF have been obtained using quantum level *ab initio* calculations. At the present time, ReaxFF

has been parameterized for mainly hydrocarbons and provides accurate hydrocarbon bond dissociation and reaction information. While the TB potential would cause a bond to break sharply, the ReaxFF on the other hand would model the bond breaking event much smoother, consistent with ab initio calculations. In the current work, the functional form of the potential is used as described in the supplemental material in the paper [84].

3. Numerical Integration

The total energy of the complete atomistic system, incorporating contributions from all atoms, is a function of positional coordinates of atoms, represented as

$$E = E(\mathbf{r}^{(1)}, \mathbf{r}^{(2)}, \mathbf{r}^{(3)} \ldots \mathbf{r}^{(N)}) \tag{2.7}$$

The expression for the potential energy is utilized to evaluate the total force on each atom

$$\mathbf{F}^{(i)} = -\nabla_{\mathbf{r}^{(i)}} E = F(\mathbf{r}^{(1)}, \mathbf{r}^{(2)}, \mathbf{r}^{(3)} \ldots \mathbf{r}^{(N)}) \qquad i = 1, 2, \ldots, N \tag{2.8}$$

Given the coordinates of the atoms, both the total energy as well as the force on individual atoms can be evaluated. The acceleration of an atom is evaluated by Newton's law as:

$$\mathbf{a}^i = \ddot{\mathbf{r}}^i = \frac{\mathbf{F}^i}{m^i} \tag{2.9}$$

where m^i is the mass of the ith atom. These are a set of $3N$ second order ordinary differential equations and are integrated in time using the velocity-Verlet integration algorithm [85] given as follows:

At a given time instant t, represented by the nth time step of uniform duration h such that $t = nh$, the velocity and accelerations can be approximated using the central

difference scheme as:

$$\mathbf{v}_n^i = \dot{\mathbf{r}_n^i} \approx \frac{1}{2h} \left(\mathbf{r}_{n+1}^i - \mathbf{r}_{n-1}^i \right) \tag{2.10}$$

$$\mathbf{a}_n^i = \ddot{\mathbf{r}^i} = \frac{\mathbf{F}_n^i}{m^i} \approx \frac{1}{h^2} \left(\mathbf{r}_{n+1}^i - 2\mathbf{r}_n^i + \mathbf{r}_{n-1}^i \right) \tag{2.11}$$

Treating the expressions as equality, they can be rearranged to give:

$$\mathbf{r}_{n+1}^i = \mathbf{r}_n^i + h\mathbf{v}_n^i + \frac{h^2}{2} \frac{\mathbf{F}_n^i}{m^i} \tag{2.12}$$

$$\mathbf{v}_{n+1}^i = \mathbf{v}_n^i + \frac{h}{2} \left(\frac{\mathbf{F}_{n+1}^i}{m^i} + \frac{\mathbf{F}_n^i}{m^i} \right) \tag{2.13}$$

At the beginning of the MD simulation, the positions and velocities of all the atoms are known (initial conditions: $\mathbf{r}_0^i$, $\mathbf{v}_0^i$, $i = 1 \dots N$) and the information of positions ($\mathbf{r}_0^i$) allows the evaluation of acceleration for all atoms using Eq. 2.9 ($\mathbf{a}_0^i$, $i = 1 \dots N$). The positions of atoms at the next time step ($\mathbf{r}_1^i$) are evaluated using Eq. 2.12. With the new positions of atoms, Eq. 2.9 is used to calculate accelerations on all the atoms ($\mathbf{a}_1^i$) and Eq. 2.13 gives the velocities ($\mathbf{v}_1^i$) of all atoms at the next time step. In this way, the updated positions, velocities and accelerations are used to evaluate these quantities at the next time step. This procedure is carried out for the length of the simulation.

B.   Atomistic analysis of mechanical properties of polymers

The need for investigating interface properties using atomistics is defined by their applicability to continuum scale models. This exercise of evaluating macro scale properties using nanoscale attributes has been done mostly for calculating bulk properties of polymer using MD. To evaluate the bulk mechanical properties of a polymer, several methods are available in literature as shown in Fig. 2. The molecular statics method [86–88], consists of equilibrations (energy minimization) at incremental load

application, and eventually studying the load-response profile. These simulations disregard contributions due to thermal vibrations of the constituent atoms. Molecular dynamics methods [37, 89] on the other hand, incorporate the thermal contributions. The deformation can be applied in stepwise fashion [37] or by constant strain rate [89]. The united atom method, also known as the coarse grained method [90, 91] utilizes a simplified potential so that large system volumes can be simulated. Monte Carlo methods for evaluation of polymer bulk properties [92–94] simulate the material behavior in two steps. At the first step, molecular statics is used to investigate processes or events causing material response to loading. At the next step, the information from molecular statics is used to prepare a Monte Carlo (MC) model, where the evolution of these events is represented over Monte Carlo steps.

Molecular Dynamics

•Full Force Field
•Velocity
•Time (in ps)
•System evolution based on Newton's laws
•Limited by space

Step-wise relaxation

Qi, Hinkley and He (2005)

Imposition of constant strain rate

Yashiro, Ito and Tomita (2003)

Molecular Statics

•Full Force Field
•No velocity
•No time
•No evolution
•Limited by space

Theodorou and Suter (1986)

Coarse Grained Method

•Reduced Force Field
•Velocity
•Time (in reduced units)
•System evolution based on Newton's laws
•Not limited by space

Brown and Clarke (1991)

Monte Carlo (MC) Methods

•Two step method – atomistic + MC
•Full Force Field in Atomistic part
•In MC part, system-evolution based on probability of event occurrence
•No velocity in MC
•No time in MC
•Not limited by space
•Requires pre-determined info about atomistic events (from MD)

Mott, Argon and Suter 1993

Fig. 2.: Different approaches used in literature to model mechanical properties of polymers.

CHAPTER III

EVALUATION OF MECHANICAL PROPERTIES OF SINGLE WALL CARBON

NANOTUBES*

This chapter describes the development of a method, termed as the atomistic Hessian matrix method to evaluate mechanical stiffness of nanoscale material systems. Central to this method is the utilization of the atomistic Hessian matrix evaluated using an appropriate potential. As an example, evaluating the atomistic Hessian matrix using the Hartree Fock method, this method is demonstrated for SWCNTs, where the linear elastic stiffness in extension and torsion are evaluated. Additionally, components of the atomistic Hessian matrix evaluated using the Hartree Fock method and molecular mechanics methods are compared with those obtained using experimental information.

The current work describes an alternate method for obtaining the stiffness of the SWCNT near equilibrium in a way that the discrete character is retained and at the same time computationally intensive atomistic simulations are performed only once. The method discussed in this chapter utilizes the atomistic Hessian matrix, defined as the second derivative of energy with respect to atomic displacements, to evaluate the linear response of SWCNTs for prescribed loading conditions and subsequent evaluation of structural moduli. The atomistic Hessian was evaluated using frequency calculations performed on SWCNTs using the Hartree Fock quantum mechanical method. The atomistic Hessian matrix was also evaluated analytically using

molecular mechanical calculations through the second derivative of the strain energy using the TB potential. The components of the atomistic Hessian matrix evaluated using *ab initio* calculations and TB potential were compared with experimentally obtained force-constants. Additionally, quantum mechanical calculations were performed to examine the effect of longitudinal strain on the frequency characteristics of SWCNT.

A.   The atomistic Hessian matrix

This section contains description of the atomistic Hessian matrix and its significance in theoretical chemistry. Next, a method to evaluate structural stiffness of a material system at the nanoscale is presented, where the atomistic Hessian matrix is utilized as the key component.

1.   Definition of the atomistic Hessian matrix

Consider a set of N interacting atoms in static equilibrium and the potential energy of the system be represented by $\Phi(u_i^p)$, where u_i^p is the ith component of displacement of the pth atom, where $p = 1 \ldots N$ and $i = 1 \ldots 3$. The components of displacements are defined relative to static equilibrium at which the potential energy is a minimum. The atomistic Hessian matrix $[\mathsf{K}]$ is the matrix of second derivatives of the potential energy with respect to atomistic displacements, and the components are given as

$$[\mathsf{K}]_{ij}^{pq} = \left. \frac{\partial^2 \Phi}{\partial u_i^p \partial u_j^q} \right|_{u_i^p = 0, \ u_j^q = 0} , \tag{3.1}$$

where $i, j = 1 \ldots 3$ and $p, q = 1 \ldots N$. The atomistic Hessian matrix for a system of N atoms is a symmetric matrix of order $3N$.

The atomistic Hessian matrix can be diagonalized to give eigenvalues and eigen-

vectors which physically represent natural frequencies and modal shapes of vibration of the constituent atoms. There are $3N-5$ non-zero natural frequencies (and mode shapes) for a system containing linear chain of atoms and and $3N-6$ those for a system with general configuration of atoms. This is because there are respectively 5 and 6 rigid body modes for linearly and non-linearly oriented sets of atoms, describing translation and rotation of the system as a whole, characterized by zero natural frequencies. If all the eigenvalues of the atomistic Hessian matrix are positive, the system is interpreted to be stable, while negative eigenvalues pertain to transition states. In theoretical chemistry, the study of eigenvectors of transition states, characterized by negative eigenvalues is significant [95], as it provides predictability for chemical reactions.

Typically, the atomistic Hessian matrix is evaluated for the determination of a minimum energy configuration of a set of atoms and the eigenvalues and eigenvectors are obtained through a procedure of diagonalization [96]. Moreover, given the complete set of frequencies and mode shapes for a particular atomistic system, the atomistic Hessian matrix can be evaluated using modal synthesis, as described in Appendix A. The components of the atomistic Hessian matrix are force constants representing linear spring-like interactions between pairs of atoms.

2.   Force-displacement behavior using the atomistic Hessian matrix

The atomistic Hessian matrix given by eq. 3.1 consists of force constants representing pair-wise interaction between pairs of atoms in the atomistic system. Fig. 3 shows how the atomistic Hessian matrix can be used to establish a corresponding spring mass system for a SWCNT, where every atom is connected to every other atom by a linear spring. The strength of interactions between pairs of atoms is represented by the magnitude of the corresponding components of the atomistic Hessian matrix.
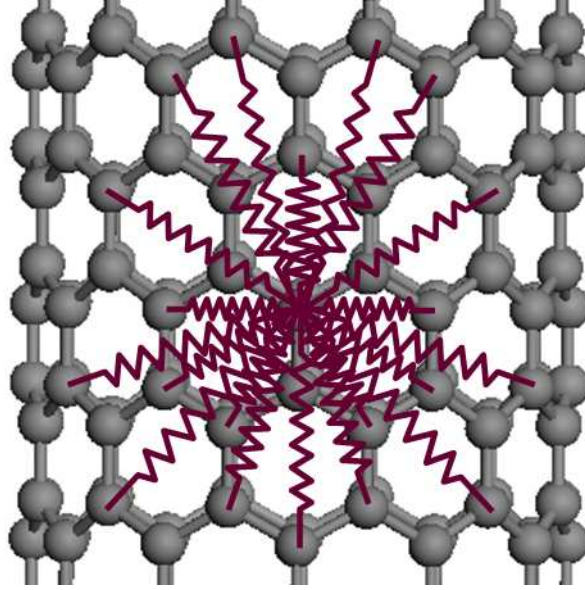
Fig. 3.: The atomistic Hessian matrix represents a system of point masses interconnected by linear springs.

With this equivalence, the atomistic Hessian matrix can also be used to write the equation of motion for a linear system containing atoms represented by point masses, given as

$$[M]\ddot{\mathbf{u}} + [\mathsf{K}]\mathbf{u} = \mathbf{F}. \tag{3.2}$$

For a system containing N atoms, this is a system of $3N$ differential equations, where $\mathbf{u} = [u_1^1, u_2^1, u_3^1, \ldots, u_1^p, u_2^p, u_3^p, \ldots, u_1^N, u_2^N, u_3^N]^{\mathrm{T}}$ represents the displacement vector. $[M]$ is a diagonal matrix known as the mass matrix, in which every atomic mass repeated thrice along the diagonal, as there are three displacement components for every atom. $\mathbf{F}$ is the force vector, containing components of external forces acting on each atom, given as $\mathbf{F} = [f_1^1, f_2^1, f_3^1, \ldots, f_1^p, f_2^p, f_3^p, \ldots, f_1^N, f_2^N, f_3^N]^{\mathrm{T}}$. In this way, the atomistic Hessian matrix can be interpreted as the force-constant matrix linking a set of atoms through Newton's laws connected to each other by linear springs.

Under static conditions, eq. 3.2 takes the form

$$[\mathsf{K}]\mathbf{u} = \mathbf{F}, \tag{3.3}$$

which represents a set of $3N$ simultaneous equations in $6N$ variables, $3N$ of which are atomic displacements (u_i^p) and the rest $3N$ are external forces on the atoms (f_i^p). Choosing a combination of atomic displacements and applied external forces, this system of equations can be solved to obtain the remaining displacements and forces. Applying specific loading conditions pertaining to standard tests (for evaluation of structural moduli), the corresponding force-deformation behavior can be obtained from eq. 3.3. In this way, and as further demonstrated in Section B, the atomistic Hessian matrix can be utilized to evaluate force-displacement behavior and subsequently the structural moduli of a material system at the nanoscale, in addition to its classical utility in predicting transition states of atomistic configurations.

B. Evaluation of linear structural stiffness of SWCNTs using the atomistic Hessian
matrix

The methodology for evaluation of force-displacement response using the atomistic Hessian matrix, as described in section 2, is implemented in the current section to obtain linear elastic stiffness in extension and torsion for single walled carbon nanotubes (SWCNTs). These measures of linear elastic stiffness are similar to Young's and shear moduli of elasticity assuming the SWCNT to be homogenized as a continuum.

1. Modeling of SWCNTs using quantum mechanical calculations and evaluation of the atomistic Hessian matrix

A quantum mechanical model of a SWCNT was prepared in the Gaussian suite of programs where the geometry was specified using the z-matrix method [75, 76]. The z-matrix method incorporates the specification of connectivity between constituent atoms with respect to a common reference, from which cartesian coordinates can be derived easily. The advantage of using the z-matrix over specification of cartesian coordinates is that it allows the evaluation of molecular symmetries, a feature which simplifies quantum mechanical calculations. For the SWCNT prepared in this work, the z-matrix was constructed using an initial C-C bond-length of 1.42Å.

(a)

(b)
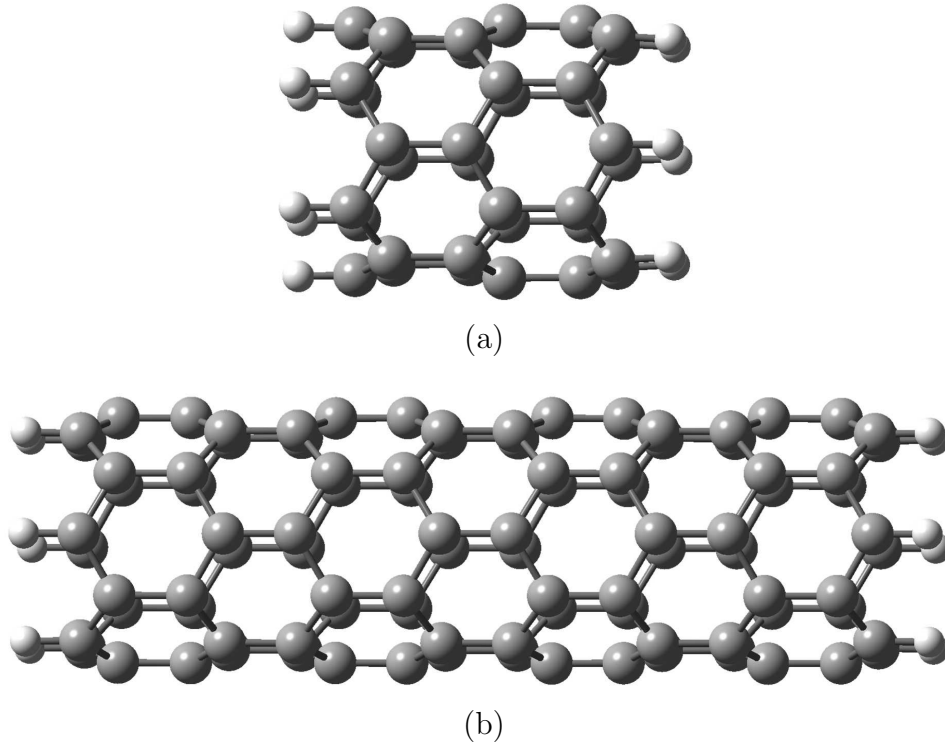
Fig. 4.: SWCNTs consisting of carbon (grey) and hydrogen (white) (a) two ring (6,0) SWCNT, (b) seven ring (6,0) SWCNT.

The structures of SWCNT, were capped with hydrogen atoms, as shown in figure 4. Zigzag SWCNTs of specification (6,0) and (12,0) were modeled in the present work, where the nomenclature $(n, 0)$ refers to the zigzag nanotube containing n carbon atoms along the circumference. Several models of SWCNTs were constructed, containing up to seven rings, in the case of (6,0) SWCNTs and up to four rings in the case of (12,0) SWCNTs.

The SWCNT structures were optimized using the Gaussian software for its minimum energy and thereafter frequency calculations were performed on the optimized geometries using the Hartree Fock (HF) quantum mechanical calculations to obtain natural frequencies and modal shapes for the SWCNT structures[74, 97–99]. The HF theory was chosen because it models every individual electron in the system using the Schrödinger wave equation. $3N-6$ sets of frequencies and modal shapes were obtained for the SWCNT and to this set, 6 additional sets were added, characterized by zero frequency and rigid body modal shape representing translation in 3 directions and rotation along 3 axes. The non-zero frequencies obtained from the HF calculations were scaled by a factor of 0.9 [75]. The final set of $3N$ frequencies and modal shapes were subjected to modal synthesis (Appendix A) to obtain the atomistic Hessian matrix for the SWCNT. The atomistic Hessian matrix hence obtained was utilized for performing force-displacement analysis on the SWCNT structure.

2. Evaluation of linear elastic stiffness in extension using the atomistic Hessian matrix

Figure 5 describes the uniaxial tensile deformation of the SWCNT where boundary hydrogen atoms were displaced in opposite directions by equal amounts, representative of axial stretch. For these atoms (refer eq.3.3), only the axial component of displacements was specified (i.e. u_z^k), while the transverse components of the forces
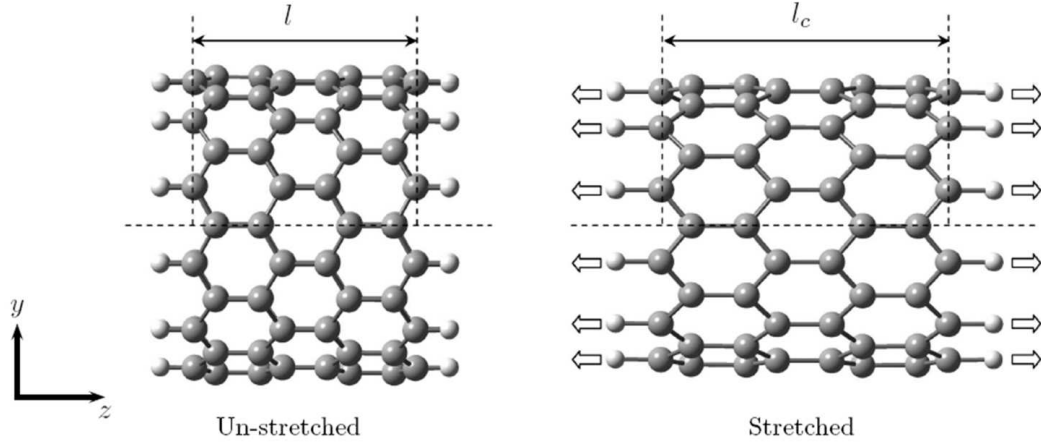
Fig. 5.: Boundary displacement conditions applied on SWCNT to evaluate the linear elastic stiffness in extension.

were set to zero (i.e. $f_x^k = f_y^k = 0$). Substituting the axial components of displacements, the transverse components of forces for outer atoms, and zero forces in all the components for the inner atoms, eq. 3.3 can be re-arranged to have all unknowns in $\hat{\mathbf{u}}$ and all specified fields in $\hat{\mathbf{f}}$. Thus the set of equations can be represented as follows

$$[\hat{\mathsf{K}}]\hat{\mathbf{u}} = \hat{\mathbf{f}}, \tag{3.4}$$

where $[\hat{\mathsf{K}}]$ is the modified coefficient matrix. This set of equations was solved to obtain axial force components and transverse displacement components for outer atoms and all displacement components for inner atoms.

Having obtained all forces and displacements for all the atoms in the SWCNT, the SWCNT was approximated as a hollow continuum tube. The total axial force, f on the tube was obtained by summing up the axial component of the forces on the hydrogen atoms on any one side, $\mathsf{f} = \sum_k^{(outer)} f_t^k$. The total axial force, f was used to obtain the linear elastic stiffness in extension, Y, by establishing an equivalence of

the discrete atomistic structure with a continuum tube[100]

$$Y = \frac{\mathsf{f}l}{\delta A} \qquad (3.5)$$

where l is the un-deformed length of the SWCNT (Figure 5), represented by the distance between carbon atoms at the opposite ends, $\delta = (l_c - l)$ is the extension of the tube, l_c is the length of the stretched tube, and A is the cross sectional area of the SWCNT, which is based on the inter-planer separation in graphite of 3.4Å. The nominal strain is given as $\epsilon = \delta/l$.

The boundary conditions are applied on the outer hydrogen atoms to deform the system as a whole and thereby the behavior of the inner carbon atoms was analyzed to evaluate the force-displacement behavior. This methodology, consistent with the St. Venant's principle, was adopted to minimize the effect of displacing hydrogen atoms on the force-displacement response of the SWCNT. However, the presence of the hydrogen atoms still influences the stiffness of the carbon bonds situated close to the hydrogen atoms which affects the behavior of the SWCNT as a whole. To address this feature, SWCNT structures of longer length were analyzed, which contained up to seven rings for (6,0) SWCNTs and four rings for (12,0) SWCNTs.

The linear elastic stiffness in extension evaluated using the atomistic Hessian matrix method for SWCNTs of different number of rings using the Hartree Fock theory is plotted in figure 6 along with the predictions of that evaluated by several other existing models in literature. It can be observed that as the size of the SWCNT is increased, by addition of rings in the SWCNT structure, the effect of end-capped hydrogen atoms reduces which causes the linear elastic stiffness in tension to demonstrate convergent behavior.

The atomistic Hessian matrices, evaluated from the HF method, that were used to compute the linear elastic stiffness in extension for (6,0) and (12,0) SWCNTs,
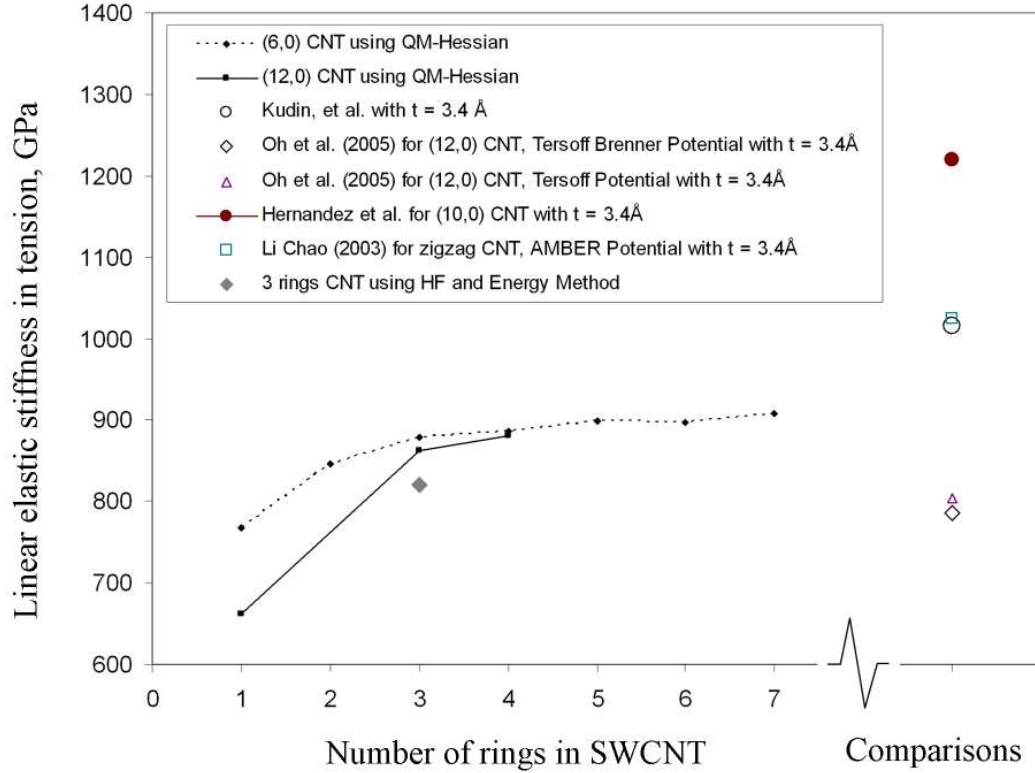
Fig. 6.: Linear elastic stiffness in extension for (6,0) and (12,0) CNTs for different number of rings evaluated using the atomistic Hessian method and comparison with other existing models.

can also be utilized to obtain the linear elastic stiffness in torsion for the respective structures as given in the next subsection.

3. Evaluation of linear elastic stiffness in torsion using the atomistic Hessian matrix

The atomistic Hessian matrix based method can be utilized to evaluate the response of the SWCNT in shear loading as well. Since the method can accommodate the application of loads on individual atoms, the shear test was performed by displacing the outer atoms with the application of a twist. In twisting the SWCNT about the axis, instead of displacing the hydrogen atoms, the carbon atoms of the outer rings
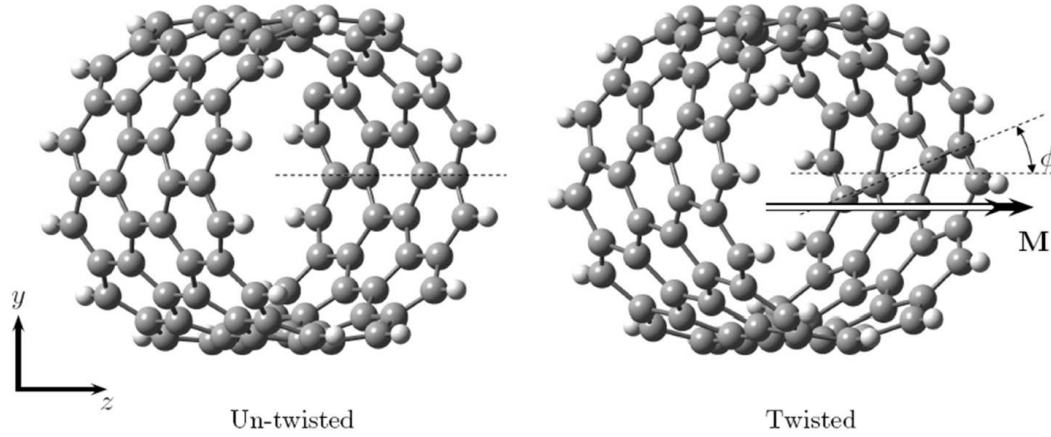
Fig. 7.: Boundary displacement conditions applied on SWCNT to evaluate linear elastic stiffness in torsion.

were displaced as shown in Fig. 7. These set of boundary conditions were chosen because applying displacement boundary conditions of twist nature on the hydrogen atoms would cause significant jump in deformation because the hydrogen-carbon bond is weaker compared to carbon-carbon bond. The end carbon atoms were displaced by angular displacement of $+\phi$ and $-\phi$ external forces on all other atoms were zero, including the hydrogen atoms, and the resulting system of equations were solved. The solution of the system of equation gave the tangential forces on the carbon atoms of the outer rings, which cause the twist. The forces were utilized to obtain the moment, $\mathbf{M}(= M\mathbf{e}_z)$, causing the twist. Assuming the nanotube to be a homogeneous cylinder of thickness 3.4Å, the linear elastic stiffness in torsion was evaluated as given by[100]

$$G = \frac{Ml}{J\phi},\tag{3.6}$$

where $M = \sum_{k}^{(outer)} f_t^k r$ is the sum of moments contributed by the forces acting on each carbon atom of the outer ring. Moreover, $r = 1/2(r_0 + r_i)$ where r_o is the outer

radius and r_i is the inner radius of the SWCNT, l is the distorted length of the nanotube (measured between the outer carbon atoms in the unloaded SWCNT), and $J = \pi/2(r_0^4 - r_i^4)$ is the polar moment of area of the cross section of the nanotube.
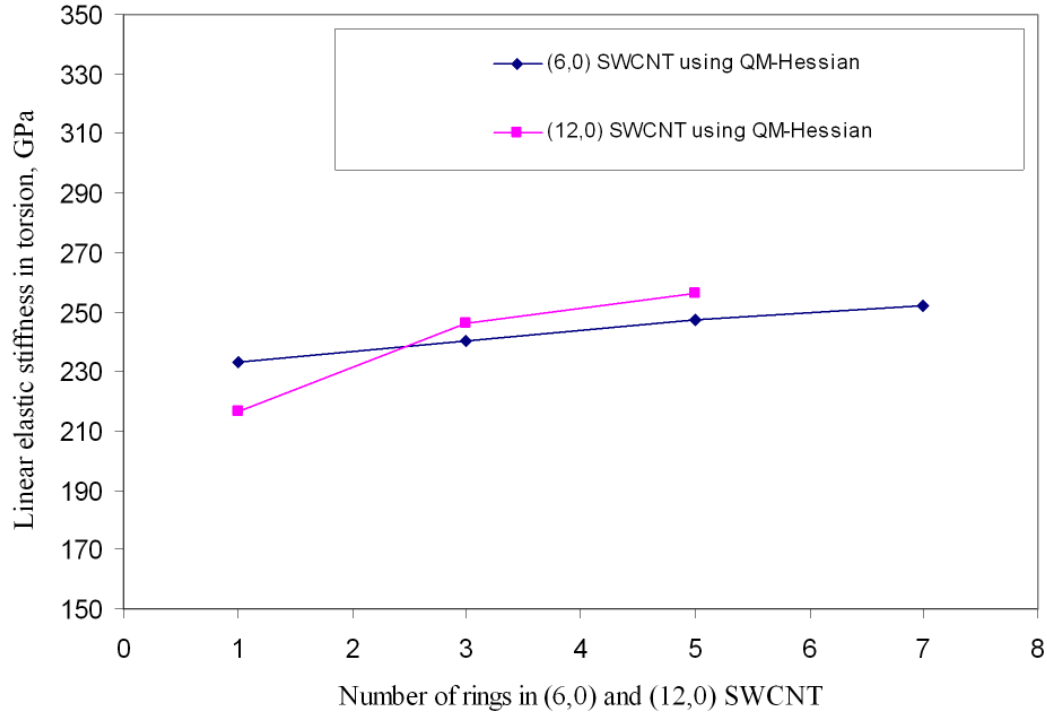
Fig. 8.: Linear elastic stiffness in torsion for (6,0) and (12,0) CNTs for various number of rings evaluated using the Hessian method and comparison with other existing models.

Figure 8 shows the linear elastic stiffness in torsion evaluated using the Hessian matrix method for (6,0) and (12,0) CNTs for rings. Thus, it can be observed that the atomistic Hessian matrix can be utilized to obtain the linear force-displacement response of material systems at the nanoscale for a variety of loading conditions and the main computational effort is concentrated in the evaluation of the atomistic Hessian matrix. In the next sub-section, a study is performed to investigate the

impact of the axial strain on the natural frequencies of a SWCNT.

4. Effect of axial stretch on frequencies of SWCNTs

In this sub-section, frequency calculations were performed for a three ring $(12,0)$ nanotube under axial strain using the HF quantum mechanical calculations. Utilizing the feature in Gaussian to constrain bond lengths, the SWCNT was stretched by 0.4% of the initial length. This system was re-optimized for minimum energy configuration, allowing the inner atoms to relax. After the optimization, a frequency calculation was performed and the frequencies, ω, of the un-strained and strained structures were compared.

Fig. 9 shows five different modes of vibration analyzed, and Table I shows the comparison of frequencies for the five modes. Radial breathing modes are described by atoms vibrating along the radius of the SWCNT whereas the axial stretch modes are characterized by vibration of atoms along the axis of the SWCNT. From the analysis, it was observed that the frequencies of the radial breathing modes increased on application of positive nominal strain while those of the axial stretch modes decreased. Moreover, the magnitude of the shift of the frequencies was lesser for radial breathing modes as compared to axial stretch modes. These trends in shift for both radial as well as axial modes were in agreement with experimental measurement of Raman intensities for CNTs [101, 102], as tabulated in Table II. Moreover, the magnitude of the un-strained frequencies of Raman active modes as calculated by quantum methods lie in the range predicted by the experiments.

The variation of natural frequencies with application of strain shows that the SWCNT does not exhibit linear behavior for strains even as small as 0.4%. Careful consideration must be taken on the evaluation of the linear elastic stiffness in extension while loading the SWCNT to this strain level, because the SWCNT structure

(a)

(b)

Radial Breathing Modes

(c)   (d)   (e)

Axial Stretch Modes
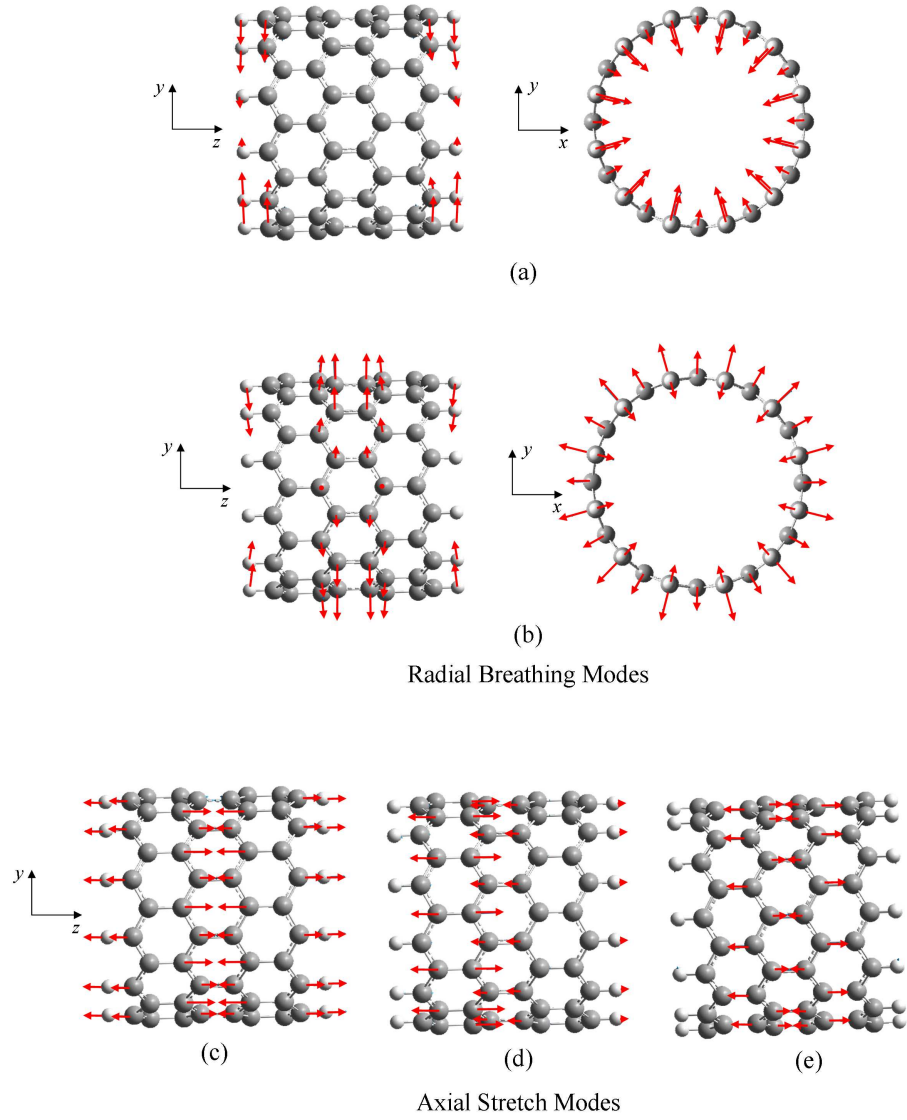
Fig. 9.: Five modes of vibration selected for investigating the effect of axial deformation on natural frequencies for a (12,0) SWCNT. The arrows represent eigenvectors.

Table I.: Comparison of five modal frequencies of a 3-ring $(12, 0)$ SWCNT evaluated using HF quantum mechanical method for unstrained and 0.4% axially strained configurations.

Mode	ω for unstrained SWCNT (cm^{-1})	ω for 0.4% strained SWCNT (cm^{-1})	shift in ω (cm^{-1})	Percent shift $(\%)$
First Radial	235.53	237.46	+1.93	+0.82
Second Radial	244.00	246.50	+2.50	+1.02
First Axial	1066.21	1058.06	-8.15	-0.76
Second Axial	1490.34	1482.41	-7.93	-0.53
Third Axial	1518.34	1512.91	-5.43	-0.36

deviates from linearity and therefore the evaluated modulus will lose accuracy. This is demonstrated in the following, where the linear elastic stiffness in extension was evaluated by sequentially deforming a (12,0) 3 ring SWCNT in the axial direction and evaluating the energy at ±0.3% and ±0.6% strain levels. This is the order of the strain level that has been applied to the SWCNT for evaluating the linear elastic stiffness in extension by the energy method [12].

5. Evaluation of linear elastic stiffness in extension using the energy method

For uniaxial deformation, the linear elastic stiffness in extension, Y, is given by

$$Y = \left(\frac{\partial^2 \hat{\Phi}}{\partial \epsilon^2} \right)_{\epsilon=0} \tag{3.7}$$

where $\hat{\Phi} = \Phi/V_0$ is the strain energy per unit un-deformed volume and ϵ is the axial strain. The above expression can be rewritten as

$$Y = \frac{1}{V_0} \left(\frac{\partial^2 \Phi}{\partial \epsilon^2} \right)_{\epsilon=0}, \tag{3.8}$$

Table II.: Comparison of three modal frequencies of a SWCNTs obtained using Raman Spectroscopy for unstrained and 0.45% axially strained SWCNTs.

Mode	ω for unstrained SWCNT (cm^{-1})	ω for 0.45% strained SWCNT (cm^{-1})	shift in ω (cm^{-1})	Percent shift (%)
Radial[102]	272	274	+2	0.74
Axial[101]	1594	1589	-5	-0.31
Axial[102]	1600	1594	-4	-0.25

where V_0 is the un-deformed volume.

The atomistic Hessian matrix method and the energy method for evaluating the linear elastic stiffness in extension are equivalent, as is demonstrated in Appendix B. To demonstrate the the energy method for evaluating the linear elastic stiffness in extension, quantum mechanical energy calculations were performed over a 3 ring (12,0) SWCNT. The SWCNT was first optimized in geometry using the 3-21g basis sets with the HF quantum mechanical computations. The thresholds for maximum force and maximum displacement for each atom during optimization was taken to be the default for Gaussian jobs as 0.00045 a.u. and 0.0018 a.u. respectively. Axial strain was applied to the SWCNT by a feature provided in the Gaussian program that facilitates the constraining of several bonds. Starting with the optimized geometry, strains were applied by fixing the outermost carbon atoms to distances pertaining to overall tensile and compressive nominal strains of a maximum of 0.6%. These atoms were fixed throughout the next step of optimization where the inner atoms were allowed to re-equilibrate. From these set of optimized geometries, the variation of potential energy was obtained, as plotted in figure 10. The data points were fitted using least squares method to obtain the second derivative of the energy at zero

nominal strain. The linear elastic stiffness in extension was evaluated using eq. 3.8 where V_0 was computed based on the length of the SWCNT between outermost carbon atoms. The area of cross-section was assumed to be 3.4Å, equal to the interplanar spacing in graphite. The modulus value was evaluated to be 820 GPa using the energy method. It can be observed from Figure 6 that the linear elastic stiffness in
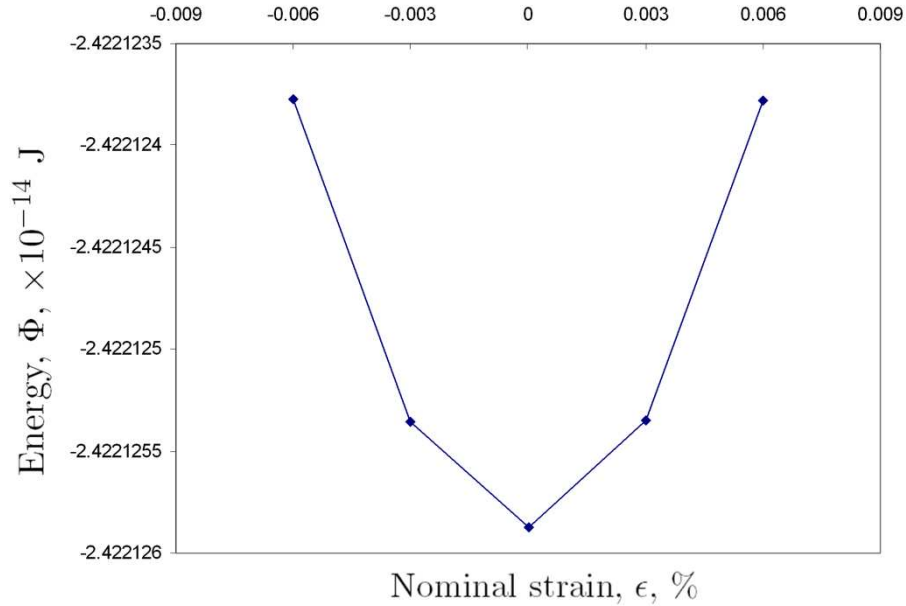
Fig. 10.: Variation of energy with respect to nominal strain evaluated using Hartree Fock quantum mechanical calculations for a 3 ring (12,0) SWCNT.

extension evaluated from the Hessian method for the (12,0) 3 ring SWCNT using HF quantum mechanical calculations was 881 GPa, which differs from the energy method by about 4.7%. Even though the energy method and the atomistic Hessian method are theoretically equivalent, the application of strains of the order of 0.3–0.6% introduces error due to loss in linearity which is also demonstrated in the frequency shifts. The analysis of this sub-section demonstrates that, even though the atomistic Hessian based method and the energy method are equivalent in theory, the energy

method should be used with caution for systems that deviate from linearity in the range of applied deformation.

C.   Comparison of the components of the atomistic Hessian matrix

In this section, comparisons are presented for some chosen components of the atomistic Hessian matrix, evaluated using quantum mechanical calculations, the Tersoff Brenner (TB) Potential and an experimentally based method. All calculations were performed for a (12,0) SWCNT structure.

1.   Evaluation of atomistic Hessian matrix using experimental data

In this sub-section, the atomistic Hessian matrix has been evaluated using experimental data and methodology from Jishi et al.[103] and Dresselhaus et al.[104] which is referred to as the *zone folding method*. Using the *zone folding method*, the atomistic Hessian matrix for a SWCNT can be evaluated using force constants obtained experimentally for graphene. This method has also been used for structures different from SWCNT e.g. in the work of Popov[105], where the procedure was implemented for Boron-Nitride Nanotubes, obtaining experimental data from Boron-Nitride flat sheet structure.

With reference to the *zone folding method*[103–105], the expression for Newton's law for the static case, (which describes the interaction of atom p in graphene with its sth nearest neighbor q, where $s = 1, \ldots, 4$ with respect to a local coordinate system) is assumed to be of the form

$$\begin{bmatrix} \phi_{to}^{(s)} & 0 & 0 \\ 0 & \phi_{ti}^{(s)} & 0 \\ 0 & 0 & \phi_{r}^{(s)} \end{bmatrix} \left\{ \begin{array}{c} u_{to}^{q} - u_{to}^{p} \\ u_{ti}^{q} - u_{ti}^{p} \\ u_{r}^{q} - u_{r}^{p} \end{array} \right\} = \left\{ \begin{array}{c} F_{to}^{ps} \\ F_{ti}^{ps} \\ F_{r}^{ps} \end{array} \right\}, \tag{3.9}$$

where *to*, *ti* and *r* refer to the local coordinate system containing the pair of atoms p and q, characterized by 'transverse out-of-plane', 'transverse in-plane' and 'radial' directions respectively, $\mathbf{u}^p$ and $\mathbf{u}^q$ are small the displacements of atoms p and q from their equilibrium positions and $\mathbf{F}^{pq}$ is the force acting on atom p due to atom q. Denoting the force constant tensor [104] (which was assumed to be diagonal in the *zone folding method*[103–105]) by $\mathbf{k}^{ps}$, eq. 3.9 can be rewritten as

$$\mathbf{k}^{ps}\left(\mathbf{u}^q - \mathbf{u}^p\right) = \mathbf{F}^{pq} \quad \text{or,} \quad \left[k^{ps}\right]\{u^q - u^p\} = \{F^{pq}\}. \tag{3.10}$$

This can be rewritten in the global coordinate system by performing a coordinate transformation mapping graphene to the global coordinate of the (12,0) SWCNT [104] as follows

$$[Q^q]^{\mathrm{T}}[k^{ps}][Q^q]\{u^q - u^p\} = \{F^{pq}\}. \tag{3.11}$$

Denoting $[Q^q]^{\mathrm{T}}[k^{ps}][Q^q]$ by $[K^{pq}]$, we have

$$\left[K^{pq}\right]\{u^q - u^p\} = \{F^{pq}\}, \tag{3.12}$$

where the matrix $\left[K^{pq}\right]$ is a sub-matrix of the atomistic Hessian matrix for the (12,0) SWCNT,

$$[\mathsf{K}]_{ij}^{pq} = \left[K^{pq}\right]_{ij}. \tag{3.13}$$

For the zigzag chirality of SWCNTs analyzed in the present work, the zigzag SWCNT and the corresponding graphene system, have 3 first neighbors, 6 second neighbors, 3 third neighbors and 6 fourth neighbors. Numbering the neighbors such that atoms 1, 2 and 3 belong to the first neighbor set (i.e. $s = 1$), atoms 4 to 9 belong to the second ($s = 2$), 10 to 12 belong to the third set ($s = 3$) and 13 to 18 belong to the fourth neighbors set ($s = 4$) (Fig. 11), the total force acting on atom p on the
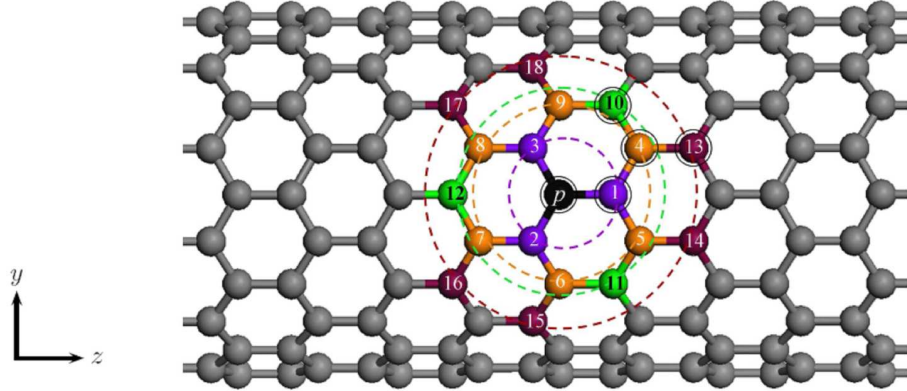
Fig. 11.: Eighteen neighboring atoms in a (12,0) SWCNT for an atom p, where interactions up to fourth nearest neighbor distance have been incorporated.

(12,0) SWCNT due to all the 18 neighboring atoms is given as

$$\{F^p\} = \sum_{q=1}^{18}[K]^{pq}\{u^q - u^p\},\qquad(3.14)$$

where $s = 1$ for $q = 1, 2, 3$, $s = 2$ for $q = 4, \ldots, 9$, and so on. After simplification, eq. 3.14 results in the following

$$\{F^p\} = \sum_{q=1}^{18}[K^{pq}]\{u^q\} - \left(\sum_{q=1}^{18}[K^{pq}]\right)\{u^p\}.\qquad(3.15)$$

Thus, the diagonal sub-matrix of the atomistic Hessian matrix K^{pp} can be written as

$$[\mathsf{K}]_{ij}^{pp} = -\left(\sum_{n=1}^{18}[K]_{ij}^{pq}\right).\qquad(3.16)$$

In the present work, the global atomistic Hessian matrix was evaluated for a (12,0) SWCNT by assembling the sub-matrices for the constituent atoms by the above procedure and using the experimental data [104]. Specific sub-matrices of the global atomistic Hessian matrix ($[\mathsf{K}]^{pq}$) have been tabulated in table III, corresponding to interactions of atom p with neighbors labeled 1, 4, 10 and 13 (eq. 3.13). The diagonal

sub-matrix of the atomistic Hessian matrix described by eq. 3.14 was evaluated using the experimental data and is given in table IV.

2. Evaluation of the atomistic Hessian matrix using the HF method and the TB potential

This subsection discusses the atomistic Hessian matrix evaluated for a 3 ring (12,0) SWCNT using HF quantum mechanical calculations and a (12,0) periodic SWCNT using the TB Potential. From the atomistic Hessian matrix for the 3 ring (12,0) SWCNT, sub-matrices pertaining to interaction of the central atom p with neighbors labeled 1, 4, 10 and 13 in Fig. 11 were obtained and have been tabulated in Table III. It was observed that the diagonal sub-matrix of the atomistic Hessian matrix, (denoted by $[\mathsf{K}]^{pp}$) as obtained from the quantum mechanical calculations, was equal to the sum of the force-constant sub-matrices corresponding to interaction of atom p with all the atoms,

$$[\mathsf{K}]^{pp}_{ij} = \sum_{q=1}^{N} [K]^{pq}_{ij}. \tag{3.17}$$

Table IV shows the diagonal sub-matrix of the atomistic Hessian matrix for a (12,0) 3 ring SWCNT evaluated using the HF method.

For a potential energy function that represents the potential energy of a set of atoms with respect to their relative positions, analytical second derivatives can be evaluated using eq. 3.1 to obtain the components of the atomistic Hessian matrix. In the present work, the TB Potential was chosen to represent the potential energy Φ in eq. 3.1. The potential was set up to represent a minimum energy configuration of a (12,0) SWCNT and analytical second derivatives were taken to obtain the components of the atomistic Hessian matrix. The atomistic Hessian matrix using the quantum mechanical calculations and the TB Potential are shown in Table III. The terms in

the atomistic Hessian matrix corresponding to the TB Potential for second neighbors and beyond are zero due to the cut-off distance employed in the potential.

Table III.: Comparison of Hessian sub-matrices evaluated using experimental data, the HF method and the T-B potential.

	Experimental			HF			T-B		
$[K]^{p1}$	98.20	0.00	0.00	113.00	0.00	5.36	34.41	0	0
	0.00	245.00	0.00	0.00	245.30	0.00	0	27.51	0
	0.00	0.00	365.0	−5.36	0.00	400.90	0	0	370.09
$[K]^{p4}$	−3.94	−0.43	−6.92	−5.90	−3.29	1.45		−	
	−0.43	−0.67	52.54	−3.60	−44.94	57.48			
	−6.92	52.54	56.31	15.05	58.22	37.45			
$[K]^{p10}$	2.11	−2.27	−9.06	9.32	4.24	0.27		−	
	−2.27	9.96	33.81	−1.32	14.38	−37.75			
	−9.06	33.81	−33.07	−19.11	−32.55	20.15			
$[K]^{p13}$	−5.39	−3.11	1.73	−12.87	3.34	−5.60		−	
	−3.11	17.78	−13.16	4.40	11.61	12.66			
	1.73	−13.16	−14.49	1.64	13.46	−9.89			

This is for the first time that components of the atomistic Hessian matrix evaluated using experimental data and atomistic methods have been compared and analyzed. From this comparison it was observed that the elements of the sub-matrix of atomistic Hessian matrix obtained by experimental data and the HF method had

Table IV.: Comparison of diagonal sub-matrix of atomistic Hessian matrix for (12,0) SWCNT evaluated using experimental data and the HF method. The experimental column corresponds to interactions of atom p with up to fourth neighboring distance while the HF column incorporates interactions with all other atoms in the SWCNT.

	Experimental			HF		
$[\mathsf{K}]^{pp}$	191.01	−0.01	0.00	285.49	0.00	15.71
	−0.01	1110.35	−7.80	0.00	1135.69	0.00
	0.00	−7.80	1057.85	15.71	0.00	1115.10

comparable diagonal elements for the first neighbor interaction, $[K]^{p1}$. Of all the interactions, the one with the first neighbor is the strongest, since it is represented by a direct covalent bond and hence the force-constants representing this interaction show agreement between experimentally derived and HF evaluated methods. The atomistic Hessian matrix evaluated using the TB Potential showed good comparison for the axial-stretch component of the first neighbor interaction, while the other two diagonal force-constants differed significantly. It can be further observed from Table III that all the sub-matrices corresponding to the experimental method were symmetric. This is because these matrices were originally diagonal (eq. 3.9), and obtained symmetry after undergoing orthogonal transformation (eq. 3.11). It was further observed that the individual off-diagonal sub-matrices of the atomistic Hessian, $[\mathsf{K}]^{pq}$, obtained from the quantum mechanical methods were not symmetric. However the diagonal sub-matrix $[\mathsf{K}]^{pp}$ was observed to be symmetric as shown in Table IV.

The off-diagonal $(i, j)^{\text{th}}$ element of the sub-matrix $[k]^{pq}$ (eq. 3.9, $i \neq j$), namely

$([k]^{pq})_{ij}$, represents the ith component of the force that acts on atom p when the atom q is displaced by unit amount in the jth direction and all other atoms are fixed. The $(j,i)^{\text{th}}$ element, $([k]^{pq})_{ji}$, which is the jth component of the force on atom p due to unit displacement of atom q along i^{th} direction is not related physically to $([k]^{pq})_{ij}$ and can therefore be numerically different. In the modeling of the *zone folding method*[103, 104] however, the off-diagonal elements in the force-constant matrix were assumed to be zero, thus enforcing symmetry in the off-diagonal sub-matrices of the experimentally derived atomistic Hessian matrix (eq. 3.9).

The diagonal sub-matrix of the atomistic Hessian $[\mathsf{K}]^{pp}$, given in Table IV physically represents the force acting on atom p due to the displacement of atom p, while all the other atoms are fixed in space. Observing the components of $[\mathsf{K}]^{pp}$, it can be inferred that the in-plane stiffness of the SWCNT is about the same in y and z directions, as indicated by the $(2,2)$ and $(3,3)$ components for both experimental as well as *ab initio* results. Additionally, the numerical values of the elements of $[\mathsf{K}]^{pp}$ for HF case show that the displacements in x and z are coupled, due to the non-zero $(1,3)$ and $(3,1)$ component. Physically, this represents a radial deformation coupled with axial displacement which is the reason for the Poisson's effect in the SWCNT structure and is an important observation of the properties of the atomistic Hessian matrix evaluated using atomistic calculations. It can also be seen that the atomistic Hessian obtained using experimental data (Table IV) did not possess this structural property.

Studies have been performed where vibrational frequencies and mode shapes for SWCNTs were evaluated using tight binding calculations [106] and molecular mechanics based on a force field [107]. These mode shapes and frequencies obtained computationally were compared with those obtained experimentally from Raman spectroscopy. In these studies emphasis was placed mainly on the vibrational information

(which is obtained by diagonalizing the Hessian) rather than on the analysis of the components of the Hessian matrix itself. The present research focuses on the components of the atomistic Hessian matrix and compares the atomistic Hessian matrix developed using the *zone folding method.* This gives a more detailed understanding of both, the interactions between the atoms at the nanoscale in SWCNTs, as well as the use of experimentally obtained interactions in predicting the mechanical behavior of SWCNTs.

The atomistic Hessian matrix using quantum mechanical computations provides a qualitatively more accurate representation of the stiffness of the SWCNT compared to the experimentally derived analogue. It was demonstrated that the Hessian method not only provides a computationally more economic and accurate method for evaluating the stiffness of a nanosize material system (as described in Section B) but could also be used for comparison of atomistic force-constants obtained with experiments. This feature is a merit over using the the energy method directly, where the homogenization results in the loss of atomistic detail and only the structural modulus could be compared with experimental data (if available). The atomistic Hessian method retains the discreteness of the atomistic information which can be utilized for experimental verification, and can be additionally utilized for evaluating the structural moduli.

D.   Conclusions

A method for evaluating the linear force-displacement response of an atomistic system was developed, where the atomistic Hessian matrix was utilized for solving structural boundary value problems. The atomistic Hessian matrix was calculated using modal synthesis of natural frequencies and mode shapes, obtained for zig-zag SWCNTs from

quantum mechanical calculations. Linear stiffnesses in extension and torsion of elasticity were evaluated for the zig-zag SWCNTs from the atomistic Hessian matrix using the force-displacement response. The atomistic Hessian based method is computationally less demanding compared to the strain energy based method in evaluating the linear response to prescribed loading conditions, since it overcomes the need to perform intensive atomistic calculations for each boundary value problem and can be utilized to obtain stiffness parameters of the system through a variety of loading conditions. Through this feature, the Hessian method bridges scales and is applicable in multiscale modeling of linear response of nanoscale materials.

Examination of the frequency characteristics of SWCNT with application of tensile longitudinal strain showed that the frequency shifts for radial and axial modes were similar to experimental findings of Raman shifts in SWCNTs. The shifts indicate that the atomistic Hessian matrix evaluated at the un-deformed and deformed configurations is not the same and therefore the SWCNT system is not linear over even very small strain levels. Thus, the utilization of the energy method for strain levels at which deviations from linearity are observed leads to inaccuracies in evaluation of stiffnesses. The Hessian based method is therefore more accurate compared to the energy method prevalent in the literature. Additionally, unlike the energy method, the atomistic Hessian method retains the degrees of freedom of the atoms in the system after the homogenization is performed while evaluating the structural moduli of a material at the nanoscale.

For the first time, components of the atomistic Hessian matrix evaluated using experimental data (from the *zone folding method*), quantum mechanical calculations and the Tersoff Brenner Potential were compared. It was observed that the sub-matrices of the atomistic Hessian matrix corresponding to the first nearest neighbor interaction for both *zone folding method* as well as for quantum mechanically evalu-

ated atomistic Hessian matrix were in good agreement. It was additionally observed that the atomistic Hessian matrix obtained using the quantum mechanical calculations was qualitatively the most accurate and can further explain the Poisson's effect in SWCNTs while the *zone folding method* cannot.

CHAPTER IV

MECHANICAL BEHAVIOR OF CNT POLYETHYLENE INTERFACE

The previous chapter was about the evaluation of Young's and shear moduli of elasticity for SWCNTs and it was shown that these material parameters are very high for SWCNTs. This leads to the vision of using CNTs as reinforcement materials for composites primarily due to their capability of imparting high mechanical stiffness. CNTs have been used with polymers [21, 22] to obtain composites with a variety of processing techniques. One of the main component for developing well tailored composites however is the knowledge of the behavior of the interface between the CNT and the chosen polymer. With current processing and characterization tools, only bulk behavior of the composites can be assessed since individual CNTs (and hence their interfaces) are difficult to be probed by experimentation. The current chapter is about the utilization of the molecular dynamics (MD) method to investigate the interfacial behavior of the CNT and polymer in the set up of pull out tests where the CNT is removed from a film of polymer.

A.   Problem setup

This section describes the procedure for developing representative atomistic systems that were utilized to study the mechanical behavior of the CNT polymer interface. A description is also given on the constraints applied on the system that provide relative separation where the SWCNT was pulled out of the polymer. Additional pull out tests are described where separation was carried out in presence of compressive loads.

1. Nanoscale RVEs containing SWCNT and polymer

In the present study, two nanoscale unit cells (representative volume elements, RVEs) were prepared for investigating the mechanical behavior of SWCNTs with the polymer. Both the RVEs consisted of a finite size (non-periodic) model of a SWCNT surrounded by a thin film of polymer. The polymer chosen was Polyethylene (PE) because of the simplicity of its structure. The choice of these unit cells was dictated by the force field used to model the interactions between the atoms and each of the RVEs is described as follows.

The first RVE was modeled using the CVFF force field [77] and is shown in Fig. 12a. The CVFF force field is a classical MD force field which has successfully modeled the properties of several polymers including bio-polymers, however it cannot model bond breaking and formation. In the model shown in Fig. 12, the polymer PE is amorphous and composed of straight chains of 60 monomers each. There are 32 such chains, with no covalent chemical bonds connecting them. In total, there are about 6000 PE atoms in the system and the chains are connected only by non-bonded interactions namely the Van der Waals and electrostatic components of the force field (Sect. a). The polymer was prepared first as described in Appendix C and equilibrated at 100K using the LAMMPS code [108]. The temperature of 100K was chosen because it is well below the glass transition temperature (Tg) of PE, which ranges between 190-300K. The system includes a (12,0) SWCNT which was chosen because it has a diameter of 1nm whose ends were capped by hydrogen atoms to complete the valency requirements. There were 540 carbon atoms and 24 hydrogen atoms in the SWCNT. The system comprising the SWCNT and the amorphous polymer was re-equilibrated at 100K for 50ps using LAMMPS to obtain a starting configuration to perform the pull out test. The equilibrated system occupied a volume of 58.47Å × 56.07Å ×

56.58Å (measured using atomic coordinates of the farthest atoms) and the length of the SWCNT in the equilibrated system was 46.87Å. In this model, both the SWCNT as well the polymer PE have been modeled using the same CVFF force field so as to capture the interactions between the two phases in full atomistic detail.

The second RVE is shown in Fig. 13 which utilizes the ReaxFF force field to model the interactions amongst the atoms. The ReaxFF force field is a new atomistic potential that has the capability to form and break bonds. This feature of the ReaxFF force field is utilized in designing the current model wherein bond breaking and formation is critical. The model in Fig. 13 consists of the polymer PE in network configuration in which the chains of PE are cross linked by other PE chains. There were about 2000 PE atoms in the network polymer structure with a cross link density of (ref). The polymer model was minimized in the beginning and then equilibrated at 100K through a series of steps starting from 0K. The system also consists of a (12,0) SWCNT, end-capped with hydrogen atoms. There were 360 carbon atoms and 24 hydrogen atoms in the SWCNT. The composite system comprising of the SWCNT in the network polymer was equilibrated at 100K for 50ps before performing the pull out tests. Bonds were allowed to be formed between the SWCNT and the network polymer and in the equilibrated structures there were 35 covalent interconnects joining the network PE with the SWCNT. The equilibrated system occupied a volume of 32.32Å × 32.53Å × 35.41Å while the length of the SWCNT was 33.75Å. In this model, both the SWCNT as well as the network PE have been modeled using the ReaxFF force field. This is the first time that ReaxFF has been utilized to model the mechanical interactions of the SWCNT-polymer system.
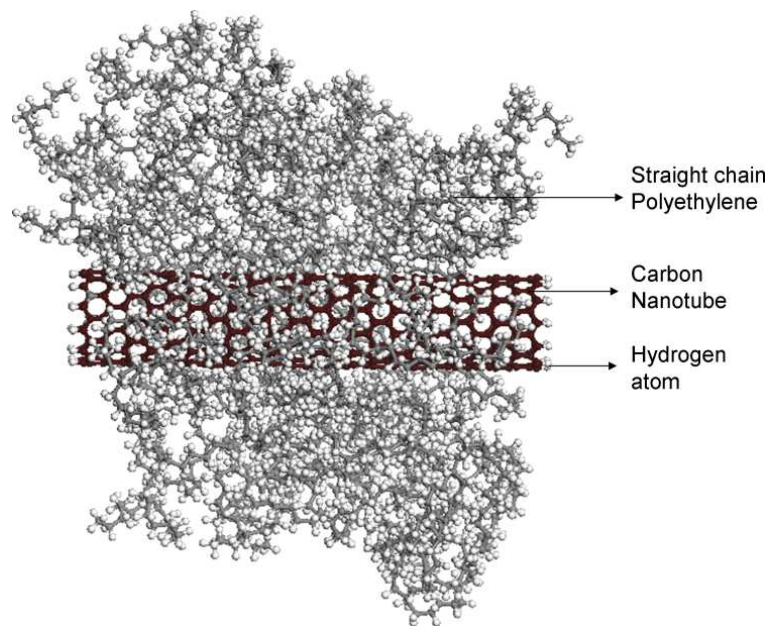
(a) Front view
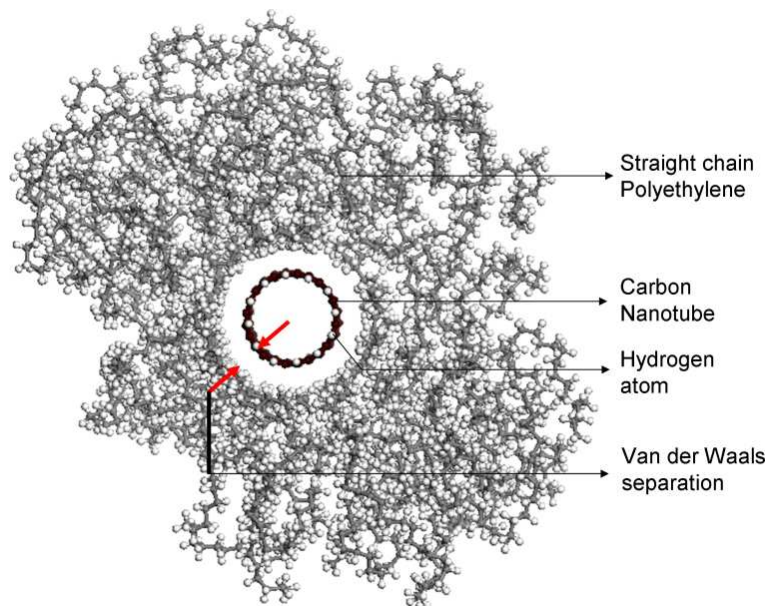
(b) Side view

Fig. 12.: Model of a SWCNT embedded in amorphous straight-chain Polyethylene. No covalent bonds exist amongst the polymer chains and between the polymer and the SWCNT. The system was modeled using the CVFF Force Field.
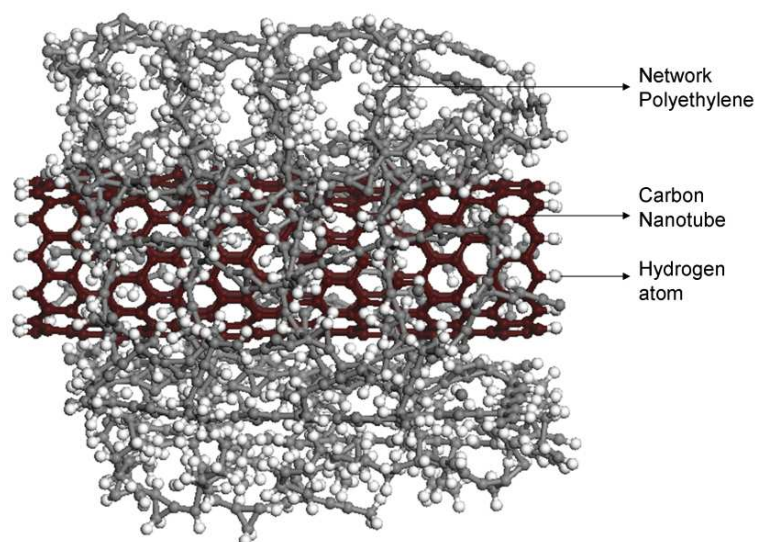
(a) Front view
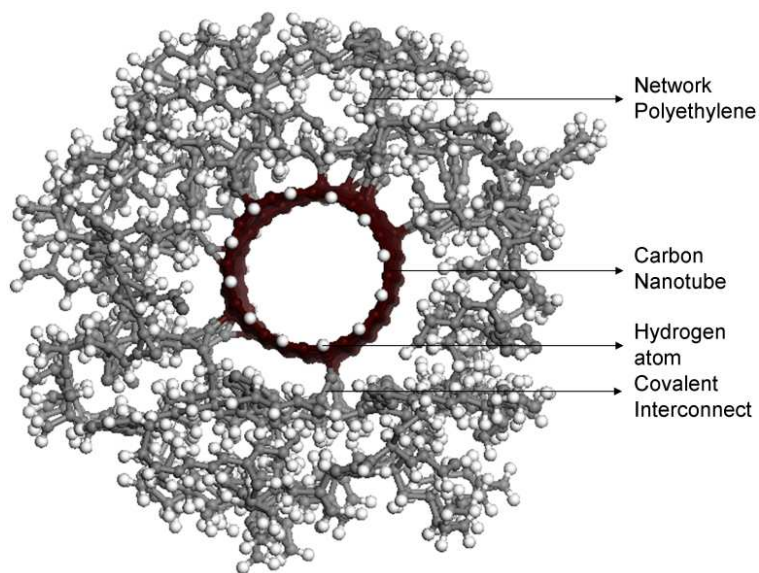
(b) Side view

Fig. 13.: Model of a SWCNT embedded in network Polyethylene. Covalent bonds exist amongst the polymer chains as well as between the polymer and the SWCNT. The system was modeled using the ReaxFF Force Field.

2.   Application of constraints

To investigate separation through a pull out test, the system comprising of the SWCNT and polymer has to be constrained in a specific way. These constraint conditions have to be imposed on the system or otherwise, the pull out of the SWCNT will cause all the polymer atoms to move together with the SWCNT due to the interatomic forces. The applied constraint condition is described in the following.

   The SWCNT is pulled out from the polymer, and small portions of the polymer at the top and bottom are fixed in space. The atoms in the SWCNT as well as those around it are not kept fixed and can move under the influence of each other as well as temperature.

This represents a system where the polymer is contained between two SWCNTs and application of symmetrical boundary conditions causes the polymer in between the SWCNTs to remain ideally fixed as shown in Fig. 14. Moreover greater the distance between the SWCNTs larger will be the portion of the polymer that would remain fixed.

The constraint condition for the two RVEs is shown in Fig. 15 where the axes of the SWCNTs coincided with the y axis, and two portions of the polymer above and below the SWCNT were constrained against movement as shown. The separation tests of pull out were performed on these systems as explained as follows.

a.   Pull out separation under no external load

For pull out separation under no load, systems depicted in Fig. 15 were utilized. The SWCNT in each of the RVE was separated from the polymer by displacing it in the y direction. Equal displacement steps of 0.5Å were applied on the SWCNT while the polymer was restrained by the constrained conditions. For each displacement step,
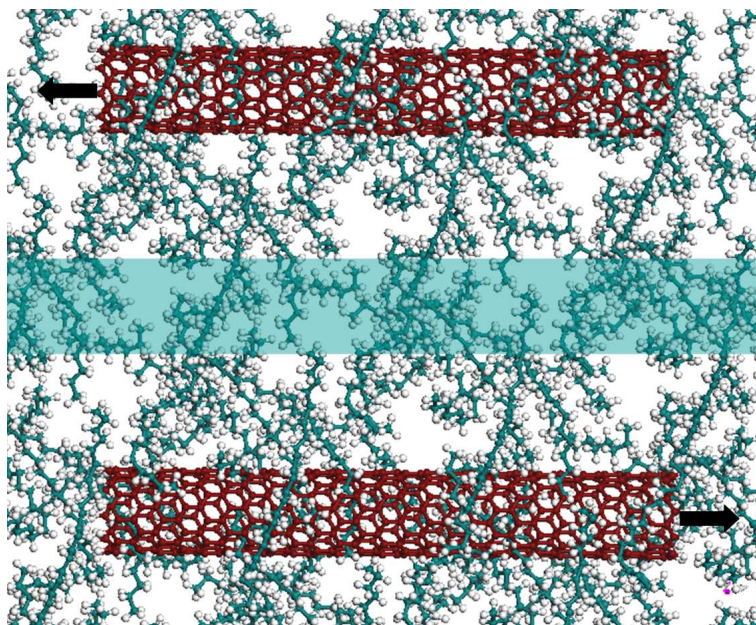
Fig. 14.: Schematic of constraint condition where the presence of symmetrical boundary conditions on two SWCNTs causes the polymer atoms in the middle portion to be ideally fixed in space. The shaded portion represents the fixed polymer.

the system was equilibrated for 10ps at 100K temperature, which sufficient for the system to achieve dynamic equilibrium at the temperature of 100K. For the entire length of the separation process, the polymer atoms in the constrained portion were kept fixed at their same initial fixed position. The polymer atoms near the SWCNT were however free to move under the influence of both the displacing SWCNT, as well as due to the vibrational motion caused by the temperature thermostat of 100K.

b. Pull out separation under transverse load

In this case, the two constrained portions of the polymer was displaced towards the SWCNT causing compression in the z direction. The pull out test was performed in presence of the transverse load that resulted due to the application of the compression. This test analyzes the effect of combined loading where SWCNT is pulled out from the polymer which was loaded by compression in a direction transverse to the pull out direction. In these studies, the SWCNT was pulled out from the polymer in equal displacement steps of 0.5Å with equilibration time of 10ps while the temperature of the system was held at 100K.

B. Results for SWCNT pull out from PE matrix under no external load

This section describes the results for the case when SWCNT pull out tests are performed without external load. Both RVEs, one modeled by the CVFF force field and another modeled by the ReaxFF force field, were utilized to perform the pull out tests.
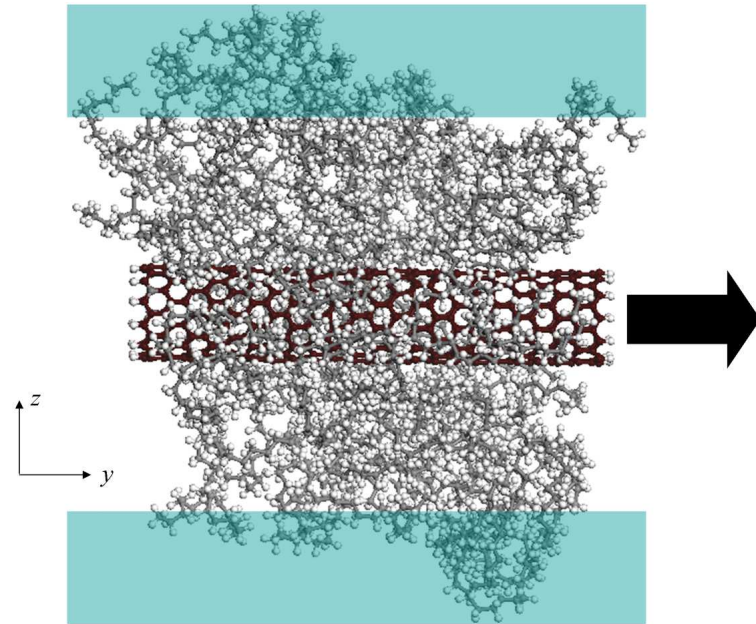
(a) Constraint condition for system modeled with the CVFF force field
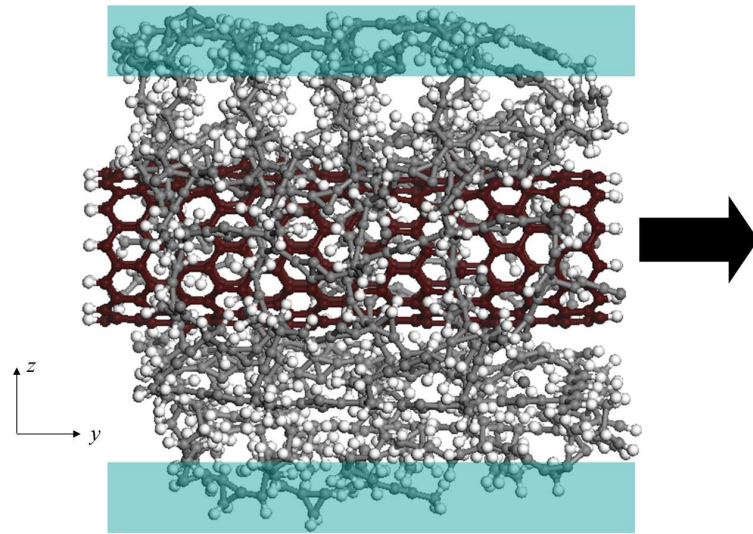
(b) Constraint condition for system modeled with the ReaxFF force field

Fig. 15.: Constraint conditions for the two model RVEs investigated. Shaded portions represent fixed atoms.

1. Results for atomistic RVE modeled by CVFF

Fig. 16 represents the pull out tests performed on the RVE modeled by the CVFF force field. The individual frames are shown at different displacement steps while the SWCNT was pulled out from the polymer. Frame (a) shows the atomistic configuration of the system in the beginning, before the SWCNT was displaced and the remaining frames shown in the figure are the atomistic configurations at displacement steps of 10Å, 20Å, 30Å, 40Åand 50Å. As the SWCNT was pulled out from PE, the y component of forces acting on all the atoms in the SWCNT was monitored. Summing up these individual force components, the y component of total force acting on the SWCNT was obtained. This total force component was normalized by the surface area of the SWCNT to evaluate the shear traction on the SWCNT. The variation of the shear traction on the SWCNT with the displacement of SWCNT is plotted in Fig. 17 and the individual frames of Fig. 16 are also indicated by the corresponding letters.

It can be observed from Fig. 17 that the total shear traction at frame (a), which represents the equilibrium configuration at the start of the test, is not zero. This is because the atoms of the SWCNT were vibrating under the influence of temperature and this motion caused a small net force. It can further be observed that with a very small pull out displacement of the SWCNT, the traction displacement response sharply increases, and reaches a maximum. The maximum shear traction is actually the minimum shear traction needed to separate the SWCNT from the polymer. With further displacement of the SWCNT, the traction displacement response fluctuates due to thermal motion and falls in magnitude. As the SWCNT separates from PE, it interacts with lesser PE atoms, reducing the y component of the force of interaction between the SWCNT and PE, thus reducing the shear traction. With increasing pull
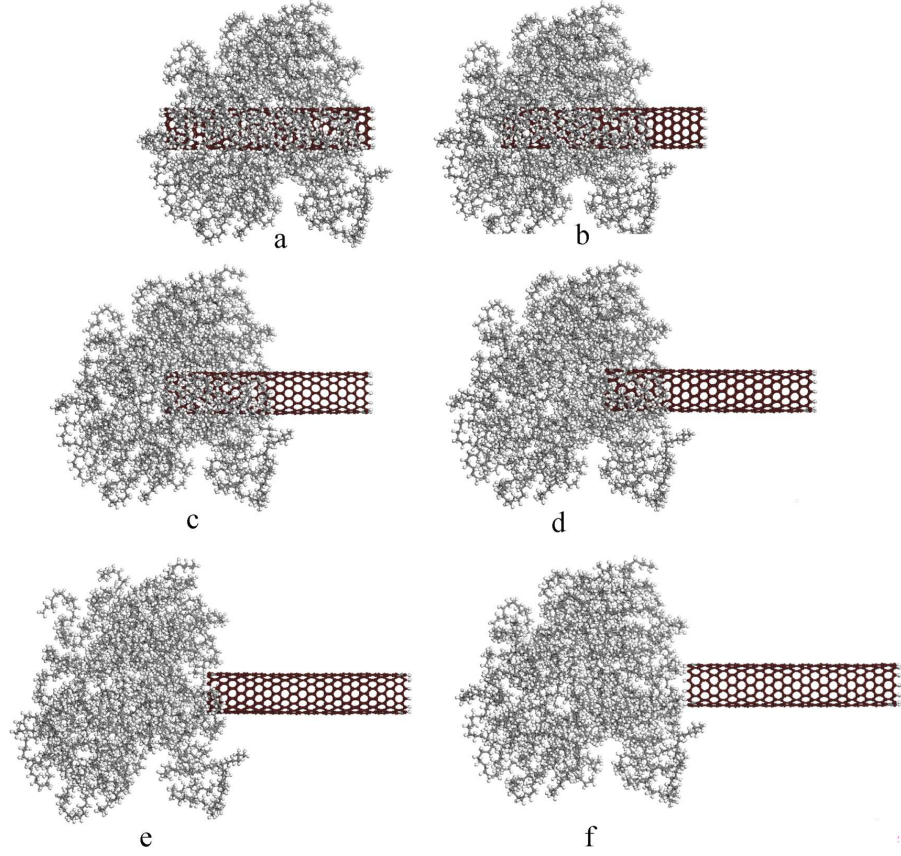
Fig. 16.: SWCNT pull out from an amorphous PE matrix with no transverse loads applied to the polymer, modeled by only non bonded interactions between the SWCNT and PE using the CVFF force field.

out displacement, the shear traction reduced further and fluctuated at a low magnitude finally reducing to almost zero when the SWCNT was completely separated from the influence of PE. The energy of shear separation was evaluated as the area under the traction displacement and was calculated to be 0.26 J/m².
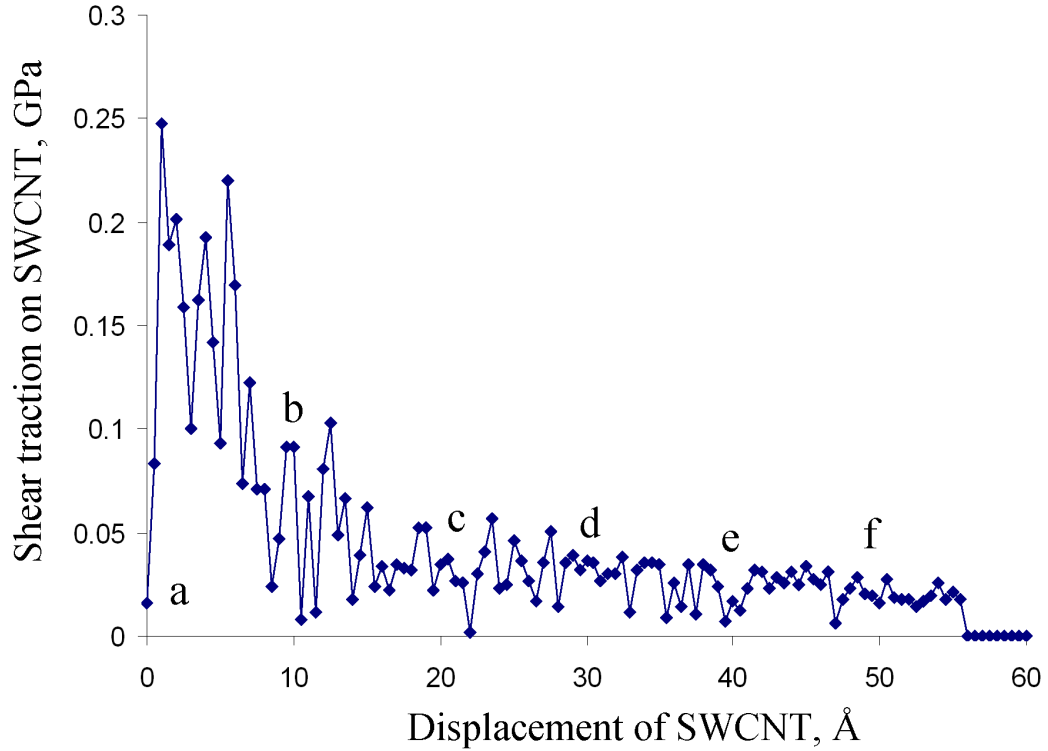
Fig. 17.: Traction displacement response of the SWCNT during pull out from PE modeled by CVFF force field.

2. Results for atomistic RVE modeled by ReaxFF

The behavior of SWCNT pull out from the network PE model is shown in Fig. 18 and Fig. 18 which show the atomistic detail of the separation process at different pull out displacements of the SWCNT. It can be observed that as the SWCNT was displaced away from the matrix, a portion of the networked PE would follow the movement of the SWCNT, because of the covalent bonding in the interconnects that join the SWCNT with the PE. With increasing displacement of the SWCNT, it was observed that covalent linkages broke, and the fragments of the interconnects occupied the SWCNT surface. It was further observed that bond breaking occurred not only

at the interconnects, but also within the polymer network structure. This caused the formation of dangling polymer chains and some of which that were close to the SWCNT surface, moved with the SWCNT.
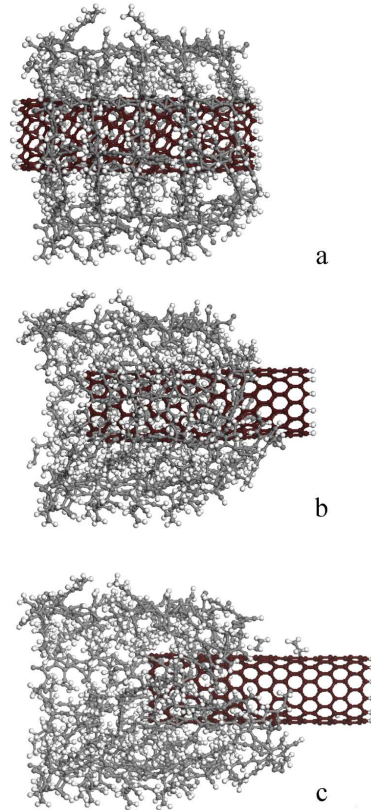
Fig. 18.: SWCNT pull out from an networked PE matrix with no transverse loads applied to the polymer, modeled by using the ReaxFF force field, having capability of bond breaking and formation.

The traction displacement response of the SWCNT was evaluated in the same was as for the RVE modeled with the CVFF force field and is shown in Fig. 19. From the traction displacement response, it can be observed that the peak traction was about two orders of magnitude greater than the case with no bond breaking (Fig. 17). Sharp drops in shear traction were observed, which were typically due to bond breaking

d

e

f
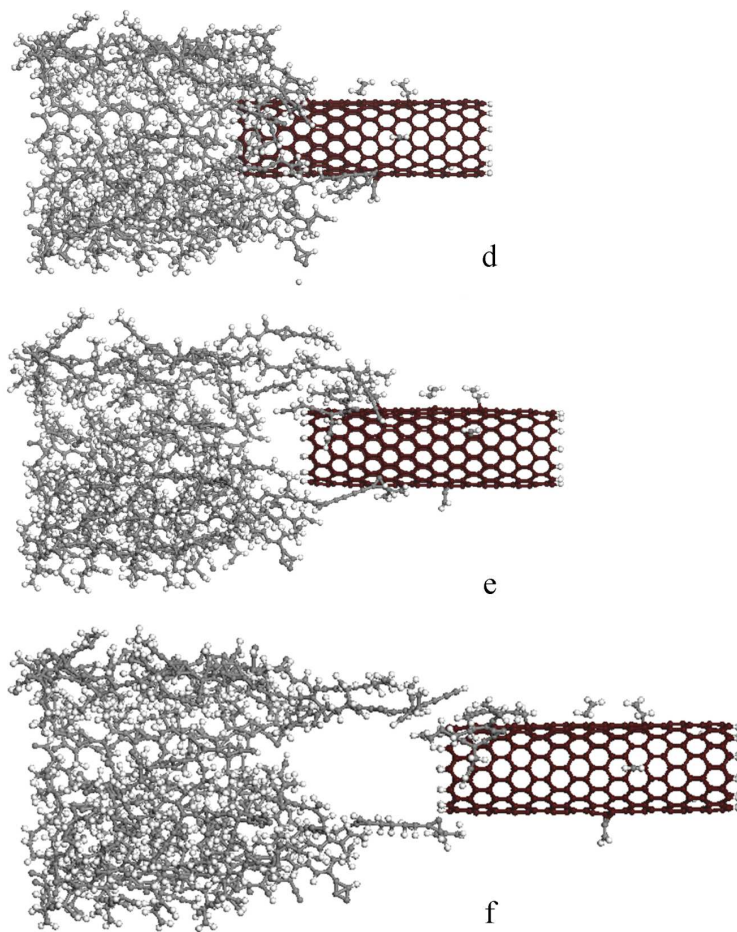
Fig. 18.: Continued.
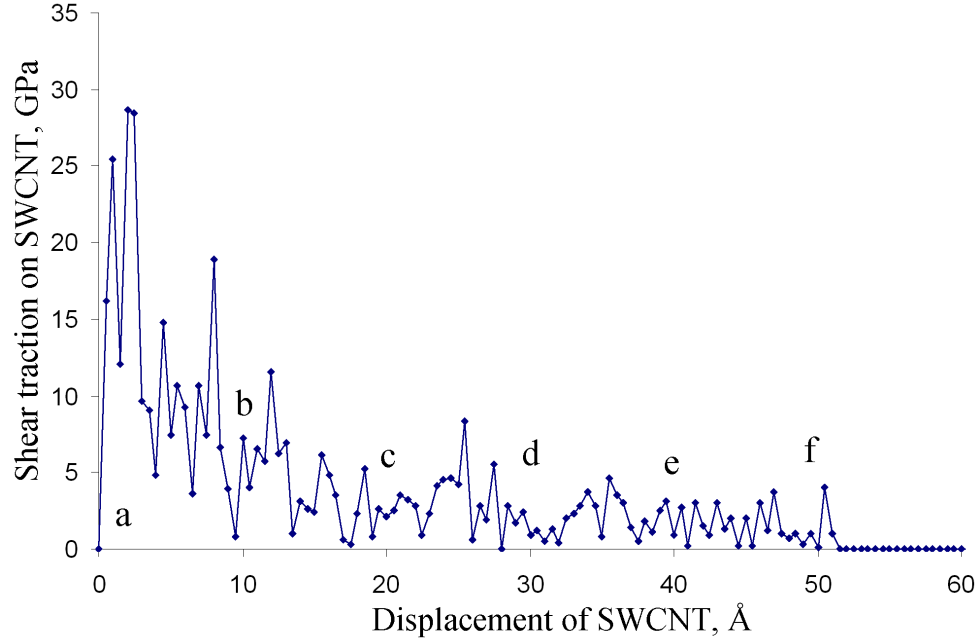
Fig. 19.: Traction displacement response of the SWCNT during pull out from PE modeled by ReaxFF force field.

events occurring either at the SWCNT surface or within the polymer network. With further displacement of the SWCNT and as the interconnects broke, the SWCNT was progressively lesser influenced by the networked PE, causing the shear traction to fall. When the SWCNT was completely separated from the networked PE, the shear traction dropped to almost zero as shown in Fig. 19.

C.   Results for SWCNT pull out from PE matrix under transverse external load

This section describes studies in which SWCNT pull out simulations were conducted in presence of transverse external load acting on the polymer. The behavior of both RVEs, one modeled using the CVFF force field and another with the ReaxFF force field were utilized to perform these tests.

1.   Results for atomistic RVE modeled by CVFF

In investigating pull out separation of the SWCNT from the polymer matrix in presence of external transverse load, the RVE modeled by CVFF (shown in Fig. 12) was subject to compression along the z direction. The constrained portion of the polymer above the SWCNT was displaced in the $-z$ direction and that below the SWCNT was displaced in $+z$ direction to create transverse compression on the SWCNT. The sample for investigation was prepared by displacing the polymer by a total of 12% of the thickness of the polymer in the z direction. Starting from the RVE of Fig. 12, the constrained portions of the polymer both above and below the SWCNT were respectively displaced in $-z$ and $+z$ directions by steps of 0.25Å. For each step, the system was dynamically equilibrated at 100K for 10ps and these steps were carried out until 12% compression was obtained. During these steps, the SWCNT was not constrained and was allowed to deform under the influence of the external load. The pull out stages are shown in Fig. 20.

Fig. 21 shows superimposed traction displacement responses for SWCNT pull out with and without transverse compression. It was observed that the peak shear traction for the case with transverse compression was higher than that with no transverse compression. The reason was the increase in the number of polymer atoms that come under the influence of the SWCNT in the present model. This also caused a longer response wherein the shear traction continued to be non zero at the point where it was zero for the case of separation under no transverse compression. The energy of shear separation was evaluated for this case to be 0.30 J/m².
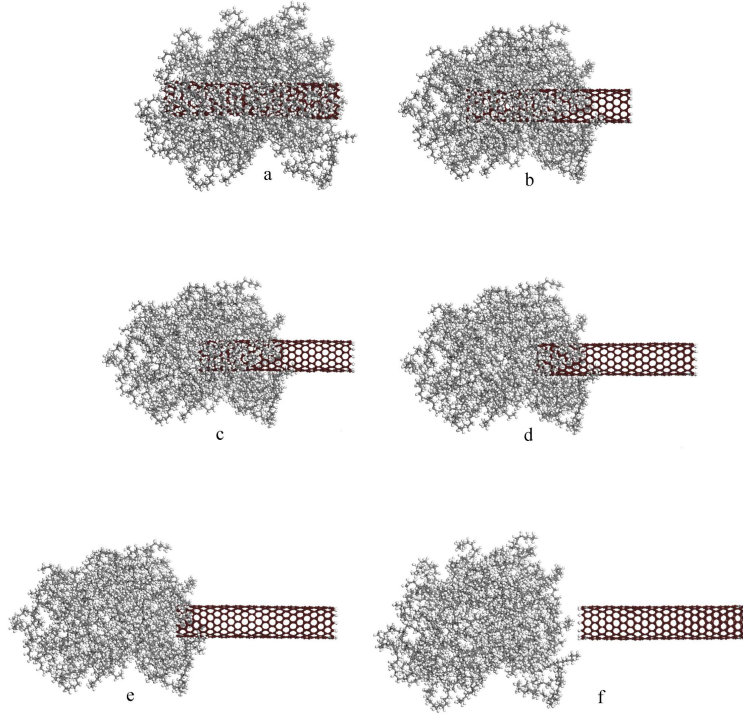
Fig. 20.: SWCNT pull out from an amorphous PE matrix with transverse load applied to the polymer. Only non bonded interactions exist between the SWCNT and PE and the CVFF force field used to model the system.

2. Results for atomistic RVE modeled by ReaxFF

In the case of studying the effect of transverse loading on the behavior of SWCNT pull out from networked PE using ReaxFF force field, the RVE shown in Fig. 13 was utilized. The constrained polymer atoms above the SWCNT were displaced in $-z$ and ones below the SWCNT were displaced in $+z$ directions in steps of 0.25Å, and dynamically equilibrating the system at 100K for 10ps. This procedure was utilized to prepare two samples, one with compression level 12% of the polymer thickness in the z direction and another with that of 20%.

The behavior of the system with 20% compression level is shown in Figs. 22 and
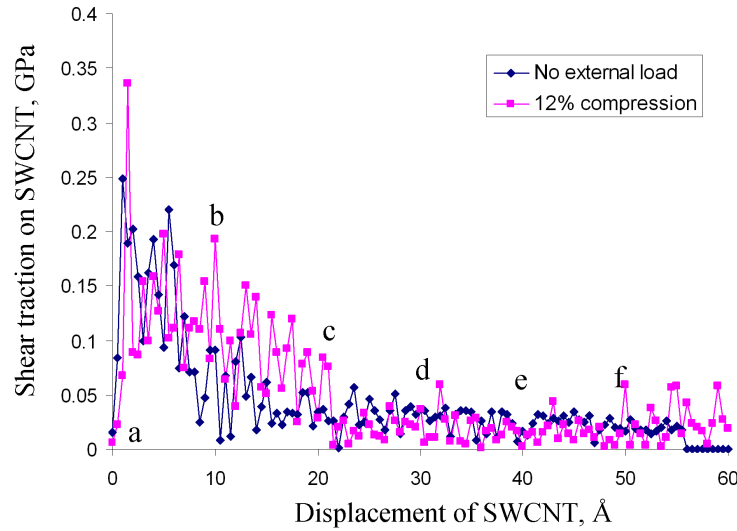
Fig. 21.: Results for SWCNT pull out from an amorphous PE matrix with transverse load applied to the polymer.

22. It can be seen that compression of the polymer results in causing the SWCNT to deform. With application of pull out displacement on the SWCNT, it was observed that the load transfer caused the polymer network to deform in the y direction. With increase in the pull out displacement of the SWCNT, chemical bonds at the interfacial interconnects broke, causing fragments of polymer chains to get severed from the polymer material which stick to the SWCNT surface. It was also observed that the portion of the SWCNT outside the influence of transverse compressed polymer, regained its cylindrical shape (Fig. 22c and Fig. 22d). Further pull out of the SWCNT caused rupture of bonds on the SWCNT surface (Fig. 22e) which deformed its shape even after it eventually separated fully from the polymer material (Fig. 22f).

The shear traction versus displacement response of the two systems, namely with 12% and 20% compression are shown in Fig. 23 along with that of no compression. It can be observed that the peak shear traction for the case with 12% compression is
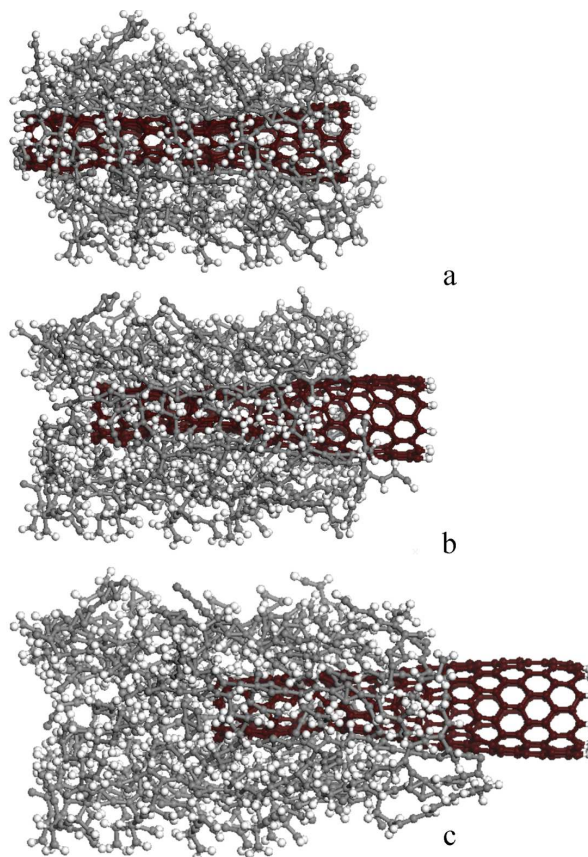
Fig. 22.: SWCNT pull out from a networked PE matrix with transverse load of 20% compression applied on the polymer. ReaxFF force field used to model the system.

d

e

f
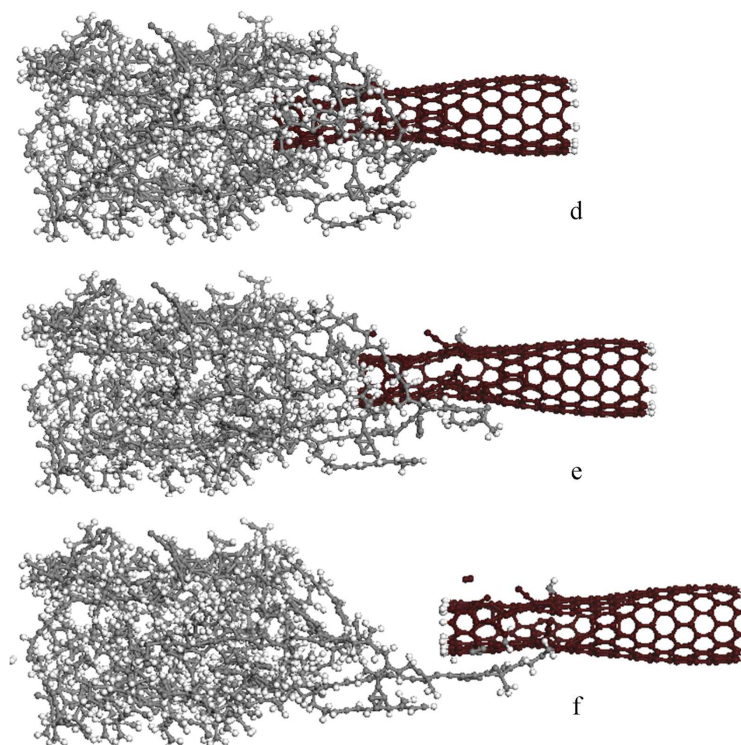
Fig. 22.: Continued.
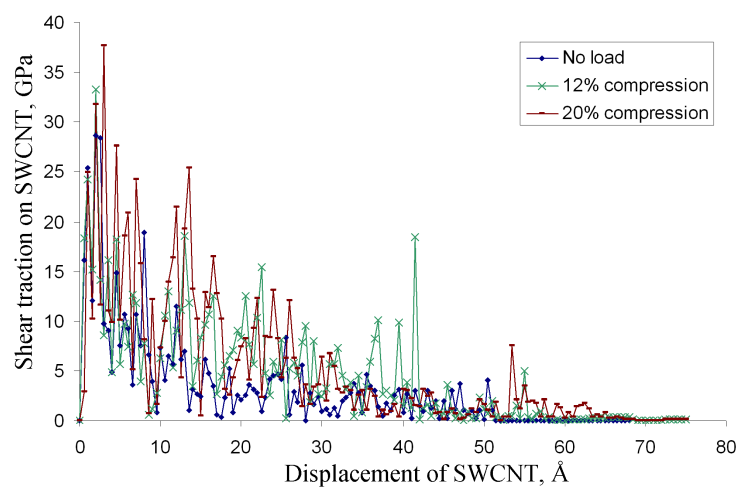
Fig. 23.: Results for SWCNT pull out from an amorphous PE matrix with transverse load applied to the polymer.
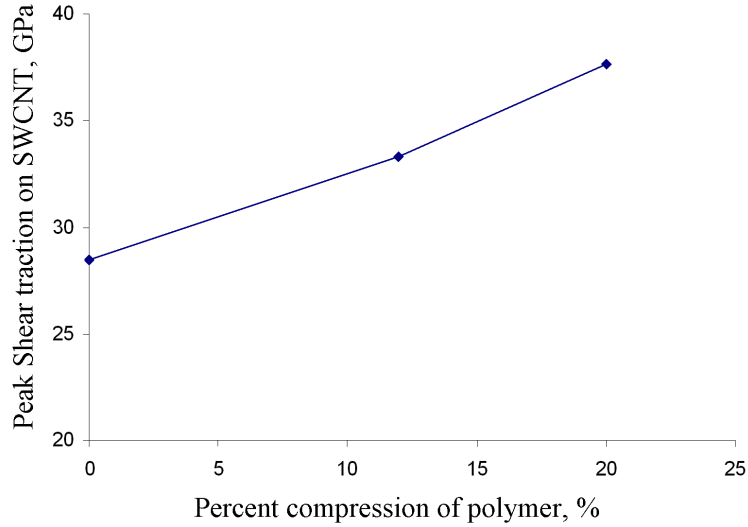
Fig. 24.: Variation of peak shear traction on SWCNT with transverse compression of polymer for RVE modeled by the ReaxFF force field.

greater than that of no compression. Additionally the peak shear traction of the case of 20% compression is greater than that of 12% compression. It was further observed that the increase in compression causes more fluctuations in the traction separation response, because of greater interaction of SWCNT with the polymer atoms and more bond breaking events occurring. The response length increased with the compression level, indicating the enhanced interaction of SWCNT with the network PE.

The variation of the peak shear traction with transverse compression is shown in Fig. 24 and the area under the respective curves, also interpreted as the energy of separation is shown in Fig. 25.

D. Discussion of results

MD studies of SWCNT pull out have been performed for a periodic system consisting of a non-functionalized SWCNT embedded in a polyethylene matrix [50]. In these
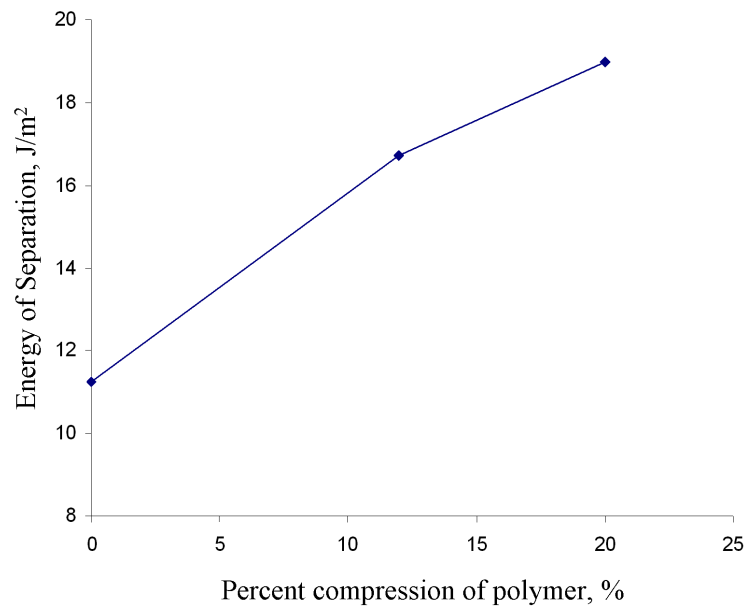
Fig. 25.: Variation of energy of separation with transverse compression of polymer for RVE modeled by the ReaxFF force field.

studies, the SWCNT interacted with the polymer by Van der Waals forces and the displacement of the SWCNT with respect to the polymer did not cause the SWCNT to completely separate from the polymer due to the imposed periodicity of the structure. In the current study, pull out test was conducted using a non periodic system and the SWCNT completely separated from the polymer. The shear traction necessary to cause the relative slippage evaluated in [50] was about two orders of magnitude lesser compared to the present study (of about 250 MPa) with the CVFF unit cell. When the SWCNT is displaced with respect to the polymer in a periodic system, it experiences both a net pulling force due to the applied load, as well as a net pushing force due to the periodic presence of polymer atoms. The resultant effect of these two forces which are opposite in direction, causes the maximum shear traction to be less.

Experimental pullout tests have been performed [61] where unfunctionalized CNTs were pulled out from epoxy matrix using a Scanning Probe Microscope (SPM). The peak shear traction was observed to lie between 25 MPa and 350 MPa for different sets of pull out experiments. The peak shear traction evaluated from the present study (about 25 MPa) lies within the experimentally observed value. Though the material systems composing the matrix material are different (epoxy versus polyethylene), the Van der Waals interactions will be similar, hence the comparison can be valid. The energy of separation for non-bonded interface as evaluated in the present work is within the order of magnitude of that previously calculated by Jiang and coworkers [53] using MD simulations for complete pull out of a SWCNT from an epoxy matrix.

Experimental studies of CNT pullout from a polymeric matrix [109, 110] have measured the fracture energy of functionalized nanotubes to vary between 4 and 70 J/m^2, which lies within the predicted energy of separation for the unit cell modeled with ReaxFF (about 11 J/m^2). MD studies of SWCNT pullout from polymer matrix using reactive force fields have analyzed periodic systems only and have predicted the

interfacial shear strength to range between 30 and 110 MPa.

In the present work, the SWCNT was displaced in steps of 0.50 Åand for each step the system was dynamically equilibrated for 10 ps. Dividing the displacement with the time gives 5 m/s as the displacement rate, which is very high compared to laboratory conditions. It should be noted, however, that the time of 10 ps is chosen to allow the system achieve a dynamic equilibrium at the chosen temperature and pressure conditions. Therefore the pullout tests essentially represent a set of step-wise quasi-static loadings.

MD studies have shown that the presence of covalent bonds on the CNT surface causes a degradation in the elastic modulus [49, 111], strength [111] and strain at fracture [111] with increase in functionalization. This effect was evident in the present study where chemical bonds in the SWCNT broke on application of sufficient pressure.

The shear traction versus displacement response of the ReaxFF unit cell, as given in Fig. 19 shows sharp fluctuations of the shear traction as it falls rapidly on events of bond breaking. These events can be resolved more effectively by choosing a smaller timestep of MD. In all MD studies carried out in this dissertation, the MD timestep was consistently chosen to be 1 fs as this is sufficient to resolve atomic vibrations. A smaller time step, of the order of 0.1 fs can provide better precision of bond breaking and formation events and thereby decrease the sharp fluctuations in the response.

The results presented in this chapter pertain to atomistic level phenomena, localized at the interface between the SWCNT and polymer. However, interpretation or applicability of the atomistic data at the continuum level, can only be made after a size dependence study of the interfacial model. Additionally, MD can only model system sizes as large as 100,000 to up to 1 million which again is limited in capturing non-local contributions to the continuum parameters such as the energy of separation. In a real nanocomposite system, there are many other dissipation sources, in

addition to nanoscale separation, that contribute to the measurements made at the macroscale. These are hard to be captured or resolved by MD simulations presented in the present study.

CHAPTER V

ATOMISTIC MODELING OF MECHANICAL BEHAVIOR OF GRAPHENE
POLYMER INTERFACE*

In the previous chapter, interfacial interactions between polymer and SWCNT were
analyzed through shear separation by means of a pull out test. In the present chapter,
the mechanical behavior of the CNT-polymer interface is described in more detail,
focussing at different modes in which separation can occur, namely opening and
sliding modes. Separation is studied by constructing unit cells of different periodicity
and simulating separation by relative displacement of the two phases. The behavior
of the interface is first studied with respect to Van der Waals interaction only, and
later, a more complex system is analyzed wherein chemical bonding at the interface
is incorporated.

A.   Problem setup

This section describes the procedure for preparing representative MD models for
the interface between the filler and polymeric matrix in the nanocomposite. A list
of necessary tools needed to model these systems has been mentioned. The effect
of boundary conditions on the separation response is studied by applying specific
constraints on the atoms in the model. Separation behavior is simulated by additional
constraints, which represent relative separation of the graphene layer from polymer.
These constraint conditions are described for opening mode separation, sliding mode
separation and sliding mode separation in the presence of tensile and compressive
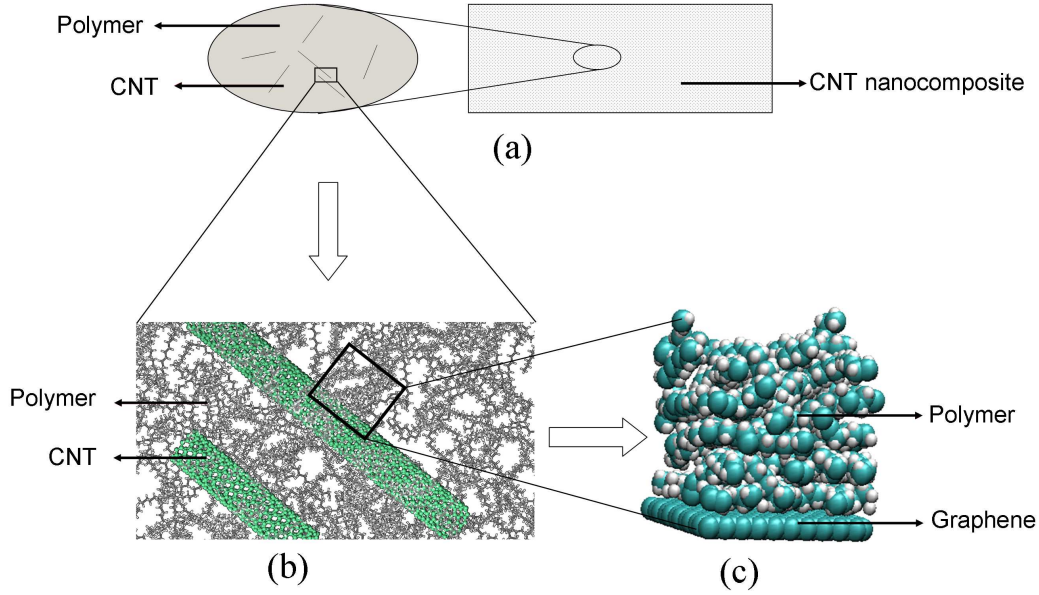
Fig. 26.: Modeling of mechanical behavior of CNT nanocomposite with interfacial effects: (a) nanocomposite at macroscale, (b) molecular detail of CNT and polymer, (c) nanoscale interfacial RVE consisting of graphene and polymer chosen to perform simulations of separation.

normal tractions.

1.   Nanoscale RVEs

The graphic presented in Figure 26 represents the framework of modeling the mechanical behavior of CNT polymer nanocomposites, with incorporation of interfacial behavior between CNTs and polymer. Figure 26a depicts the nanocomposite at the macroscale, consisting of CNTs dispersed in the polymer, in aligned or random orientations, and Figure 26b shows the molecular detail of the interfacial system. The complexity of the CNT-polymer interface is a result of the amorphous nature of the polymer and there is no unique polymer structure that may describe the polymer in

equilibrium with the CNT. The separation behavior at the interface is influenced by individual lengths of the polymeric chains and their orientations, near the vicinity of the CNTs. Additionally, the nanocomposite may contain CNTs of different sizes and chiralities that add to the complexity of the nanocomposite interface. In order to reduce the complexity of the system, to be able to represent it by a simpler structure, a model system was identified from Figure 26b and represented by a polymer-graphene system, shown in Figure 26c since graphene has local structural morphology similar to carbon atoms in the CNT.

In order to simulate long polymeric chains, the computational cost is traditionally economized by coarse graining the polymer, wherein groups of neighboring atoms are treated as individual units which are modelled by computationally simpler force-fields. Grouping neighboring sets of atoms reduces computational cost, but results in loss of atomistic detail. In the current study, short polymeric chains, 60 monomers long (oligomeric length) were chosen, in order to keep polymer lengths in the same length scale as the graphene nanostructure, thereby treating both graphene as well the polymer with the same force-field and thus being able to capture the separation behavior with atomistic detail. This choice of polymer-graphene model also economized the computational cost at the same time and was utilized to conduct MD simulations to obtain interfacial parameters for separation in opening, sliding and combined loading modes. Incorporating the curvature and waviness of the CNT, the results of separation response could be utilized as input to higher scale micromechanical models to obtain bulk mechanical response of the nanocomposite.

2.   Nanoscale unit cell modeled with CVFF

A unit cell of the model system is shown in Figure 27, which consists of the graphene layer, assumed flat, interacting with a film of polymer molecules in the near vicinity.

Also indicated are the periodicity conditions employed in the structure to represent a large domain. The graphene layer was represented with periodicity in its plane and the polymer layer was set up with the same periodicity as graphene, as shown in the figure. No periodicity was assumed in the direction normal to the plane of graphene. This model essentially assumes that, for a low weight percent nanocomposite, interactions among the dispersed filler material are negligible, since they would be scattered by relatively large distances, far from each other. In the present work, it is assumed that there is no functionalization between the graphene and polymer phases and that no chemical bonds exist between the graphene and polymer phases.

Based on its simple chemical structure, polyethylene (PE) was chosen as the polymer matrix material in the present work. The monomer of PE consists of three atoms: an sp^3 hybridized carbon atom which is linked to two hydrogen atoms represented as $-(CH_2)-$. The remaining valence of the carbon atom gets satisfied through polymerization, where additional monomeric units link each other, forming a straight chain. In the present work, the two terminal carbon atoms of each polymer chain are each connected to one hydrogen atom each, making the terminal group $-(CH_3)$. The polymer structure is therefore $CH_3-(CH_2)_n-CH_3$, and in this work, the number of monomer units, n has been kept fixed to be 60. The objective of the current work was to investigate interfacial interactions of graphene with amorphous glassy PE. The glass transition temperature (Tg) of PE is typically in the regime 190-300K, and therefore in present research, the simulations were done at 100K, to conduct separation studies below the Tg of PE. Graphene is a flat structure and consists of sp^2 hybridized carbon atoms forming a planar network, where each carbon atom is connected to three other carbon atoms, forming an angle of 120° between the bonds. Materials Studio Modeling [112] and Cerius^2 [113] were used to prepare atomistic structures, and LAMMPS [108] was used perform molecular dynamics simulations.

Graphics for atomistic representations were generated using Materials Studio Modeling and VMD [114]. The Consistent Valence Force Field (CVFF) [77] was chosen to model interactions between atoms in the present work. This force field is a classical force field and contains parameters for a variety of systems. It is widely used because it has been optimized for organic and polymeric systems including proteins.

The preparation of the periodic structure was dictated by the periodicity of graphene as well as the capability of the MD simulation solver. Fig. 28 shows the different repeat units that can be employed to generate the periodicity inherent in graphene. From the figure, it is evident that the smallest repeat unit needed to generate the graphene geometry using only translation would have non-orthogonal lattice vectors and after replicating the geometry, the graphene layer would be non-orthogonal as well. At the time that this research was performed, the MD solver LAMMPS was not equipped with the capability to perform simulations on non-orthogonal cells and hence, the orthogonal repeat unit of graphene was chosen to prepare the graphene layer in the nanoscale RVE for performing separation tests.

In order to prepare the atomistic structures for simulations in LAMMPS, a model of the polymer independent of graphene was prepared at first, having 3D periodicity. This procedure is described in C where the equilibrium structure of neat polymer was obtained for a chosen set of temperature and pressure conditions. This equilibrated structure was amorphous and in order to verify that the structure was representative in a mechanical sense, the bulk properties (density and moduli) were determined as presented in C. The computational domain (atomistic RVE) up to this point was a 3D periodic cube with edge-lengths given in Table V. At the next step, 3D periodicity conditions were eliminated, and the periodic repeat unit of the polymer was obtained. The computational domain was reconstructed by enclosing the polymer repeat unit within a rectangular prism. Periodic conditions were implemented on this structure
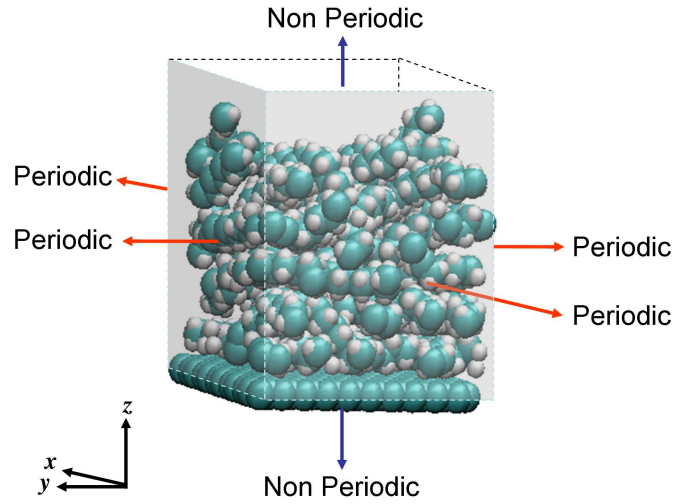
Fig. 27.: Nanoscale RVE with periodic structure in 2D.
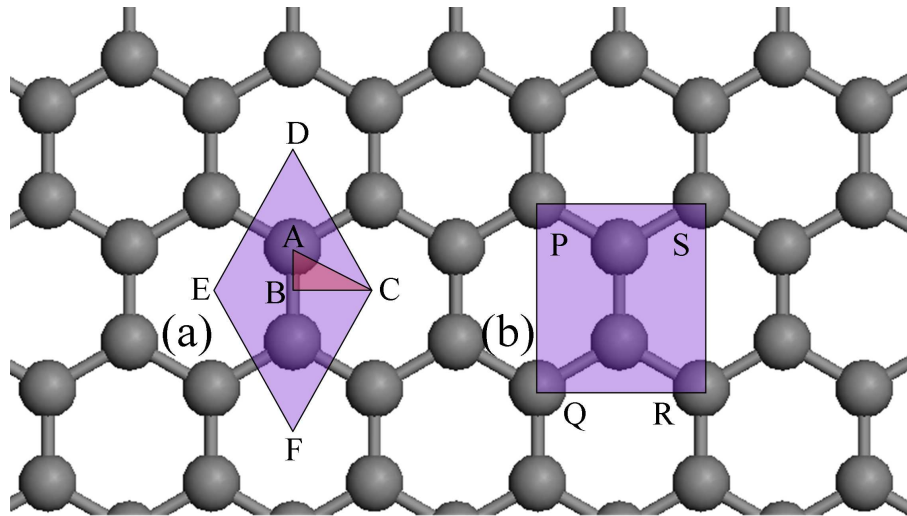
Fig. 28.: Periodic repeat units of graphene geometry, (a) cell ABC is the unit cell which can produce graphene geometry, which utilizes both symmetry as well as translation; cell DEFC is the smallest repeat unit which utilizes only translation, (b) cell PQRS is the smallest repeat unit for producing graphene geometry by translation in orthogonal directions.

along the length and width of the prism (x and y directions), and no periodicity was applied along the height (z direction), which resulted in a 2D periodic RVE. A sheet of 2D periodic graphene was introduced in the $x-y$ plane adjacent to the 2D periodic polymer and the system was re-equilibrated as described in D. No chemical bonds were broken in the polymer chains while transitioning from 3D to 2D periodicity and, additionally, no chemical bonds were created between graphene and polymer since the mode of interaction between the graphene and polymer was assumed to be only given by the non-bonded (Van der Waals and electrostatic) type interactions. The equilibrated model containing polymer and graphene in 2D periodicity shown in Figure 27, contains approximately 1500 atoms, of which 240 of the atoms are the carbon atoms of graphene. This model, consisting of periodicity in two directions, was used to study opening mode separation behavior where the graphene layer was displaced with respect to the polymer in the $-z$ direction.

Table V.: Equilibrated cell parameters and density.

Approx. total atoms	Number of polymer chains	Equilibrated box size (Å side)	Number of graphene atoms
1500	8	23.34	240
3000	16	29.51	336
6000	32	37.19	540
9000	48	42.57	680

The modeling of separation in sliding mode was investigated using two different cases. The first case describes the situation where graphene is embedded entirely in the polymer, while experiencing separation in the sliding mode. As graphene displaces with respect to the polymer in the sliding mode, it comes under the influence of
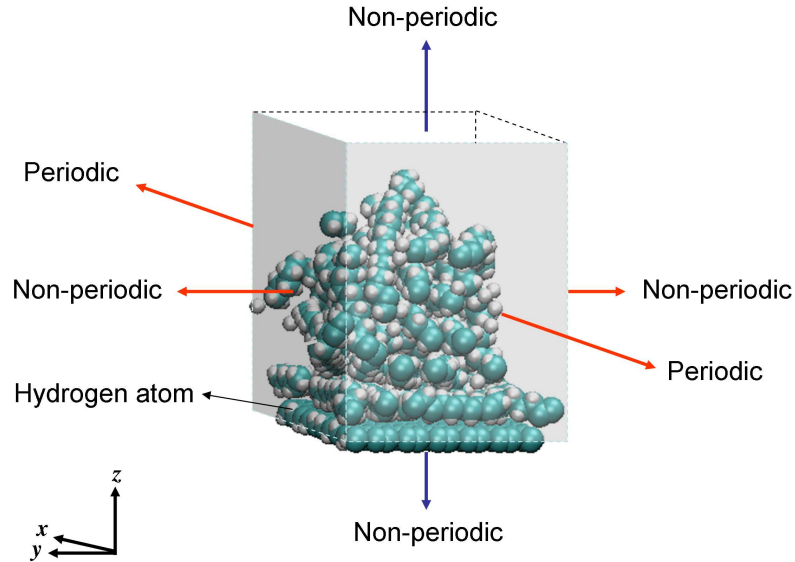
Fig. 29.: Nanoscale RVE with periodic structure in 1D.

new polymer molecules along the displacement direction. Further displacement of graphene causes previous polymer neighbor molecules to be replaced by new polymer molecules. This relative separation has been modelled using the 2D periodic unit cell of Figure 27 where the graphene layer was displaced in the $-y$ direction. Since y direction is the direction of periodicity of the graphene lattice, both graphene as well as polymer atoms moving past the periodic faces of the unit cell reappear on the opposite side.

Another mode of separation in sliding mode can be described where the graphene sheet separates from the polymer entirely. To study this case, a new model was constructed, using the 2D periodic model of Figure 27. Eliminating the periodicity in the y direction, as shown in Figure 29, a 1D periodic structure was obtained. In preparing this 1D periodic model, some chemical bonds had to be broken in the polymeric structure, in order to contain the polymeric chains over the area of graphene. The portions of the chains that extended beyond the non-periodic dimension of graphene were cut.

In this process, whatever chemical bonds had to be broken for both the graphene layer as well as the polymer chains, were completed by hydrogen atoms to satisfy the valence conditions. The process of breaking chemical bonds resulted in creating smaller chain fragments about 10-15 monomer lengths out of the 60 monomers original length. On average about one fourth of the total number of chains were affected in this way. These small fragments were eliminated from the system and resulting structure was re-equilibrated to 100K temperature and 1 atmospheric pressure. In both the sliding mode separation models (2D periodic and 1D periodic structures), the graphene sheet was displaced in the $-y$ direction relative to the polymer.

Transitioning from 3D to 2D periodicity was straightforward and the systems were monodisperse, wherein all polymer chains had the same length. Performing the same procedure for transitioning from 2D to 1D resulted in polymer chains being irregularly arranged over the graphene. This caused several problems with re-equilibration, as the chains would go below the graphene and therefore a test system was difficult to obtain. Thus, a different procedure was adopted wherein the 2D structure was used as the starting configuration and polymer chains outside the periodic edge were cut off, to obtain the required periodicity conditions.

It can be visualized, that after the onset of separation, chains near the interface would largely dominate the separation response; and therefore, to maintain consistency in the current study, separation was investigated keeping polymer chains equal in lengths. In all the samples, the length of the polymer chains was fixed at 60 monomers. In the present study, opening and sliding separation studies were performed over the four system sizes given in table V. The atomistic sizes of the four systems were chosen based on the number of polymer chains in each system. The polymer thickness in each of the samples was approximately equal to the box dimension corresponding to bulk 3D polymer sample as mentioned in Table V.

In all the cases considered in this work, the graphene layer completely occupied a face of the computational domain and the polymer atoms always stayed on one side of the graphene plane and did not cross it. This provided a natural basis to perform surface averaging to obtain interfacial parameters, as opposed to volumetric homogenization where explicit motion of all atoms in the whole computational domain would have to be incorporated.

3. Nanoscale unit cell modeled by ReaxFF

To model separation using the capability to break and create bonds at the graphene PE interface as well as PE bulk, a unit cell consisting of network PE was used. The description of preparing this unit cell is described in Appendix F. To introduce a layer of graphene to the network polymer, in order to create a 2D periodic unit cell, the periodicity of the polymer in the z direction (separation direction) was eliminated and the resulting free bonds were completed by hydrogen atoms. To create bonds for graphene at the interface, several dangling units of PE monomers were attached to the non-periodic PE surface. The valencies of the end atoms of these units were chosen such that they can form an sp^3 bond with the graphene sheet. At the next step, the 2D periodic graphene layer was introduced at a suitable proximity which was approximately equal to a sp^3 bond length. This is shown in Fig. 30.

4. Application of constraint conditions

Experimental observations of separation between nanotubes and polymer chains in nanocomposites are limited at present, due to experimental difficulties in probing nanoscale phenomena. The separation studies undertaken in the present research using MD simulations assume, that interfacial separation is a combination of opening and sliding separation processes, characteristic of a realistic system. Constraint cases

Chemical bonds linking the
polymer chains to graphene
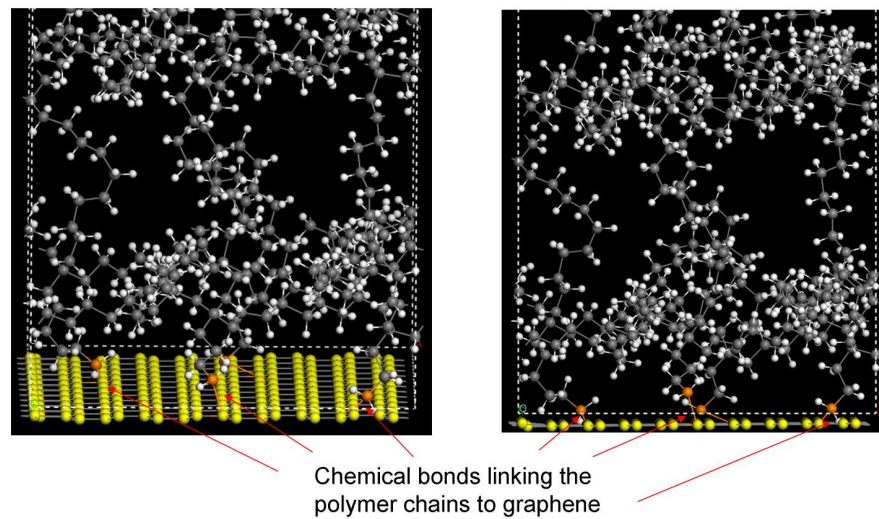
Fig. 30.: Atomistic unit cell chosen to model opening mode separation in 2D with network PE.

All polymer atoms within a layer at the **top** region fixed

All polymer atoms within a layer at the **bottom** region fixed

All polymer atoms fixed

Case A   Case B   Case C
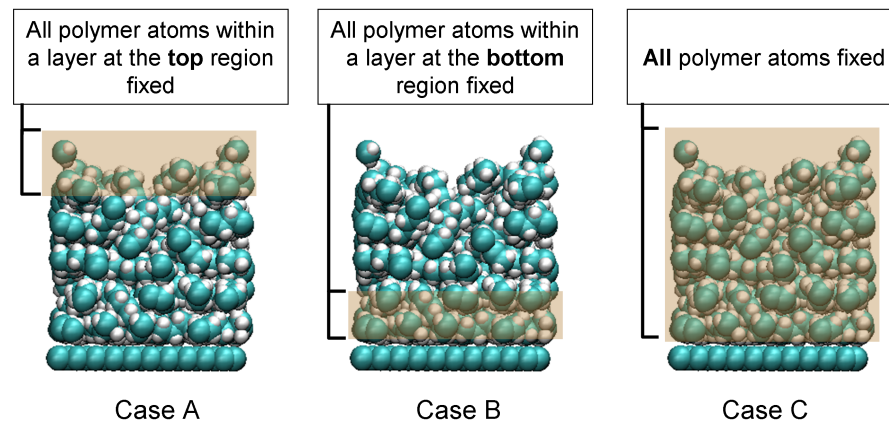
Fig. 31.: Three different constraint conditions employed to study separation. Shaded portion represents fixed atoms. In all cases graphene atoms are incrementally displaced.

have to be imposed in order to separate the two phases from each other, otherwise, moving the graphene will cause all polymer atoms to move together with the graphene and there will be no separation.

Interfacial separation studies were conducted by subjecting the unit cell to the following boundary conditions (Figure 31):

Case A: graphene is separated from the polymer, and a portion of the polymer at the top is fixed in space.

Case B: graphene is separated from the polymer, and a portion of the polymer near the graphene surface is fixed in space, and

Case C: graphene is separated from the polymer keeping *all* polymer atoms fixed.

Case A is representative of a system where the polymer is constrained between two graphene layers, and the graphene sheets are subjected to symmetrical boundary conditions (Fig. 32). In this system, polymer molecules located near the graphene layer are influenced the most by the displacement of graphene. As the distance from graphene increases, the movement of polymer molecules under the influence of graphene reduces. Polymer molecules situated at the center of the polymer region stay fixed with respect to graphene due to symmetrical boundary conditions applied to the system. Case B is a hypothetical system where polymer atoms in close vicinity of graphene are constrained against movement, forcing separation to occur at the interface. Further, Case C is an extension of Case B, where all polymer atoms are fixed and despite interactions occurring between graphene and polymer, the polymer atoms are constrained to stay fixed and force separation to occur at the interface. It can be seen that Cases B and C do not incorporate atomic motion of polymer chains at the interface during separation, and are therefore less realistic compared to Case A, which allows the atomic motion of the polymer chain to be incorporated
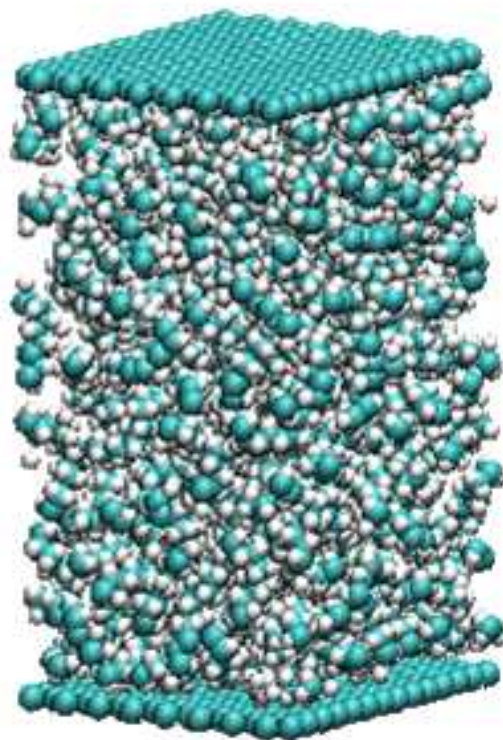
Fig. 32.: Description of Case A constraint condition where a graphene sheet, representing the wall of a SWCNT is separated from another similar SWCNT surface by a large distance. The central portion of the polymer layer is unaffected by symmetrical boundary conditions.

in the separation process. Constraining the polymer atoms in these different ways, separation is performed by displacing the graphene sheet relative to the polymer by applying boundary conditions as given in the following.

a.   Opening mode separation

Opening mode separation is characterized by relative movement of phases in directions normal to the interfacial surface. To study the separation in opening mode, graphene was displaced along the $-z$ direction using the 2D periodic RVE of Figure 27. The separation was performed in steps, where the graphene was displaced by 0.25Å in each step. For Case C, the simulation was static, as none of the atoms were allowed to move after initial equilibration. For Cases A and B, at every displacement step, the system was allowed to dynamically equilibrate for 10 picoseconds. Displacement of 0.25Å in time 10 picoseconds is equivalent to a separation rate of 2.5m/s, which is very high compared to standard laboratory tests. However it was noticed that 10 picoseconds was sufficient to dynamically equilibrate the system (D) and thus the separation could be approximated to be quasi-static for the timescales involved with the atomistic potentials. For all the simulations, a Nose-Hoover thermostat [115] was used to keep the temperature at 100K (except Case C where all atoms were fixed). The influence of polymer on graphene was assessed by monitoring the z component of the total force acting on the graphene obtained by summing the individual forces on each atom. Case A was utilized in simulating various system sizes (table V), to investigate size-dependence on the load-displacement response.

b.   Sliding mode separation

Sliding mode separation is characteristic of relative movement of phases parallel to the interface. To obtain information for separation in sliding mode, graphene was

displaced in the $-y$ direction. The response of separation was evaluated by monitoring the y component of total force acting on graphene obtained by summing the individual forces on each atom. Cases A and C were simulated using the 2D unit cell of Figure 27 representative of an infinite plane of graphene sliding along an infinite film of polymer. Case A was simulated using the 1D unit cell of Figure 29 to study complete separation and to investigate the effect of system size on the load-displacement behavior. The displacement rate of graphene during sliding mode separation simulations was kept the same as in opening mode separation simulations to be 2.5m/s.

c.   Sliding mode separation under normal tractions

Sliding mode separation was investigated further and the influence of normally applied tensile and compressive tractions was studied. Case A was utilized to examine this problem, where the fixed set of atoms of the polymer were displaced in a direction normal to the graphene surface, namely the z direction. Compressive tractions were applied by displacing the fixed atoms in the $-z$ direction while tensile tractions were represented by displacing the fixed atoms in the $+z$ direction. In this way the interface was studied for combined loading comprising of both normal as well as shear components.

In all the simulations, the separation tests were performed to represent a quasi-static process wherein graphene was displaced in normal or shear directions away from the polymer in steps of 0.25Å and the system was dynamically equilibrated at that step before the next displacement step was applied. For simulations pertaining to Case A, all polymeric atoms within a layer of 10Å at the top portion were fixed.

In standard MD codes, a set of atoms are fixed in space by assigning zero forces to them at the beginning of every time step. During the course of simulation, however, finite forces are evaluated on the fixed atoms due to the underlying MD theory. At

the end of the current time step and right before the next time step, the constraint condition automatically assigns zero forces to these fixed atoms, and this information of zero forces is carried over to the next time step and printed in the output script. In the current work, the LAMMPS code was modified to print the finite forces evaluated on the fixed atoms, right before the constraint conditions were applied, and in this way, forces on fixed graphene atoms were obtained for all time steps.

B.   Results for opening mode separation

Figure 33 demonstrates the behavior of the interface for separation in opening mode for Case A for the 1500 atom system. The individual images in Figure 33a are atomic configurations of the polymer-graphene system at different displacement steps of graphene, as it was displaced in the $-z$ direction, away from the polymer. Frame (1) was the structure at the beginning of the simulation, representing equilibrium where the graphene experienced zero average force due to the polymer layer. As the graphene layer was displaced in the $-z$ direction, while the top layer of the polymer was kept fixed, the polymer film underwent stretch, as shown in frames (2) and (3) in Figure 33a. As the graphene sheet displaced further, the polymer chains separated from each other leading to the formation of a distinctive void evident in frame (4). With further displacement of graphene, the void grew in size as observable in frame (5). Continued separation of graphene, (frame (6)) showed that one chain of the polymer moved together with the graphene sheet, separating from the original polymer, while another chain connected the rest of the polymer with the separated chain. As the graphene sheet was separated further, the chains slipped past each other (frame (7)) leading to complete separation as shown in frame (8) where one polymer chain stayed adhered to the graphene sheet, and having separated from the parent polymer layer,

(a)

(b)
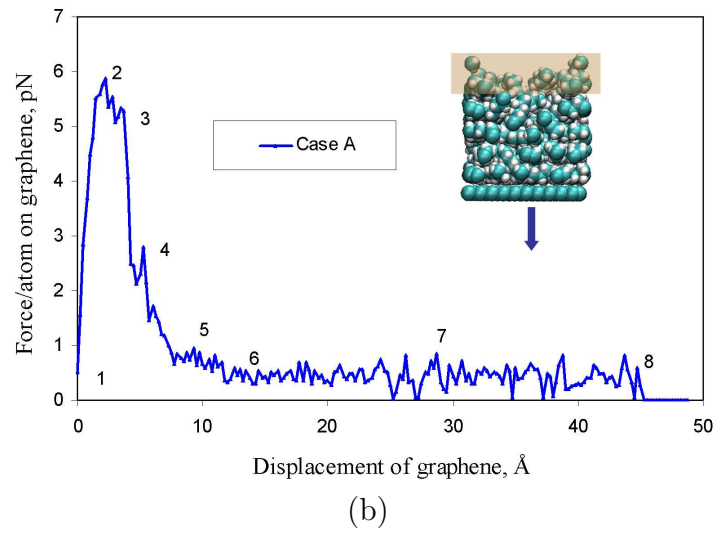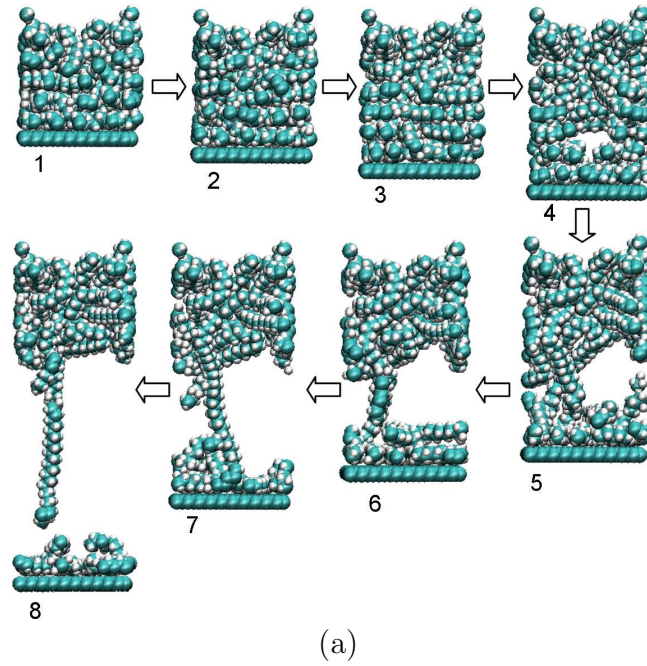
Fig. 33.: Opening mode separation for model containing approx. 1500 atoms with constraint conditions of Case A: (a) structural changes in the polymer during separation. (b) force-displacement behavior of interface during separation.

completely. It should be noted that the polymer chain that got separated from the parent polymer, did not result from the breaking of chemical bonds. The separation occurred due to the sliding motion of the chains as they were held together by Van der Waals forces.

The total force on the graphene atoms was monitored, as graphene was displaced from the equilibrium state. Figure 33b shows the force acting on the graphene atoms normalized by the number of graphene atoms for the duration of the simulation. The individual snapshots shown in Figure 33(a) are also labeled on the force-displacement plot. It can be seen that as graphene was retracted from the polymer, the force per atom increased linearly at first, and reached a maximum of about 6 pN/atom at only 2Å separation (point 2). With further separation of graphene, the force per atom showed a drop at point (3), beyond which it reduced sharply at point (4) indicating reduced interaction between graphene and the polymer, as fewer polymer atoms were available to interact with the graphene. As the graphene sheet was separated further, voids created in the polymer bulk led to lower force, (point (5) and (6)). Beyond point (5), the force per atom continued to be small, mainly governed by the single dangling chain of the polymer. Further displacement of the graphene layer caused complete slippage of the dangling chain which eventually lead to complete separation at point (8). At complete separation, the force per atom went to zero. It was also observed that the length of interaction depended on the length of the polymer chains, more specifically on the length of the chain that separated at the end.

For Cases B and C, the responses are plotted in Figure 34 and it can be seen that they were almost identical. As the graphene was initially separated from the polymer, the force per atom rose to a maximum of about 35 pN/atom. With further separation, this force gradually decayed and went to zero. The similarity of response of Cases B and C indicates that the thermal motion of the free atoms far away from
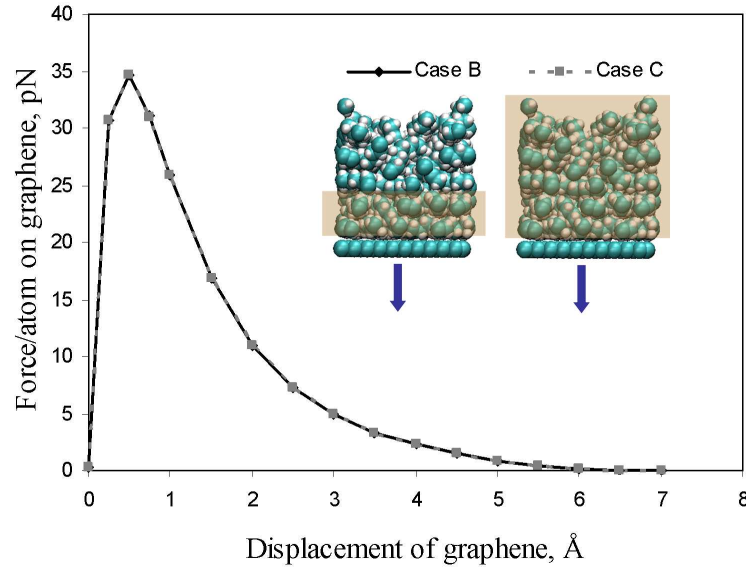
Fig. 34.: Comparison of load-displacement response for Cases B and C for opening mode separation.

the graphene layer do not contribute to the average force response and that, the interaction largely depends on the atoms closest to the graphene layer.

Case C is similar to the system chosen by some researchers [53], [54] and [60], where motion of atoms near the surface is not incorporated. The response obtained in these researches is qualitatively similar to Case C, because it is the nature of the Van der Waals potential that governs the force-displacement response, refer Fig. 35. Since the system is fully constrained, the motion of polymer atoms does not enter into the analysis. Comparing the response with Case A, it can be seen that allowing atoms near the interaction zone to be unconstrained, random instabilities can be captured representing a more realistic situation.

The maximum average force is referred to as the peak average force and the displacement of graphene corresponding to complete separation is defined as the critical separation. Figure 36 compares the force-displacement response for all three cases
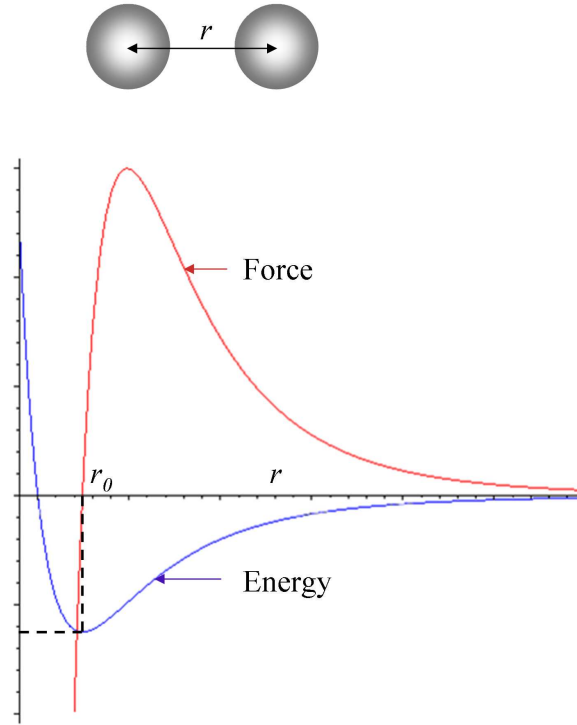
Fig. 35.: Qualitative variation of potential energy and force with respect to distance, r, for two atoms connected through the Van der Waals potential. r_0 pertains to the minimum energy configuration for which the force is zero.

of separation in opening mode. It can be observed that the unconstrained influence of the polymer with the graphene layer in Case A tends to appreciably reduce the peak force per atom, but provide a higher critical separation as compared to Cases B and C. Thus, constraint conditions play a significant role in deciding the force-separation response and are critical in extracting cohesive zone information from the simulations. Case A corresponds to a realistic separation process because it takes into consideration the interactions of molecular chains with the graphene layer and amongst themselves while the boundary conditions are applied far from the interface. Cases B and C do not admit this feature and force the polymer phase to separate
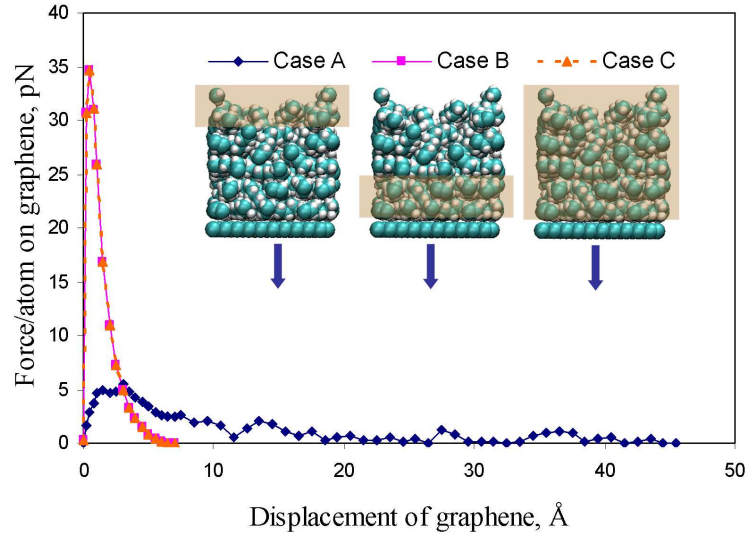
Fig. 36.: Comparison of load-displacement response for Cases A, B and C in opening mode separation.

from the graphene layer, however they are investigated for comparison with Case A.

Case A was subsequently used to simulate the separation behavior for larger system sizes as identified in Table V. To make the separation response applicable for models at higher length scales, the forces were represented as tractions on the graphene surface. This was performed by normalizing the total force on the graphene sheet by the area occupied by the graphene sheet. The response for different system sizes is shown in Figure 37. The responses are plotted against real displacement of graphene in Å(lower x–axis), as well as normalized displacement of graphene (upper x–axis), where the real displacement is divided by the length of polymer chain which is a constant in the present research.

It can be observed for all cases that the nature of the response was nearly the same - consisting of an initial linear response, which continued up to a peak traction, dropped down sharply and gradually reduced to zero. The exact details of the re-
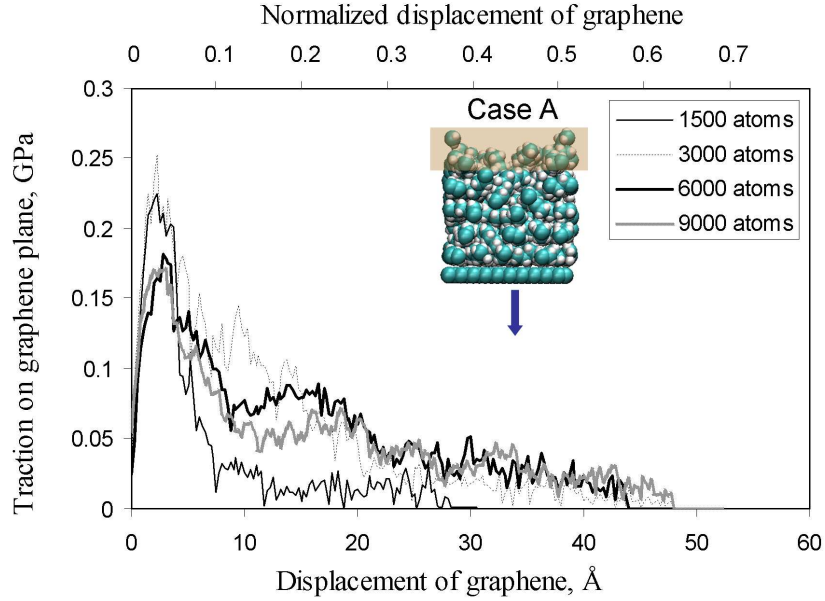
Fig. 37.: Size dependent behavior of traction-displacement response in opening mode using Case A.

sponse may differ from sample to sample for the same case. This variation is caused due to randomness in thermal fluctuations and the polymer configurations at the start of the simulations. It can be further observed that all the curves went to zero at approximately the same displacement of graphene. This is attributed to the length of the chains, which in the present study was taken to be equal in all simulations. It was noticed that the peak traction for simulation sizes with 1500 and 3000 atoms was approximately equal and larger compared to that obtained from the 6000 and 9000 for which almost similar response was observed. Note that the 1500, 3000 and 6000 curves vary in detail, however, the 6000 and 9000 cases show an appreciable overlap. This indicates that, at the 6000 atom size, the system begins to show a converged response for separation in opening mode.

While increasing the size of the system, two contradictory effects occur: increase

in thickness of the polymer layer brings in more atoms to interact with graphene which causes an increase in the total force per atom. However as the size of the graphene layer increases, normalization tends to have a reducing effect on the traction. The effect of these two opposing factors diminishes beyond 6000 atoms indicating that the response begins to get independent of the size of the simulation cell. This is an important consideration while obtaining continuum properties using atomistic simulations.

It can be inferred from Figure 33a that, in a real system, consisting of polymer lengths of several sizes, the critical separation distance would depend on the length of the polymeric chains present just near the interface. During separation, the chains near the interface uncoil and straighten, and therefore govern the critical separation. In the present exercise, for consistent comparisons, all chains of the polymer were taken to be of equal length. Normalization of the displacement of graphene by the size of the straight chain length preserves the response such that it is valid for chains of different sizes.

C.   Results for sliding mode separation

For the sliding mode, the separation process is presented for both 2D as well as 1D periodicity representative of situations where the graphene layer is embedded within the matrix and gets fully separated from the matrix, respectively.

1.   Sliding mode separation using 2D periodic RVE

Shear mode separation in 2D corresponds to the case where the graphene moves in a shear mode while being fully embedded in the polymer. As a consequence of motion, the graphene would lose its immediate neighbors, makes new neighbors and never
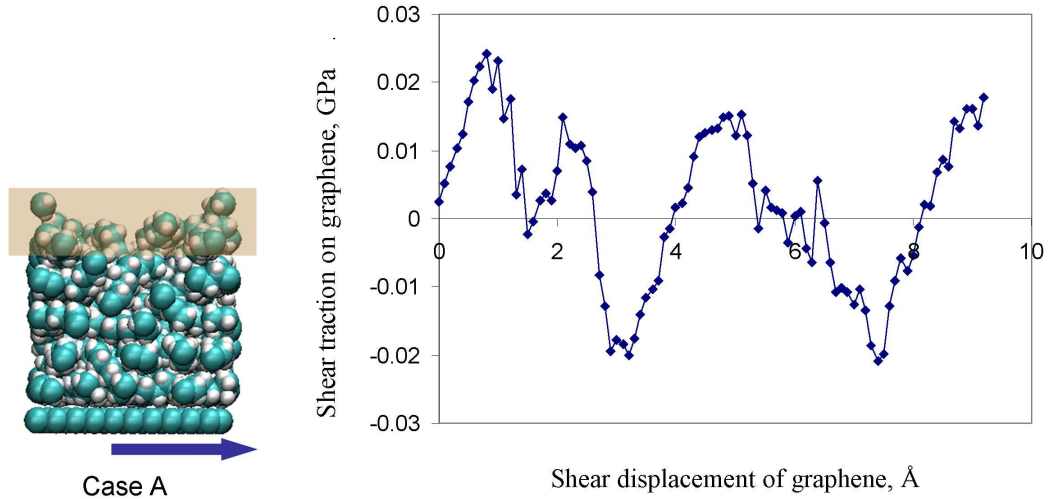
Case A

Fig. 38.: Sliding mode separation using the 2D periodic unit cell and constraint condition of Case A.

separates from polymer entirely. The 2D periodicity ensures that atoms which move outside the unit cell, reappear at the symmetrically opposite face.

For separation in sliding mode, the graphene layer was displaced in $-y$ direction and the y component of the total force on the graphene layer was analyzed. Figure 38 shows simulation of sliding mode separation behavior for Case A for the model containing about 1500 atoms. Here, polymer atoms in the top layer were fixed while those near graphene were free to move. The graphene layer was displaced in uniform steps along the sliding direction ($-y$ direction). The pattern was similar to the case of fully constrained case, containing both positive and negative contributions.

Simulation performed on the 2D periodic system in sliding mode separation for Case C is shown in Figure 39 for a model containing about 1500 atoms. All atoms of the polymer (and graphene) were fixed and not allowed any motion, while graphene was displaced as a rigid body in successive steps in the sliding direction ($-y$ direction). Due to periodicity, whatever atoms left the boundary at one edge, they reappeared on
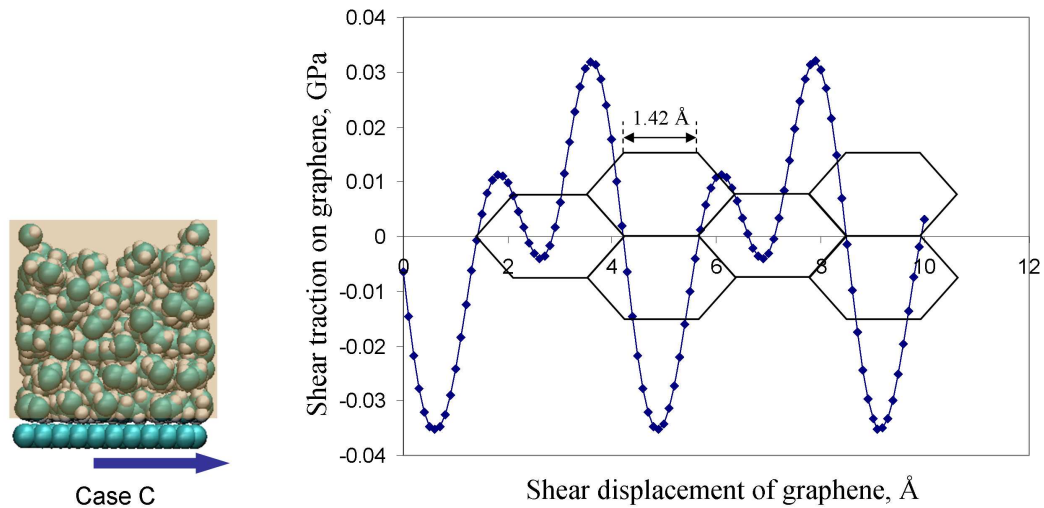
Fig. 39.: Sliding mode separation using the 2D periodic unit cell and Case C constraint condition. Also shown in the graphene structure for reference; the periodicity of the response is same as the periodicity of the graphene structure.

the opposite edge. This gave rise to the positive and negative force values and it can be also noted that the position of the peaks and zeros on the plot were separated by distances inherent in the graphene geometry. (Notice that the force at zero displacement is not exactly zero. This value depends directly on the minimization tolerance chosen - a more tighter tolerance tends to limit it closer to zero. In the current work the tolerance was chosen to be 0.0001 Kcal/mol.)

Figure 40 compares the magnitude of the tractions acting on the graphene layer for opening and sliding mode cases for the case of 2D periodicity. The curve for opening mode separation, averaged by the area of graphene has been taken from Case C in Figure 34 and that for sliding mode case has been taken from Figure 39. The peak traction is about 13 times higher in opening mode compared to sliding mode for the same system.
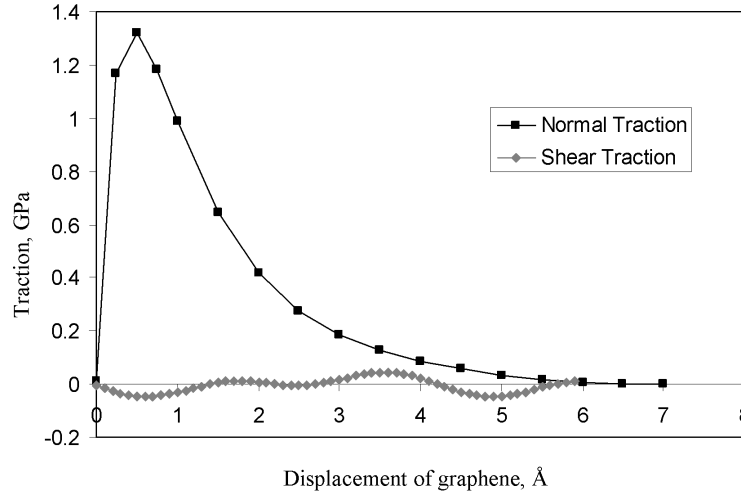
Fig. 40.: Comparison of traction magnitudes obtained using constraint condition of Case C in opening and sliding separation modes.

2. Sliding mode separation using 1D periodic RVE

To obtain the traction-displacement response for the situation where graphene completely separates from the polymer in sliding mode, periodicity was broken in the direction of sliding separation (y direction) as depicted in Figure 29. In this model, the graphene sheet completely disengages from the influence of polymer. Figure 41 depicts a typical 1D separation case for Case A. The response consisted of an initial steady growth of force per atom, followed by several fluctuations representative of instabilities at the interface. The force-displacement response gradually diminished, and eventually, at the end of the separation process, one polymer chain remains with the graphene layer after separating from the bulk polymer. For both opening as well as sliding separation in the current work, it can be noticed that separation occurs within the polymer material (Figure 33 and Figure 41). This feature has also been observed experimentally in Transmission Electron Microscopy (TEM) imaging of CNT-polymer nanocomposites [29]. It should be noted that these effects are likely
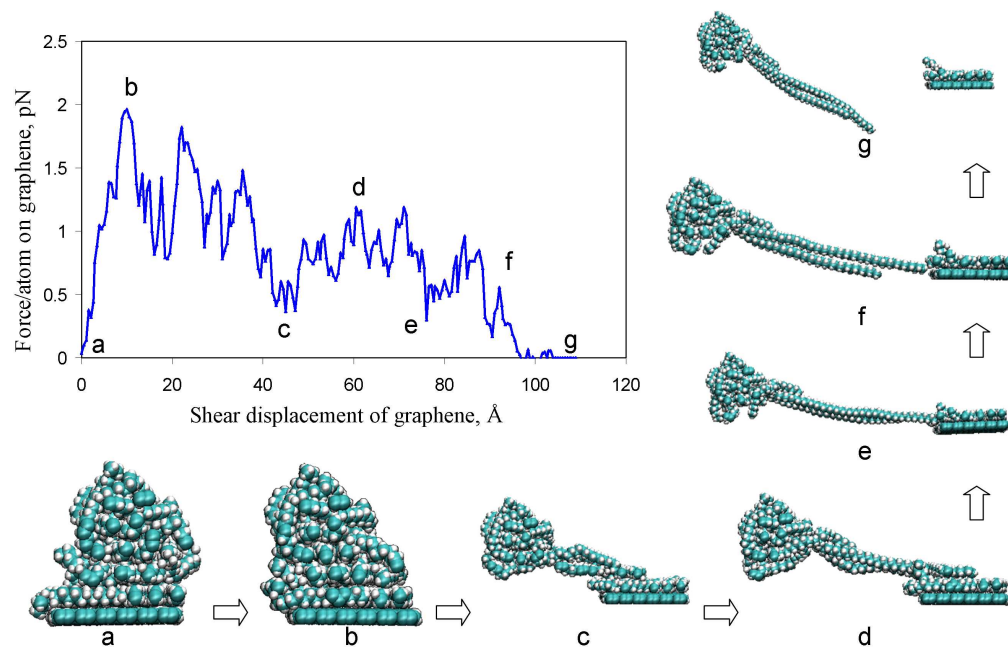
Fig. 41.: Sliding mode separation using the 1D periodic unit cell and constraint conditions of Case A.
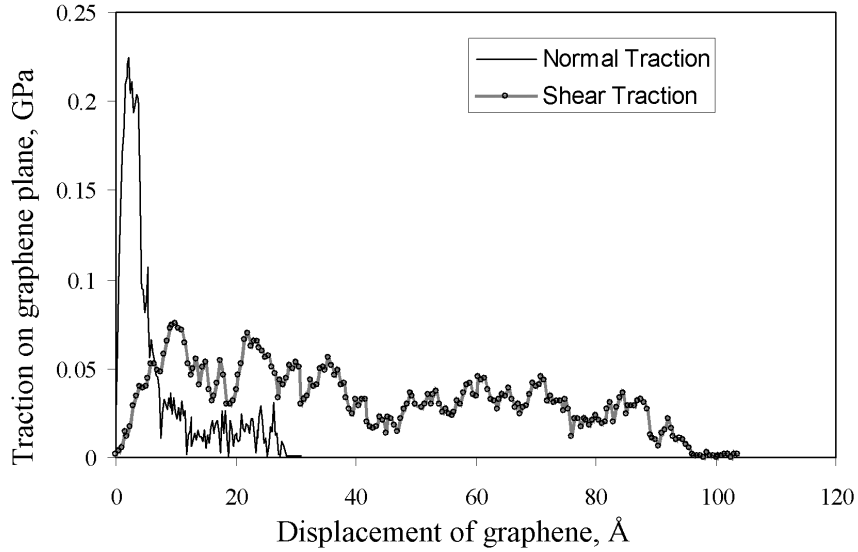
Fig. 42.: Comparison of traction-separation response in opening and sliding separation modes for Case A constraint condition.

to be captured when a complete dynamics incorporating motion of atoms near the interface is performed together with the utilization of a full force field. Studying separation without incorporating the dynamics at the interface does not provide these features. In Figure 42 comparison is made between the opening and sliding separation responses both obtained for Case A. It can be noted that the peak normal traction was only about three times in magnitude, compared with the shear traction. This shows that the fully constrained system (Figure 40), where this ratio was about 13, over-predicts the response. The size dependent study performed with various system sizes of table V for sliding mode separation using Case A is shown in Figure 43, with the responses plotted against both the real shear displacement of graphene (in Å) as well as the real displacement normalized by the fixed length of polymer chain.

When the size of the atomistic RVE is small, the traction-separation response is more sensitive to the random fluctuations in the polymeric structure adjacent to
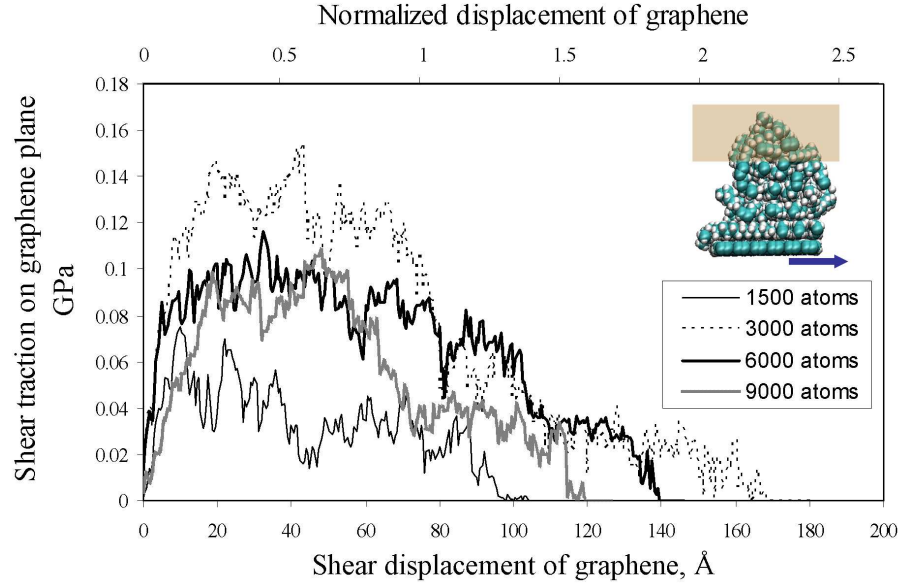
Fig. 43.: Size dependent behavior of traction-separation response in sliding mode separation using Case A constraint condition.

graphene. However, as the size of the computational domain is increased, the effect of these fluctuations is diminished, since the average traction on graphene is evaluated from the forces on all graphene atoms. However, there is still a difference in the results between RVEs containing 6000 and 9000 atoms indicating that in order for full convergence to be achieved, a larger RVE is necessary.

The shape of the force-displacement response in complete separation cases of both opening as well as sliding modes as studied above, resembles the cohesive law in quasi-brittle materials [116]. The response comprises of an initial linear part, leading to the peak force and then gradually decays, ultimately leading to separation. As observed from the size dependence studies, beyond a certain number of atoms, the system response approaches limiting behavior. This shows that the phenomenon of interest, i.e. the separation process, ceases to depend on the size of the system for the

chosen set of boundary conditions. The separation law eventually tends to behave as a system property and gives justification to connect to higher scale modeling.

Table VI.: Cohesive zone model parameters for opening mode separation using constraint conditions of Case A.

No. of atoms	Work of separation (mJ/m^2)	Peak Traction (MPa)
1500	129.108	224.432
3000	276.065	252.319
6000	265.924	181.427
9000	246.525	170.616

The cohesive zone parameters, namely peak force and work of separation, are shown in tables VI and VII for opening and sliding modes of separation, respectively. Figure 44 and Figure 45 show the variation of the cohesive zone parameters with system size. Also shown are opening mode separation parameters evaluated by [54] using the methodology of [53] (where the model consisted of an infinitely long CNT surrounded by polymer) and case C for 1500 atoms. It can be observed that despite the large difference between peak tractions, the cohesive energies are closer together. The fully constrained case has higher peak tractions and smaller cut off interaction distances, which together result in the work of separation being comparable.

D. Results for sliding mode separation under normal tractions

The results of previous sections were special cases where the graphene sheet was free of any normal loads through the polymer layer. However in a real system, the interface undergoes combined loading, and separation occurs under the influence of tractions.
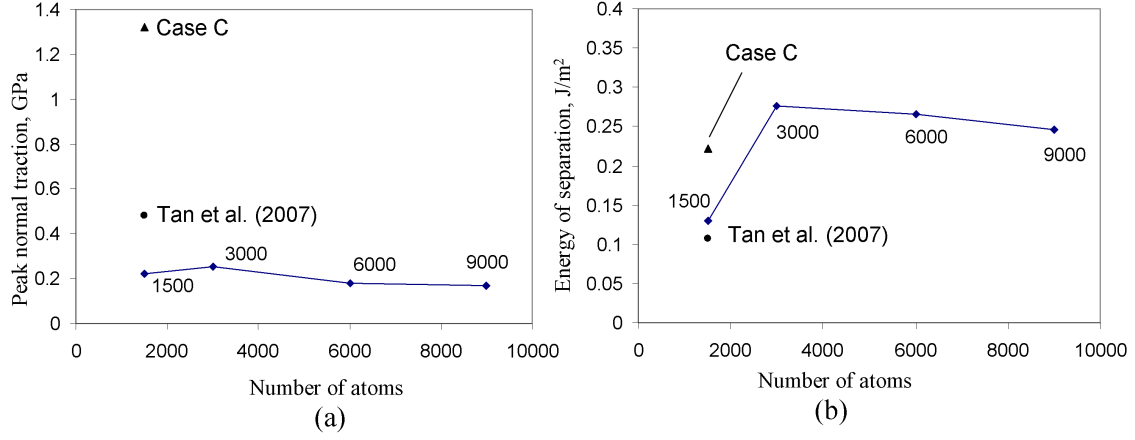
Fig. 44.: Cohesive zone parameters for opening mode separation obtained using different system sizes and constraint condition of Case A (a) peak normal traction, (b) energy of separation.

Table VII.: Cohesive zone model parameters for separation in sliding mode using constraint conditions of Case A.

No. of atoms	Work of separation (mJ/m^2)	Peak Traction (MPa)
1500	165.871	74.938
3000	591.568	154.525
6000	473.821	116.466
9000	331.650	108.276
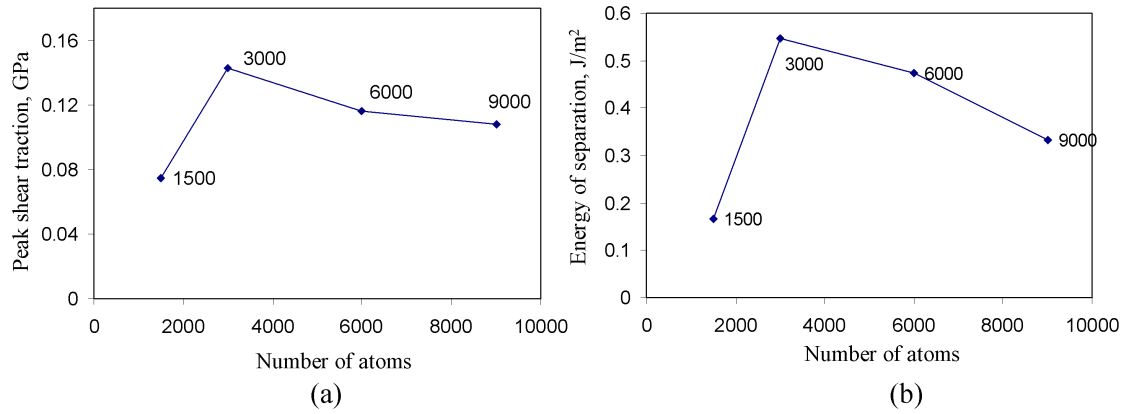
Fig. 45.: Cohesive zone parameters for sliding mode separation obtained using different system sizes and constraint condition of Case A (a) peak shear traction, (b) energy of separation.
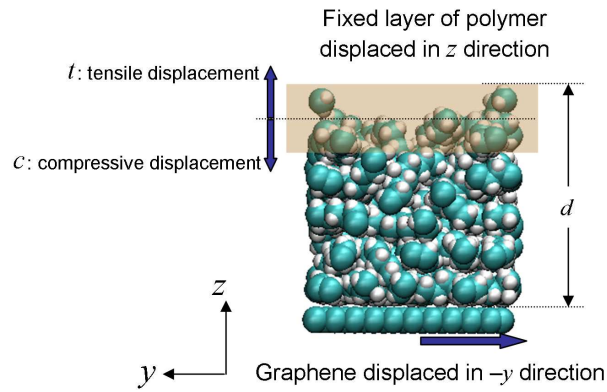
Fig. 46.: Schematic of sliding mode separation under normal traction. Fixed layer of polymer in Case A displaced in $+z$ direction to apply compressive, and $-z$ direction to apply tensile loading on graphene. Graphene displaced in $-y$ direction to represent sliding mode separation.

In this section, results are presented for the case where graphene is separated from the polymer in sliding mode while being loaded with tractions in the normal direction. Normal tractions were applied by imposing compressive and tensile displacements on the polymer in the normal direction (Figure 46). Case A was utilized to study the influence of combined loading, and the fixed set of atoms (represented by the shaded region in Figure 46) were displaced by amount c along $-z$ direction, and by t along $+z$ to apply the compressive and tensile loadings respectively. The magnitude of c was chosen to be proportional to the thickness of the polymer layer (d) , which is also representative of the size of the RVE. Both 2D as well as 1D periodic systems of sections 1 and 2 respectively were undertaken for study.

1.   Sliding mode separation under normal tractions for 2D periodic RVE

The RVE of 2D periodicity models the situation where graphene is always in the influence of the polymer and never separates completely from it. This RVE is appropriate for modeling of interfacial constitutive behavior of nanocomposites. Using the nanocomposite RVE of section 1, the top (fixed) layer of polymer was displaced by amount c in the $-z$ direction. At first the atomistic model for c equal to $0.04d$ was prepared. The total displacement of $0.04d$ was performed by successively displacing the fixed layer of atoms in the polymer model for Case A by 10 equal steps of $0.004d$, and for each step, the system was dynamically equilibrated for 100K and 1 atmospheric pressure over 10ps time intervals. This process of applying total displacement in small successive steps represents a quasistatic process and prevents to expose the system to any sudden changes. After reaching the equilibrated compression of $0.04d$, the sliding test was simulated as before, by displacing graphene in $-y$ direction. This process of displacing the fixed layer of atoms of polymer and performing sliding mode separation tests was performed for different compression levels, for c equal to $0.08d$,
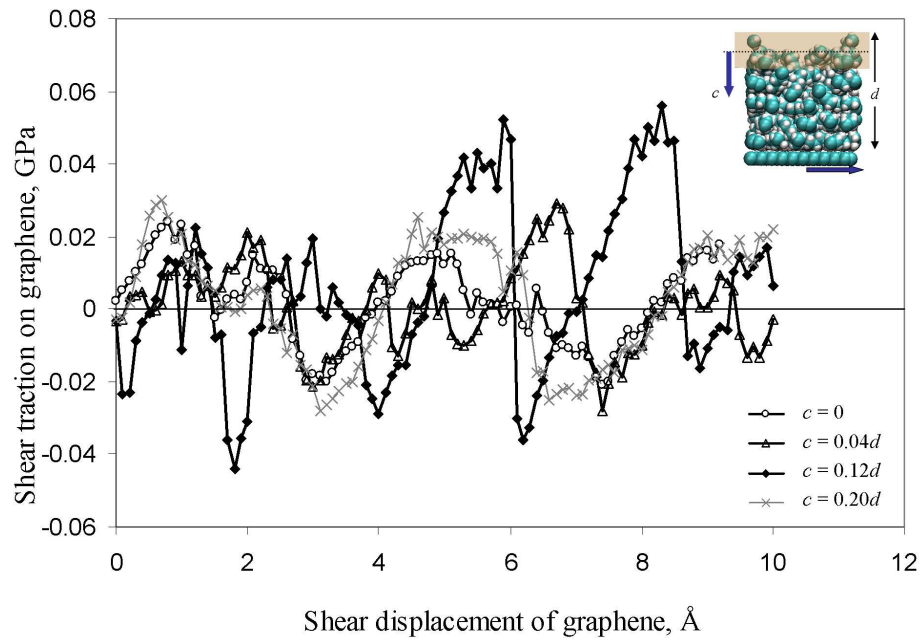
Fig. 47.: Traction-displacement response for sliding mode separation with compressive normal loading for the system containing 1500 atoms, constraint condition of Case A and 2D periodicity.

Fig. 48.: Variation of (a) peak traction and (b) energy, with compression of polymer layer for system containing 1500 atoms with 2D periodicity using constraint conditions of Case A.

$0.12d$, $0.16d$ and $0.20d$. The individual responses are shown in Figure 47 along with the response for no normal loading (responses for c equal to $0.08d$ and $0.16d$ are not shown for clarity). Qualitatively, the response for all compression levels is similar to that with no loading, comprising of repeated increase and drop in shear traction, which changes direction, due to the periodic boundary conditions employed. The absolute value of the peak traction for the different levels of compression is plotted in Figure 48a. It is observed that the peak initially shows a rise with the compression level, reaching a maximum at compression level corresponding to $c = 0.16d$, and begins to drop with further compression. The initial rise can be attributed to more polymer atoms participating in interaction with the graphene layer, but with added normal loading, the compressed polymer phase gets distributed more uniformly over the graphene layer. Since the boundary is periodic, and interactions at the interface are through Van der Waals forces, a graphene atom begins to experience uniform interactions in the y direction from the polymer atoms which leads to canceling of the y component of force and results in an overall drop in traction (Figure 47) and

hence the peak traction as well (Figure 48a).

Table VIII.: Effect of compression on peak traction and energy for opening mode separation for the 2D periodic RVE containing approx. 1500 atoms using constraint conditions of Case A.

Compression, c	0	$0.04d$	$0.08d$	$0.12d$	$0.16d$	$0.20d$
Energy (mJ/m²)	2.069	2.045	3.012	5.044	2.255	2.244
Peak traction (MPa)	24.168	29.251	50.300	55.938	38.924	30.069

To obtain the measure of energy expended in displacing the graphene in sliding mode for the model with 2D periodicity, the maximum area under the traction-displacement plot was calculated. It was observed that the maximum area corresponded to the part of response having the peak traction. Energy evaluated for different levels of compression is plotted in Figure 48b and the trend of the energy is same as that of the peak traction, rising up to the compression level of $c = 0.16d$ and falling thereafter to almost the same value as that for the case with no normal loading. Table VIII presents the numerical values of energy and peak tractions for this case.

The load-displacement response for tension was studied by investigating ten systems, which were individually set up by displacing the fixed top portion of the polymer in the $+z$ direction in increments of $0.04d$ reaching up to $0.40d$. The traction-displacement response for sliding separation under the influence of tensile tractions, is shown in Figure 49, for normal tensile loadings up to $0.20d$, and Figure 50, for loadings from $0.24d$ to $0.40d$. The peak traction and energy are plotted in Figure 51a and Figure 51b respectively and presented in table IX. The energy values correspond to the part of the response consisting of peak traction and are observed to follow

Fig. 49.: Traction-displacement response for sliding mode separation with tensile normal loading for the system containing 1500 atoms with constraint condition of Case A and using the 2D periodic unit cell. Results shown for tensile loading up to 20% of the thickness of the polymer layer.

Fig. 50.: Traction-displacement response for sliding mode separation with tensile normal loading for the system containing 1500 atoms with constraint condition of Case A and using the 2D periodic unit cell. Results shown for tensile loading from 24% to 40% of the thickness of the polymer layer.
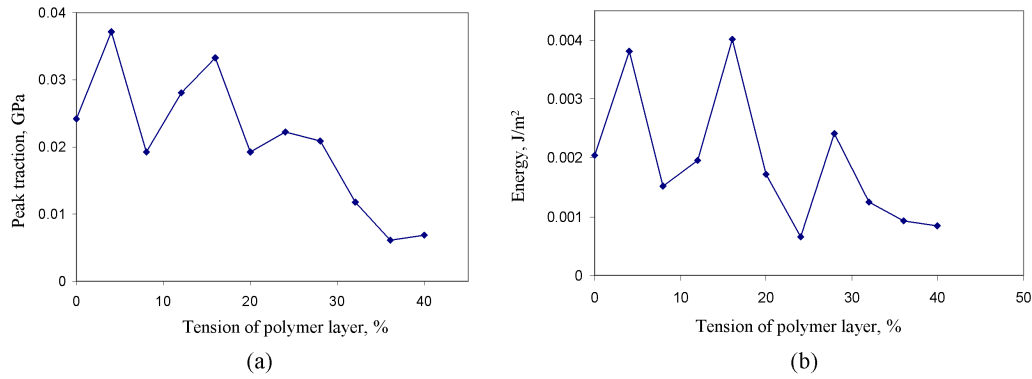
Fig. 51.: Variation of (a) peak shear traction and (b) energy, with tension of polymer layer for system containing 1500 atoms with 2D periodicity and constraint condition of Case A.

a similar trend as peak traction. As the top fixed portion of the polymer was displaced in a direction away from graphene, two processes occur simultaneously. The polymer chains near the graphene sheet get distributed less uniformly which causes tractions to increase, while separation between graphene and polymer atoms reduces the forces of interaction causing the tractions to drop. Eventually, at large separation, the tractions and energy values, show a decreasing trend, as the interaction between the polymer atoms and graphene atoms reduces appreciably.

2. Sliding mode separation under normal tractions for 1D periodic RVE

The RVE of 1D periodicity pertains to the situation wherein graphene eventually separates from the the influence of the polymer, completely. The effect of normal loading was investigated by starting with the model systems of section 2, and subjecting the fixed sheet of graphene to compression and tension by displacing the fixed layer of the polymer in $-z$ and $+z$ directions respectively by $0.04d$, $0.08d$, $0.12d$, $0.16d$ and $0.20d$. This procedure was performed for the 1D periodic model-RVEs consisting of

Table IX.: Effect of tension on peak traction and energy for opening mode separation for the 2D periodic RVE containing approx. 1500 atoms using constraint conditions of Case A.

| Tension, t	0	$0.04d$	$0.08d$	$0.12d$	$0.16d$	$0.20d$
Energy (mJ/m^2)	2.044	3.805	1.523	1.961	4.014	1.719
Peak traction (MPa)	24.168	37.156	19.278	28.112	33.247	19.183
Tension, t	$0.24d$	$0.28d$	$0.32d$	$0.36d$	$0.40d$	
Energy (mJ/m^2)	0.649	2.418	1.245	0.932	0.840	
Peak traction (MPa)	22.271	20.940	11.759	6.048	6.874	
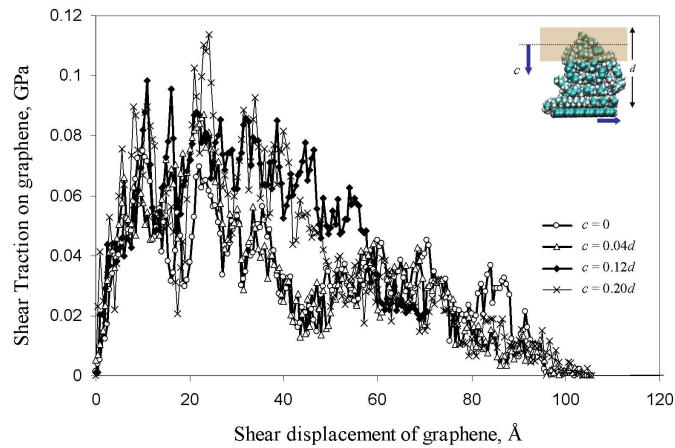
Fig. 52.: Traction-displacement response for sliding mode separation with compressive normal loading for the system with 1500 atoms, constraint condition of Case A using the 1D periodic RVE.
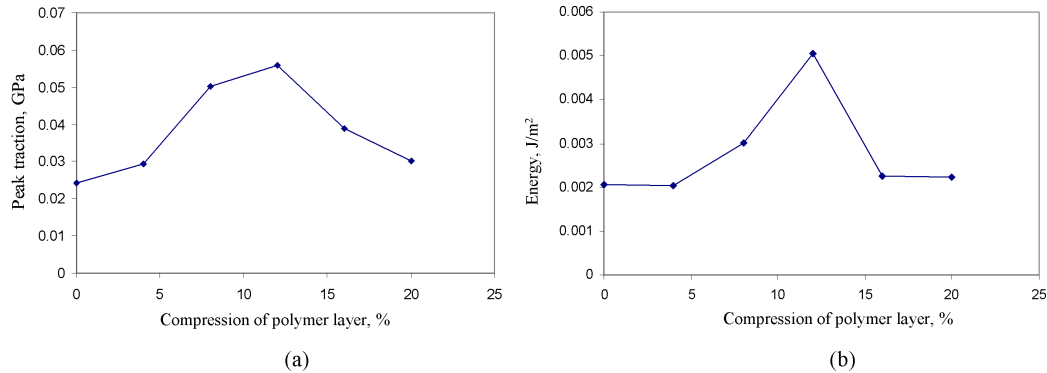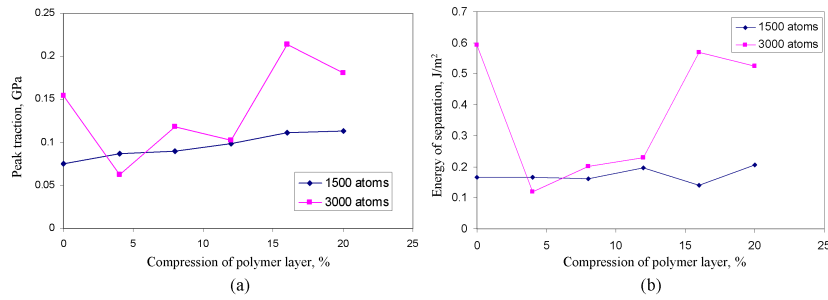
Fig. 53.: Variation of (a) peak traction and (b) energy, with compression of polymer layer for system containing 1500 atoms with 1D periodicity and Case A constraint condition.

1500 and 3000 atoms. Figure 52 shows the response for sliding mode separation for the 1D RVE containing 1500 atoms using constraint conditions of Case A, with compressive displacements of $0.04d$, $0.12d$ and $0.20d$ applied on the fixed set of polymer atoms. Table X shows the numerical values of the peak shear traction and energy of separation for compressive displacements of $0.04d$, $0.08d$, $0.12d$, $0.16d$ and $0.20d$ RVEs containing 1500 and 3000 atoms. Figure 53a shows the trend of peak traction for compressive loading for RVEs consisting of 1500 and 3000 atoms, and it can be observed that compression causes an overall increase in the peak traction. Energy of separation for compression loading, plotted in Figure 53b for RVEs with 1500 and 3000 atoms, is represented by the area under the corresponding traction-displacement response. It was observed that, as the polymer was sequentially compressed against the graphene sheet, more polymer molecules were interacting with the graphene. Since energy of interaction is largely governed by the polymer chains separating at the end, this feature was random and therefore no overall trend was observed in the energy variation of the case with 3000 atoms.

Figure 54 shows the traction-separation response for the 1500 atom model for

sliding mode separation in 1D periodic unit cell with tensile loaded applied in the $+z$ direction. The peak shear tractions and energies of separation obtained for RVEs containing 1500 and 3000 atoms are tabulated in table XI. Figure 55a shows the variation of peak traction and Figure 55b that of energy of separation respectively, for models containing 1500 and 3000 atoms. It can be observed that the application of tensile loads causes both the peak traction as well as the energy to reduce with load.

Table X.: Effect of compression on peak traction and energy for opening mode separation for 1D periodic RVE containing approx. 1500 and 3000 atoms using constraint conditions of Case A.

	1500 atoms		3000 atoms	
	Peak traction	Energy	Peak traction	Energy
Compression, c	(MPa)	(mJ/m^2)	(MPa)	(mJ/m^2)
0	74.938	165.871	154.525	592.342
0.04d	87.136	167.353	62.240	119.538
0.08d	89.429	162.705	118.260	201.944
0.12d	98.333	196.459	102.771	229.234
0.16d	111.618	140.045	213.756	568.582
0.20d	113.675	205.883	180.309	523.680

The peak traction evaluated from 1D periodic RVE is about 5 times higher as compared to that from the 2D periodic RVE. This is because the graphene atoms in the 2D periodic RVE always have interactions with polymer atoms lying on both $+y$ as well as $-y$ directions and thus the overall force reduces due to contributions from each side, whereas in the case of 1D periodic RVE, sliding displacement causes the
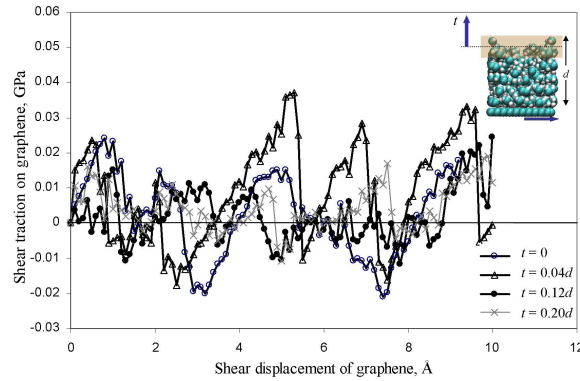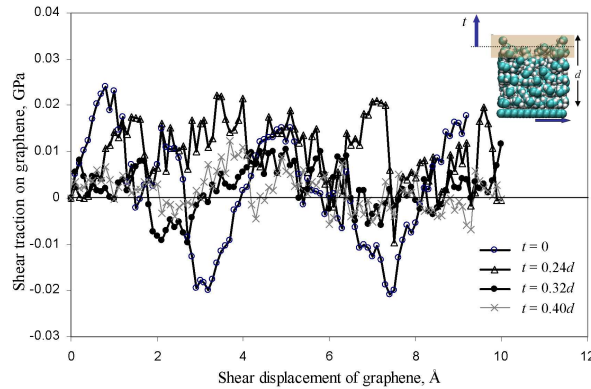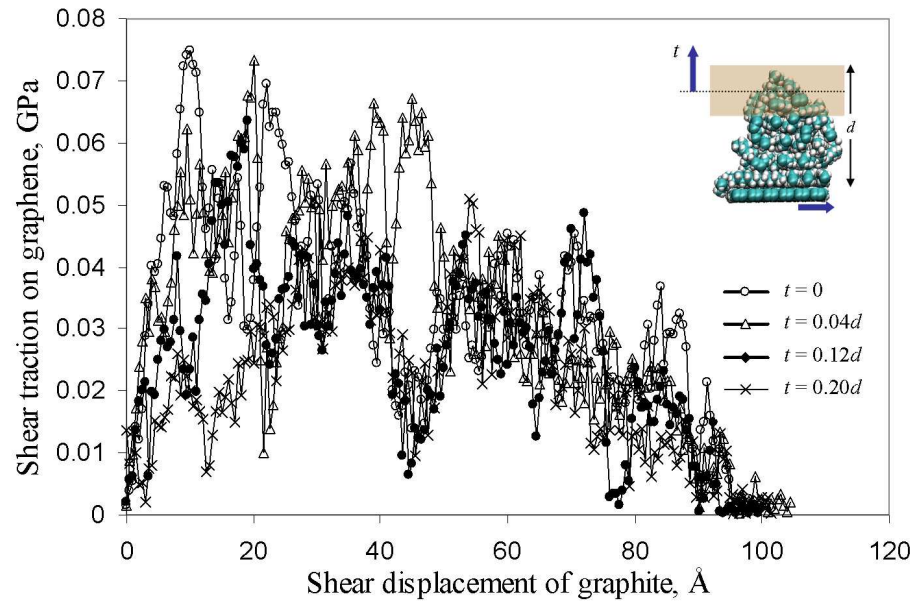
Fig. 54.: Traction-displacement response for sliding mode separation with tensile normal loading for the system with 1500 atoms, constraint conditions of Case A using the 1D periodic unit cell.
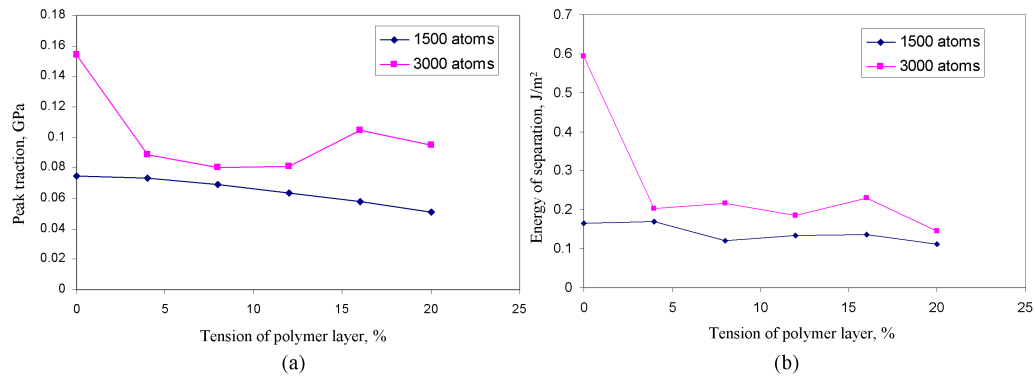
Fig. 55.: Variation of (a) peak traction and (b) energy, with tension of polymer layer for system containing 1500 atoms with 1D periodicity and Case A constraint condition.

Table XI.: Effect of tension on peak traction and energy for opening mode separation for 1D periodic RVE for RVEs containing approx. 1500 and 3000 atoms using constraint conditions of Case A.

Tension, t	1500 atoms		3000 atoms	
	Peak traction (MPa)	Energy (mJ/m²)	Peak traction (MPa)	Energy (mJ/m²)
0	74.938	165.871	154.525	592.342
0.04d	73.331	169.420	88.408	203.298
0.08d	69.173	121.003	79.916	215.751
0.12d	63.511	133.681	80.736	185.966
0.16d	57.716	136.824	104.403	229.283
0.20d	50.882	112.140	94.884	143.823

graphene to shift to one side of the polymer and thus all the forces of interaction are lined up in one direction. In the case of energy, the values for 1D periodic RVE is 100 times higher compared to the 2D periodic RVE. For the 1D periodic RVE, only the part of the response containing the peak traction is considered, because the response is both positive as well as negative while the graphene is always interacting with the polymer. This contribution is small compared to the case of 1D periodic cell where the graphene separates from the polymer completely.

E. Discussion of results

MD simulations were performed to examine the interfacial behavior in the graphene-polymer system to model the constitutive mechanical behavior of the interface. A small atomistic window near the interface was analyzed for interfacial separations

using molecular dynamics simulations. Assuming the separation process to be a combination of opening and sliding modes, simulations were performed with different constraints, periodicities and loading conditions. The load-displacement response of the system was primarily studied and separation parameters were obtained. These are appropriate to be utilized in higher level continuum or micromechanics model to predict the overall behavior of a system containing large number of such sub-systems.

The molecular dynamics simulations described above form the first phase of material analysis and simulation. Though termed as the RVE, the simulation window actually represents local interactions near the interface. To describe a continuum level, both localization as well as independence of unit-cell size have to be included. Since the mechanism of separation at the nanoscale is not fully understood by either theory or experiment, it was proposed that the actual process could be a combination of the opening and sliding mode separations. The models of CNT-polymer interface currently available in the literature only deal with the sliding mode separation within the ideology of a pullout test. In the model of [47], the CNT is bonded to fixed polymer short-chains by covalent chemical bonds. The peak traction was demonstrated to be about 5GPa when 85 chemical linkages were attached to the CNT as short polymer chains, and 0.5GPa when the number of such polymer attachments was reduced to 5. The calculations in the present work, which are based on absence of covalent interactions, predict the peak traction to be about 108 MPa for a 9000 atom case. In [47] the separation force is directly obtained from the bond-energy of the covalent linkage. This methodology does not incorporate polymer morphology, which plays a vital part in the separation process. As observed in the present work, different boundary conditions influence the response differently (figures 36, 40 and 42) and the response is mainly governed by the polymer morphology and atomistic motion during separation (figures 33 and 41), thus demonstrating that complete polymer structure

must be accounted for, while studying such atomistic systems.

The current research has led to not only new predictions of material behavior, but also new comparisons with experimental data. In an experimental setup, [61] evaluated the peak shear traction for nanotubes by performing pull out tests from a polymer matrix. MWCNTs were dispersed in the polymer matrix and there were no functional linkages joining the MWCNTs with the matrix so interaction between the phases was essentially by Van der Waals forces. Individual MWCNTs were pulled out from the matrix using the tip of the scanning probe microscope (SPM). It was observed that application of pullout force on the outermost CNT caused the entire MWCNT to get pulled out from the matrix, thus showing that inner tubes of the MWCNT were adhered to the outer layers and had lesser interaction with the polymer matrix. The pull out experiment was performed for MWCNTs of different diameters using the SPM tip and the peak shear traction measured for large diameters MWCNTs up to 24nm was found to be 96±15 MPa. In the present research, peak shear traction evaluated for complete separation of graphene (which is ideally a tube of infinite radius) from the polymer was 108 MPa (table VII). This comparison serves to be a preliminary validation of the MD model used in the present study.

The energy of interaction evaluated by [60] in which static separation tests were performed for systems comprising of graphite interacting with polymer, occurs in the range 0.1–0.2 J/m^2 and is similar to that evaluated in the present study (Fig. 44, table VI) of about 0.209 J/m^2. [53] and [54], who also evaluated the energy of separation for the graphene polymer system without incorporating true motion of atoms evaluated this figure as 0.107 J/m^2. It was demonstrated in the present research, that performing static separation studies by forcing separation at the interface (Case C) causes the peak force to get appreciably high, yet the energy evaluated by the force-displacement plot is about the same as compared with case when full atomic motion

is incorporated (Case A). This occurs because the critical separation is reduced significantly (Fig. 36) when the motion of atoms near the interface is not incorporated. It should be noted that for the fully constrained cases in which the interaction between the phases is non-bonded, the response is actually that of the atomistic potential used to model the interactions. Thus, Case C of the present work, the models of [53], [54] and [60] all show the functional form of the potential used, because the models considered in the respective studies do not incorporate explicit motion of the atoms. When motion of atoms near the interface is incorporated, the model conforms more to a realistic system and therefore suitable for evaluating interfacial parameters.

The work of separation or the cohesive energy evaluated in the present research ($0.2 - 0.3$ J/m^2) is smaller than experimental observations of functionalized nanocomposites by about two orders of magnitude. The separation tests performed in the current exercise have considered only non-bonded interactions (Van der Waals and electrostatic) at the interface. Energetically the non-bonded interactions are very weak compared to covalent bond interactions, and since the non-bonded interactions are the dominant interactions at the interface in the current model, they largely govern the response.

In connecting the nanoscale effects to higher level length scale models, this work addresses the effect of size of the simulation window over the response. This step is important because nanoscale simulations are very sensitive to the size of the simulation box and the number of interacting atoms. This step also becomes critical since the connection has to be made to continuum level properties. Moreover, as the size is increased, it was noticed that the response approached limiting behavior. The simulations for combined loading showed a trend in sliding separation behavior as normal loads were applied in compressive and tensile modes. For the case when the filler material was embedded inside the matrix, it was seen that compressive loads cause

an increase in the peak traction up to a threshold beyond which the peak traction decreased. This behavior was primarily influenced by the periodicity of the model and non-bonded interactions between the matrix and filler. Combined loading for the case when the filler separated entirely from the matrix (representative of a pull out test), however, showed that normal compression caused an increase in peak traction and normal tension resulted in decreasing the peak traction.

F. Summary and conclusions

In this research, molecular dynamics was used to study the graphene-polyethylene interfacial mechanical behavior. Periodic unit cells of 2D and 1D periodicity were utilized to model the graphene-polymer interface. Using the Consistent Valence Force Field, separation tests were performed for this interface in opening and sliding modes. The influence of different boundary conditions on separation was examined. Separation in sliding mode was studied together with normal loading and size dependence studies were conducted to obtain limiting behavior in the force-displacement responses. This information was used to obtain separation parameters namely peak force and work of separation.

MD simulations performed on the graphene-polymer interface system indicated that separation occurred within the polymer phase. During the separation process, a few polymer chains, particulary those near the graphene surface, stayed adhered to graphene and slipped away from the remaining polymer. This caused voids to form in the polymer region which grew in size leading to complete separation. Though the interface modeled in the study was characterized by non-bonded Van der Waals potential and did not contain any covalent linkages, yet, separation was found to occur within the polymer region and not at the interface. This showed that mechanical

interactions between graphene and polymer chains are stronger than those among the polymer chains. It was also observed that the choice of constraint conditions had a significant impact on the force-displacement response for the interface. Incorporation of motion of the polymer atoms near the interface captured the instabilities occurring during the separation process. It was also inferred that the critical separation distance in the force-displacement response would depend over the lengths of the polymer chains separating at the end of the separation process.

Predictions of the current research have led to new comparisons with experimental work. The interfacial peak shear traction evaluated for the graphene-polymer interface in this research was found comparable with that of the multi-walled carbon nanotube-polymer interface, measured experimentally from a pull out test. Additionally, interfacial behavior leading to separation occurring within the polymer region, as observed in the simulations in the present research, was found to be consistent with experimental findings.

CHAPTER VI

OVERALL CONCLUSIONS

The linear force-displacement response of single walled carbon nanotubes (SWCNTs) was studied by developing the atomistic Hessian matrix method. This method was utilized for solving structural boundary value problems leading to the evaluation of linear moduli of the SWCNTs. The atomistic Hessian matrix, traditionally used to perform transition state and vibrational analysis on nanoscale systems, was shown to be useful in evaluating the linear stiffness of these systems as well.

The present research enabled the comparison of the atomistic Hessian matrix evaluated using experimental data (from the *zone folding method*), quantum mechanical calculations and the Tersoff Brenner Potential. It was observed that the sub-matrices of the atomistic Hessian matrix corresponding to the first nearest neighbor interaction for both zone folding method as well as for quantum mechanically evaluated atomistic Hessian matrix were in good agreement. The components of the atomistic Hessian evaluated from the Tersoff Brenner potential differed significantly from the other two except the component corresponding to the Carbon-Carbon bond stretching mode, which was comparable. It was additionally observed that the atomistic Hessian matrix obtained using the quantum mechanical calculations was qualitatively more accurate in explaining the Poisson's effect in SWCNTs compared to the experimentally derived Hessian in the *zone folding method*.

The computation of the Hessian matrix using quantum level calculations, though an expensive calculation, yet, once evaluated, the atomistic Hessian matrix method can be used to compute the linear force displacement behavior of atomistic systems for a variety of boundary conditions and hence compute the structural stiffness in different modes. More importantly, the atomistic Hessian matrix method has the

additional advantage over the energy method wherein individual components of the Hessian matrix evaluated from quantum calculations can be compared with force constants obtained from experimental observations. Vibration analysis using quantum mechanical calculations on SWCNTs showed that application of very small axial strains leads to shifts in natural frequencies consistent with experimental observations. The frequency shifts demonstrate that SWCNTs deviate from exhibiting linear behavior even for very small strain levels and therefore the energy method should be used with caution.

To analyze interfacial behavior of carbon nanotubes (CNTs) in their applications as filler materials in nanocomposites, molecular dynamics was used to study the CNT-polyethylene and graphene-polyethylene interfacial mechanical behavior. Using the Consistent Valence Force Field to model system with no bond breaking, and the ReaxFF Force Field to incorporate bond breaking, detailed separation tests were performed on these interfaces. Interfaces of CNT and graphene with both straight chain as well as cross linked polyethylene (PE) were modeled in the separation tests. Mechanical behavior in different modes of separation, including opening and sliding mode was observed for a variety of constraint conditions, including combined loading. The information generated was used to obtain separation parameters namely peak force and work of separation under different loading environments and this knowledge has applicability to continuum level models.

Simulations of CNT pull out from network polymer using ReaxFF Force Field showed that bond breaking events occur both at the interface as well as in the polymer away from the interface. It was observed that the peak traction for opening mode separation was two orders of magnitude greater for bonded interface compared to the un-bonded interface, modeled using the CVFF Force Field. Pull out tests with transverse load for a bonded interface modeled using ReaxFF Force Field showed that

the interface can cause the rupture of CNT bonds during pull out.

The MD simulations on graphene-polymer interface system with straight chain polyethylene showed that separation phenomenon occurred within the polyethylene phase. Even though the interface was characterized by non-bonded Van der Waals potential, yet, separation occurred within the polymer region and not at the interface, indicating that mechanical interactions between graphene and polymer chains are stronger than those among the polymer chains. It was also observed that the choice of constraint conditions played a significant role on the force-displacement response for the interface. Incorporation of motion of the polymer atoms near the interface captured the instabilities occurring during the separation process and was a major finding of the present research. It was also inferred that the critical separation distance in the force-displacement response would depend over the lengths of the polymer chains separating at the end of the separation process.

To refine the interfacial model, future work will be focused on additional studies to determine the effect of separation rates on the mechanical behavior. Additionally, size dependence studies have to be performed on the atomistic RVEs containing cross linked polymer to obtain the optimum size of the interfacial model necessary for continuum modeling. Predictions of the current research have led to new comparisons with experimental work. The interfacial peak shear traction evaluated for the graphene-polymer interface in this research was found comparable with that of the multi-walled carbon nanotube-polymer interface, measured experimentally from a pull out test. Additionally, the behavior of the polymer region during separation for both straight chain as well as cross linked polymer, as observed in the simulations in the present research, was consistent with a few experimental observations.

REFERENCES

[1] K. T. Lau and D. Hui, "The revolutionary creation of new advanced materials–carbon nanotube composites," *Composites Part B-Engineering*, vol. 33, no. 4, pp. 263–277, 2002.

[2] M. F. Yu, B. S. Files, S. Arepalli, and R. S. Ruoff, "Tensile loading of ropes of single wall carbon nanotubes and their mechanical properties," *Physical Review Letters*, vol. 84, no. 24, pp. 5552–5555, 2000.

[3] M. F. Yu, O. Lourie, M. J. Dyer, K. Moloni, T. F. Kelly, and R. S. Ruoff, "Strength and breaking mechanism of multiwalled carbon nanotubes under tensile load," *Science*, vol. 287, no. 5453, pp. 637–640, 2000.

[4] J. P. Salvetat, G. A. D. Briggs, J. M. Bonard, R. R. Bacsa, A. J. Kulik, T. Stockli, N. A. Burnham, and L. Forro, "Elastic and shear moduli of single-walled carbon nanotube ropes," *Physical Review Letters*, vol. 82, no. 5, pp. 944–947, 1999.

[5] A. Krishnan, E. Dujardin, T. W. Ebbesen, P. N. Yianilos, and M. M. J. Treacy, "Young's modulus of single-walled nanotubes," *Physical Review B*, vol. 58, no. 20, pp. 14 013–14 019, 1998.

[6] H. Rafii-Tabar, "Computational modelling of thermo-mechanical and transport properties of carbon nanotubes," *Physics Reports-Review Section of Physics Letters*, vol. 390, no. 4-5, pp. 235–452, 2004.

[7] M. Arroyo and T. Belytschko, "An atomistic-based finite deformation mem-

brane for single layer crystalline films," *Journal of the Mechanics and Physics of Solids*, vol. 50, no. 9, pp. 1941–1977, 2002.

[8] E.-S. Oh, J. C. Slattery, and D. C. Lagoudas, "Thermodynamics of two-dimensional, single component, elastic, crystalline solid: single-wall carbon nanotubes," *Philosophical Magazine*, vol. 85, no. 20, pp. 2249–2280, 2005.

[9] M. Meo and M. Rossi, "Prediction of young's modulus of single wall carbon nanotubes by molecular-mechanics based finite element modelling," *Composites Science and Technology*, vol. 66, no. 11-12, pp. 1597–1605, 2006.

[10] D. Sanchez-Portal, E. Artacho, J. M. Soler, A. Rubio, and P. Ordejón, "Ab initio structural, elastic, and vibrational properties of carbon nanotubes," *Physical Review B*, vol. 59, no. 19, pp. 12 678–12 688, 1999.

[11] E. Hernandez, C. Goze, P. Bernier, and A. Rubio, "Elastic properties of single-wall nanotubes," *Applied Physics A*, vol. 68, no. 3, pp. 287–292, 1999.

[12] K. N. Kudin, G. E. Scuseria, and B. I. Yakobson, "C_2F, BN, and C nanoshell elasticity from ab initio computations," *Physical Review B*, vol. 64, pp. 235 406 (1–10), 2001.

[13] G. M. Odegard, T. S. Gates, K. E. Wise, C. Park, and E. J. Siochi, "Constitutive modeling of nanotube-reinforced polymer composites," *Composites Science and Technology*, vol. 63, no. 11, pp. 1671–1687, 2003.

[14] C. Li and T.-W. Chou, "A structural mechanics approach for the analysis of carbon nanotubes," *International Journal of Solids and Structures*, vol. 40, no. 10, pp. 2487–2499, 2003.

[15] B. H. Bodily and C. T. Sun, "Structural and equivalent continuum properties of single-walled carbon nanotubes," *International Journal of Materials & Product Technology*, vol. 18, no. 4-6, pp. 381–397, 2003.

[16] S. Q. Zhu and X. Wang, "Effect of environmental temperatures on elastic properties of single-walled carbon nanotube," *Journal of Thermal Stresses*, vol. 30, no. 12, pp. 1195–1210, 2007.

[17] S. Komarneni, "Nanocomposites," *Journal of Materials Chemistry*, vol. 2, no. 12, pp. 1219–1230, 1992.

[18] B. Njuguna and K. Pielichowski, "Polymer nanocomposites for aerospace applications: Properties," *Advanced Engineering Materials*, vol. 5, no. 11, pp. 769–778, 2003.

[19] L. A. Goettler, K. Y. Lee, and H. Thakkar, "Layered silicate reinforced polymer nanocomposites: Development and applications," *Polymer Reviews*, vol. 47, no. 2, pp. 291–317, 2007.

[20] D. D. L. Chung, "Electrical applications of carbon materials," *Journal of Materials Science*, vol. 39, no. 8, pp. 2645–2661, 2004.

[21] Y. H. Hu, O. A. Shenderova, Z. Hu, C. W. Padgett, and D. W. Brenner, "Carbon nanostructures for advanced composites," *Reports on Progress in Physics*, vol. 69, no. 6, pp. 1847–1895, 2006.

[22] F. Hussain, M. Hojjati, M. Okamoto, and R. E. Gorga, "Review article: Polymer-matrix nanocomposites, processing, manufacturing, and application: An overview," *Journal of Composite Materials*, vol. 40, no. 17, pp. 1511–1575, 2006.

[23] E. V. Barrera, "Key methods for developing single-wall nanotube composites," *Journal of the Minerals Metals & Materials Society*, vol. 52, no. 11, pp. A38–A42, 2000.

[24] C. A. Dyke and J. M. Tour, "Solvent-free functionalization of carbon nanotubes," *Journal of the American Chemical Society*, vol. 125, no. 5, pp. 1156–1157, 2003.

[25] C. A. Dyke and J. M. Tour, "Covalent functionalization of single-walled carbon nanotubes for materials applications," *Journal of Physical Chemistry A*, vol. 108, no. 51, pp. 11 151–11 159, 2004.

[26] J. Zhu, H. Q. Peng, F. Rodriguez-Macias, J. L. Margrave, V. N. Khabashesku, A. M. Imam, K. Lozano, and E. V. Barrera, "Reinforcing epoxy polymer composites through covalent integration of functionalized nanotubes," *Advanced Functional Materials*, vol. 14, no. 7, pp. 643–648, 2004.

[27] P. R. Thakre, D. C. Lagoudas, Z. J., E. V. Barrera, and T. S. Gates, "Effect of functionalization and weight fraction of single walled carbon nanotubes on mechanical properties of epoxy nanocomposites," in *International Conference on Computational and Experimental Engineering Sciences (ICCES)*, December 1–7 2005.

[28] M. L. Shofner, V. N. Khabashesku, and E. V. Barrera, "Processing and mechanical properties of fluorinated single-wall carbon nanotube-polyethylene composites," *Chemistry of Materials*, vol. 18, no. 4, pp. 906–913, 2006.

[29] V. G. Hadjiev, D. C. Lagoudas, E. S. Oh, P. Thakre, D. Davis, B. S. Files, L. Yowell, S. Arepalli, J. L. Bahr, and J. M. Tour, "Buckling instabilities of oc-

tadecylamine functionalized carbon nanotubes embedded in epoxy," *Composites Science and Technology*, vol. 66, no. 1, pp. 128–136, 2006.

[30] D. C. Lagoudas, P. R. Thakre, and A. A. Benzerga, "Nanoindentation of cnt reinforced epoxy nanocomposites," in *Sixteenth European Conference on Fracture (ECF16)*, June 2006.

[31] P. R. Thakre, D. C. Lagoudas, J. Zhu, E. V. Barrera, and T. S. Gates, "Processing and characterization of carbon-fabric/epoxy composites," in *47th AIAA/ASME/ASCE/AHS/ASC Conference*, May 1-4 2006.

[32] D. C. Lagoudas and P. R. Thakre, "Investigation of swcnt's effect on interlaminar shear strength of carbon fabric composites," in *6th International Symposium on Advanced Composites*, May 16–18 2007.

[33] S. J. V. Frankland, V. M. Harik, G. M. Odegard, D. W. Brenner, and T. S. Gates, "The stress-strain behavior of polymer-nanotube composites from molecular dynamics simulation," *Composites Science and Technology*, vol. 63, no. 11, pp. 1655–1661, 2003.

[34] M. Griebel and J. Hamaekers, "Molecular dynamics simulations of the elastic moduli of polymercarbon nanotube composites," *Computer Methods in Applied Mechanics and Engineering*, vol. 193, pp. 1773–1788, 2004.

[35] R. Zhu, E. Pan, and A. K. Roy, "Molecular dynamics study of the stress-strain behavior of carbon-nanotube reinforced epon 862 composites," *Materials Science and Engineering A-Structural Materials Properties Microstructure and Processing*, vol. 447, no. 1-2, pp. 51–57, 2007.

[36] V. V. Mokashi, D. Qian, and Y. J. Liu, "A study on the tensile response

and fracture in carbon nanotube-based composites using molecular mechanics," *Composites Science and Technology*, vol. 67, no. 3-4, pp. 530–540, 2007.

[37] D. Qi, J. Hinkley, and G. W. He, "Molecular dynamics simulation of thermal and mechanical properties of polyimide-carbon-nanotube composites," *Modelling and Simulation in Materials Science and Engineering*, vol. 13, no. 4, pp. 493–507, 2005.

[38] G. D. Seidel, D. C. Lagoudas, S. J. V. Frankland, and T. S. Gates, "Modeling functionally graded interphase regions in carbon nanotube reinforced composites," in *American Society for Composites Technical Conference*, vol. 20, Drexel University, Philadelphia, PA, 2005.

[39] M. S. Al-Haik and M. Y. Hussain, "Molecular dynamics simulation of magnetic field induced orientation of nanotube-polymer composite," *Japanese Journal of Applied Physics Part 1-Regular Papers Brief Communications & Review Papers*, vol. 45, no. 11, pp. 8984–8987, 2006.

[40] Q. B. Zheng, Q. Z. Xue, K. O. Yan, L. Z. Hao, Q. Li, and X. L. Gao, "Investigation of molecular interactions between swnt and polyethylene/polypropylene/polystyrene/polyaniline molecules," *Journal of Physical Chemistry C*, vol. 111, no. 12, pp. 4628–4635, 2007.

[41] J. Gou, "Single-walled carbon nanotube bucky paper/epoxy composites: Molecular dynamics simulation and process development," Ph.D. in Industrial Engineering, The Florida State University, Tallahassee, FL, 2002.

[42] K. Liao and S. Li, "Interfacial characteristics of a carbon nanotube-polystyrene composite system," *Applied Physics Letters*, vol. 79, no. 25, pp. 4225–4227, 2001.

[43] Z. Y. Liang, J. H. Gou, C. Zhang, B. Wang, and L. Kramer, "Investigation of molecular interactions between (10,10) single-walled nanotube and epon 862 resin/detda curing agent molecules," *Materials Science and Engineering A-Structural Materials Properties Microstructure and Processing*, vol. 365, no. 1-2, pp. 228–234, 2004.

[44] J. H. Gou, Z. Y. Liang, C. Zhang, and B. Wang, "Computational analysis of effect of single-walled carbon nanotube rope on molecular interaction and load transfer of nanocomposites," *Composites Part B–Engineering*, vol. 36, no. 6, pp. 524–533, 2005.

[45] J. H. Gou, B. Minaie, B. Wang, Z. Y. Liang, and C. Zhang, "Computational and experimental study of interfacial bonding of single-walled nanotube reinforced composites," *Computational Materials Science*, vol. 31, no. 3-4, pp. 225–236, 2004.

[46] S. C. Chowdhury and T. Okabe, "Computer simulation of carbon nanotube pull-out from polymer by the molecular dynamics method," *Composites Part a-Applied Science and Manufacturing*, vol. 38, no. 3, pp. 747–754, 2007.

[47] S. Namilae, N. Chandra, and C. Shet, "Mechanical behavior of functionalized nanotubes," *Chemical Physics Letters*, vol. 387, no. 4-6, pp. 247–252, 2004.

[48] S. Namilae and N. Chandra, "Multiscale model to study the effect of interfaces in carbon nanotube-based composites," *Journal of Engineering Materials and Technology-Transactions of the ASME*, vol. 127, pp. 222–232, 2005.

[49] S. J. V. Frankland, A. Caglar, D. W. Brenner, and M. Griebel, "Molecular simulation of the influence of chemical cross-links on the shear strength of car-

bon nanotube-polymer interfaces," *Journal of Physical Chemistry B*, vol. 106, no. 12, pp. 3046–3048, 2002.

[50] S. J. V. Frankland and V. M. Harik, "Analysis of carbon nanotube pull-out from a polymer matrix," *Surface Science*, vol. 525, no. 1-3, pp. L103–L108, 2003.

[51] Y. J. Liu, N. Nishimura, D. Qian, N. Adachi, Y. Otani, and V. Mokashi, "A boundary element method for the analysis of cnt/polymer composites with a cohesive interface model based on molecular dynamics," *Engineering Analysis with Boundary Elements*, vol. In print, 2008.

[52] W. B. Lu, J. Wu, L. Y. Jiang, Y. Huang, K. C. Hwang, and B. Liu, "A cohesive law for multi-wall carbon nanotubes," *Philosophical Magazine*, vol. 87, no. 14-15, pp. 2221–2232, 2007.

[53] L. Y. Jiang, Y. Huang, H. Jiang, G. Ravichandran, H. Gao, K. C. Hwang, and B. Liu, "A cohesive law for carbon nanotube/polymer interfaces based on the van der waals force," *Journal of the Mechanics and Physics of Solids*, vol. 54, no. 11, pp. 2436–2452, 2006.

[54] H. Tan, L. Y. Jiang, Y. Huang, B. Liu, and K. C. Hwang, "The effect of van der waals-based interface cohesive law on carbon nanotube-reinforced composite materials," *Composites Science and Technology*, vol. 67, pp. 2941–2946, 2007.

[55] K. F. Mansfield and D. N. Theodorou, "Atomistic simulation of a glassy polymer graphite interface," *Macromolecules*, vol. 24, no. 15, pp. 4295–4309, 1991.

[56] K. C. Daoulas, V. A. Harmandaris, and V. G. Mavrantzas, "Detailed atomistic simulation of a polymer melt/solid interface: Structure, density, and conforma-

tion of a thin film of polyethylene melt adsorbed on graphite," *Macromolecules*, vol. 38, no. 13, pp. 5780–5795, 2005.

[57] H. X. Guo, X. Z. Yang, and T. Li, "Molecular dynamics study of the behavior of a single long chain polyethylene on a solid surface," *Physical Review E*, vol. 61, no. 4, pp. 4185–4193, 2000.

[58] V. A. Harmandaris, K. C. Daoulas, and V. G. Mavrantzas, "Molecular dynamics simulation of a polymer melt/solid interface: Local dynamics and chain mobility in a thin film of polyethylene melt adsorbed on graphite," *Macromolecules*, vol. 38, no. 13, pp. 5796–5809, 2005.

[59] H. Yang, Z. Y. Lu, Z. S. Li, and C. C. Sun, "A molecular-dynamics simulation study of diffusion of a single model carbonic chain on a graphite (001) surface," *Journal of Molecular Modeling*, vol. 12, no. 4, pp. 432–435, 2006.

[60] D. J. Henry, G. Yiapanis, E. Evans, and I. Yarovsky, "Adhesion between graphite and modified polyester surfaces: A theoretical study," *Journal of Physical Chemistry B*, vol. 109, no. 36, pp. 17 224–17 231, 2005.

[61] C. A. Cooper, S. R. Cohen, A. H. Barber, and H. D. Wagner, "Detachment of nanotubes from a polymer matrix," *Applied Physics Letters*, vol. 81, no. 20, pp. 3873–3875, 2002.

[62] D. Qian, E. C. Dickey, R. Andrews, and T. Rantell, "Load transfer and deformation mechanisms in carbon nanotube-polystyrene composites," *Applied Physics Letters*, vol. 76, no. 20, pp. 2868–2870, 2000.

[63] D. Qian and E. C. Dickey, "In-situ transmission electron microscopy studies

of polymer-carbon nanotube composite deformation," *Journal of Microscopy-Oxford*, vol. 204, pp. 39–45, 2001.

[64] D. E. Spearot, K. I. Jacob, and D. L. McDowell, "Non-local separation constitutive laws for interfaces and their relation to nanoscale simulations," *Mechanics of Materials*, vol. 36, no. 9, pp. 825–847, 2004.

[65] V. Yamakov, E. Saether, D. R. Phillips, and E. H. Glaessgen, "Molecular-dynamics simulation-based cohesive zone representation of intergranular fracture processes in aluminum," *Journal of the Mechanics and Physics of Solids*, vol. 54, no. 9, pp. 1899–1928, 2006.

[66] D. S. Dugdale, "Yielding of steel sheets containing slits," *Journal of the Mechanics and Physics of Solids*, vol. 8, pp. 100–104, 1960.

[67] G. I. Barenblatt, "The mathematical theory of equilibrium cracks in brittle fracture," *Advances in Applied Mechanics*, vol. 7, pp. 55–129, 1962.

[68] A. Needleman, "A continuum model for void nucleation by inclusion debonding," *Journal of Applied Mechanics*, vol. 54, pp. 525–531, 1987.

[69] M. Ortiz, "Microcrack coalescence and macroscopic crack growth initiation in brittle solids," *International Journal of Solids and Structures*, vol. 24, no. 3, pp. 231–250, 1988.

[70] V. Tvergaard, "Effect of fiber debonding in a whisker-reinforced metal," *Materials Science and Engineering a-Structural Materials Properties Microstructure and Processing*, vol. 125, no. 2, pp. 203–213, 1990.

[71] Y. J. Liu and X. L. Chen, "Evaluations of the effective material properties

of carbon nanotube-based composites using a nanoscale representative volume element," *Mechanics of Materials*, vol. 35, no. 1-2, pp. 69–81, 2003.

[72] G. D. Seidel and D. C. Lagoudas, "Micromechanical analysis of the effective elastic properties of carbon nanotube reinforced composites," *Mechanics of Materials*, vol. 35, pp. 884–907, 2006.

[73] D. C. Hammerand, G. D. Seidel, and D. C. Lagoudas, "Computational micromechanics of clustering and interphase effects in carbon nanotube composites," *Mechanics of Advanced Materials and Structures*, vol. 14, no. 4, pp. 277–294, 2007.

[74] I. N. Levine, *Quantum Chemistry*. Boston, MA: Allyn and Bacon Inc., 1983.

[75] D. Young, *Computational chemistry: A practical guide for applying techniques to real-world problems*. New York, NY: John Wiley & Sons, 2001.

[76] J. B. Foresman and A. Frisch, *Exploring Chemistry with Electronic Structure Methods*. Pittsburgh, PA: Gaussian Inc, 1996.

[77] P. Dauberosguthorpe, V. A. Roberts, D. J. Osguthorpe, J. Wolff, M. Genest, and A. T. Hagler, "Structure and energetics of ligand-binding to proteins - escherichia-coli dihydrofolate reductase trimethoprim, a drug-receptor system," *Proteins-Structure Function and Genetics*, vol. 4, no. 1, pp. 31–47, 1988.

[78] J. Tersoff, "New empirical approach for the structure and energy of covalent systems," *Physical Review B*, vol. 37, pp. 6991–7000, 1988.

[79] D. W. Brenner, "Empirical potential for hydrocarbons for use in simulation the chemical vapor deposition of diamond films," *Physical Review B*, vol. 42, pp. 9458–9471, 1990.

[80] D. W. Brenner, "The art and science of an analytic potential," *Physica Status Solidi (B)*, vol. 217, pp. 23–40, 2000.

[81] A. C. T. van Duin, S. Dasgupta, F. Lorant, and W. A. Goddard, "Reaxff: A reactive force field for hydrocarbons," *Journal of Physical Chemistry A*, vol. 105, no. 41, pp. 9396–9409, 2001.

[82] S. Namilae and N. Chandra, "Role of atomic scale interfaces in the compressive behavior of carbon nanotubes in composites," *Composites Science and Technology*, vol. 66, no. 13, pp. 2030–2038, 2006.

[83] S. C. Chowdhury and T. Okabe, "Computer simulation of carbon nanotube pull-out from polymer by the molecular dynamics method," *Composites Part a-Applied Science and Manufacturing*, vol. 38, no. 3, pp. 747–754, 2007.

[84] K. Chenoweth, A. C. T. van Duin, and W. A. Goddard, "Reaxff reactive force field for molecular dynamics simulations of hydrocarbon oxidation," *Journal of Physical Chemistry A*, vol. 112, no. 5, pp. 1040–1053, 2008.

[85] W. C. Swope, H. C. Andersen, P. H. Berens, and K. R. Wilson, "A computer-simulation method for the calculation of equilibrium-constants for the formation of physical clusters of molecules - application to small water clusters," *Journal of Chemical Physics*, vol. 76, no. 1, pp. 637–649, 1982.

[86] D. N. Theodorou and U. W. Suter, "Local-structure and the mechanism of response to elastic-deformation in a glassy polymer," *Macromolecules*, vol. 19, no. 2, pp. 379–387, 1986.

[87] S. S. Jang and W. H. Jo, "Yielding and plastic behavior of amorphous atactic

poly(oxypropylene): An atomistic modeling approach," *Abstracts of Papers of the American Chemical Society*, vol. 215, pp. U335–U335, 1998.

[88] C. F. Fan, T. Çağin, Z. M. Chen, and K. A. Smith, "Molecular modeling of polycarbonate .1. force-field, static structure, and mechanical-properties," *Macromolecules*, vol. 27, no. 9, pp. 2383–2391, 1994.

[89] K. Yashiro, T. Ito, and Y. Tomita, "Molecular dynamics simulation of deformation behavior in amorphous polymer: nucleation of chain entanglements and network structure under uniaxial tension," *International Journal of Mechanical Sciences*, vol. 45, no. 11, pp. 1863–1876, 2003.

[90] J. Rottler and M. O. Robbins, "Yield conditions for deformation of amorphous polymer glasses," *Physical Review E*, vol. 6405, no. 5, pp. 051 801–8, 2001.

[91] D. Brown and J. H. R. Clarke, "Molecular-dynamics simulation of an amorphous polymer under tension .1. phenomenology," *Macromolecules*, vol. 24, no. 8, pp. 2075–2082, 1991.

[92] P. H. Mott, A. S. Argon, and U. W. Suter, "Atomistic modeling of plastic-deformation of glassy-polymers," *Philosophical Magazine A – Physics of Condensed Matter Structure Defects and Mechanical Properties*, vol. 67, no. 4, pp. 931–978, 1993.

[93] D. N. Theodorou and U. W. Suter, "Atomistic modeling of mechanical-properties of polymeric glasses," *Macromolecules*, vol. 19, no. 1, pp. 139–154, 1986.

[94] S. Shenogin and R. Ozisik, "Simulation of plastic deformation in glassy poly-

mers: Atomistic and mesoscale approaches," *Journal of Polymer Science Part B-Polymer Physics*, vol. 43, no. 8, pp. 994–1004, 2005.

[95] J. Simons, *An Introduction to Theoretical Chemistry.* Cambridge, UK: Cambridge University Press, 2003.

[96] J. W. Ochterski, "Vibrational analysis in gaussian," Gaussian Inc, Wallingford, CT, Tech. Rep., 1999.

[97] M. Born and R. Oppenheimer, "Zur quantentheorie der molekeln (on the quantum theory of molecules)," *Annalen der Physik*, vol. 84, no. 20, pp. 457–484, 1927.

[98] M. Springborg, *Methods of Electronic-Structure Calculations: From Molecules to Solids.* England, UK: John Wiley & Sons, 2000.

[99] M. A. Ratner and G. C. Schatz, *An Introduction to Quantum Mechanics in Chemistry.* Upper Saddle River, NJ: Prentice Hall, 2000.

[100] E. P. Popov, *Mechanics of materials.* Upper Saddle River, NJ: Prentice Hall, 1952.

[101] M. Lucas and R. J. Young, "Effect of uniaxial strain deformation upon Raman radial breathing modes of single-wall carbon nanotubes in composites," *Physical Review B*, vol. 69, pp. 085 405–9, 2004.

[102] V. G. Hadjiev, M. N. Iliev, S. Arepalli, P. Nikolaev, and B. S. Files, "Raman scattering test of single-wall carbon nanotube composites," *Applied Physics Letters*, vol. 78, no. 21, pp. 3193–3195, 2001.

[103] R. A. Jishi, L. Venkataraman, M. S. Dresselhaus, and G. Dresselhaus, "Phonon modes in carbon nanotubules," *Chemical Physics Letters*, vol. 209, no. 1-2, pp. 77–82, 1993.

[104] G. Dresselhaus, M. S. Dresselhaus, and R. Saito, *Physical properties of carbon nanotubes*. London, UK: World Scientific Publishing Company Inc., 2003.

[105] V. N. Popov, "Lattice dynamics of single-walled boron nitride nanotubes," *Physical Review B*, vol. 67, no. 8, p. 085408, 2003.

[106] A. M. Rao, E. Richter, S. Bandow, B. Chase, P. C. Eklund, K. A. Williams, S. Fang, K. R. Subbaswamy, M. Menon, A. Thess, R. E. Smalley, G. Dresselhaus, and M. S. Dresselhaus, "Diameter-selective raman scattering from vibrational modes in carbon nanotubes," *Science*, vol. 275, pp. 187–191, 1997.

[107] G. Gao, T. Çağin, and W. A. I. Goddard, "Energetics, structure, mechanical and vibrational properties of single-walled carbon nanotubes," *Nanotechnology*, vol. 9, no. 3, pp. 184–191, 1998.

[108] S. Plimpton, "Fast parallel algorithms for short-range molecular-dynamics," *Journal of Computational Physics*, vol. 117, no. 1, pp. 1–19, 1995.

[109] A. H. Barber, S. R. Cohen, and H. D. Wagner, "Measurement of carbon nanotubepolymer interfacial strength," *Applied Physics Letters*, vol. 82, no. 23, pp. 4140–4142, 2003.

[110] A. H. Barber, S. R. Cohen, A. Eitan, L. S. Schadler, and H. D. Wagner, "Fracture transitions at a carbon-nanotube/polymer interface," *Advanced Materials*, vol. 18, pp. 83–87, 2006.

[111] Z. Q. Zhang, B. Liu, Y. L. Chen, H. Jiang, K. C. Hwang, and Y. Huang, "Mechanical properties of functionalized carbon nanotubes," *Nanotechnology*, vol. 19, no. 39, pp. 395 702(1–6), 2008.

[112] Accelrys, "M. S. Modeling," San Diego, CA, 2004.

[113] Accelrys, "Cerius² Modeling Environment," San Diego, CA, 2003.

[114] W. Humphrey, A. Dalke, and K. Schulten, "VMD: Visual Molecular Dynamics," *Journal of Molecular Graphics*, vol. 14, no. 1, pp. 33–38, 1996.

[115] W. G. Hoover, "Canonical dynamics - equilibrium phase-space distributions," *Physical Review A*, vol. 31, no. 3, pp. 1695–1697, 1985.

[116] R. de Borst, "Fracture in quasi-brittle materials: a review of continuum damage-based approaches," *Engineering Fracture Mechanics*, vol. 69, no. 2, pp. 95–112, 2002.

[117] M. P. Allen and D. J. Tildsley, *Computer simulation of liquids.* New York, NY: Oxford University Press Inc., 1987.

APPENDIX A

EVALUATION OF HESSIAN MATRIX FROM MODAL SYNTHESIS

This appendix describes the procedure of modal synthesis, wherein the Hessian matrix for a linear mass-spring system is evaluated utilizing the corresponding mass matrix, the vibrational frequencies and the mode shapes obtained from the free vibration behavior.

Consider an N mass (atoms) system, free to vibrate in three-dimensional space. Let the displacement vector corresponding to the modal shape $\{\psi^\alpha\}$ be

$$\mathbf{u}^\alpha = e^{i\omega^\alpha t}\{\psi^\alpha\}, \qquad \alpha = 1, 2, \cdots, 3N, \tag{A.1}$$

where ω^α is the natural frequency corresponding to $\{\psi^\alpha\}$. Substituting eq. A.1 into eq. 3.2 with zero force ($\mathbf{F} = \{\mathbf{0}\}$), yeilds

$$\left(-(\omega^\alpha)^2[\mathbf{M}] + [\mathsf{K}]\right)\{\psi^\alpha\} = \{\mathbf{0}\}. \tag{A.2}$$

Pre-multiplying by $\{\psi^\beta\}^{\mathrm{T}}$, eq. A.2 is written as

$$\{\psi^\beta\}^{\mathrm{T}}\left(-(\omega^\alpha)^2[\mathbf{M}] + [\mathsf{K}]\right)\{\psi^\alpha\} = 0. \tag{A.3}$$

Similarly,

$$\{\psi^\alpha\}^{\mathrm{T}}\left(-(\omega^\beta)^2[\mathbf{M}] + [\mathsf{K}]\right)\{\psi^\beta\} = 0. \tag{A.4}$$

Transposing eq. A.4 and subtracting from eq. A.3, taking into account that $[\mathbf{M}]$ and $[\mathsf{K}]$ are symmetric, leads to

$$\left((\omega^\alpha)^2 - (\omega^\beta)^2\right)\{\psi^\beta\}^{\mathrm{T}}[\mathbf{M}]\{\psi^\alpha\} = 0. \tag{A.5}$$

It is clear from eq. A.5 that

$$\{\psi^\beta\}^\mathrm{T}[\mathbf{M}]\{\psi^\alpha\} = 0, \qquad \text{for } \alpha \neq \beta, \tag{A.6}$$

$$\{\psi^\beta\}^\mathrm{T}[\mathbf{M}]\{\psi^\alpha\} \equiv \tilde{m}^\alpha, \qquad \text{for } \alpha = \beta. \tag{A.7}$$

Using eq. A.3 and eq. A.6 yields

$$\{\psi^\beta\}^\mathrm{T}[\mathsf{K}]\{\psi^\alpha\} = 0, \qquad \text{for } \alpha \neq \beta, \tag{A.8}$$

$$\{\psi^\beta\}^\mathrm{T}[\mathsf{K}]\{\psi^\alpha\} = \tilde{m}^\alpha \omega^{\alpha 2}, \qquad \text{for } \alpha = \beta, \tag{A.9}$$

which can be written in a condensed form as

$$[\boldsymbol{\Psi}]^\mathrm{T}[\mathsf{K}][\boldsymbol{\Psi}] \equiv [\mathcal{K}], \tag{A.10}$$

where $[\boldsymbol{\Psi}]$ is the modal matrix containing all the mode shapes as columns,

$$[\boldsymbol{\Psi}] = [\{\psi^1\}, \{\psi^2\}, \{\psi^3\}, \cdots, \{\psi^{3N}\}], \tag{A.11}$$

and

$$\mathcal{K}_{ij} = 0, \qquad \text{for } i \neq j, \tag{A.12}$$

$$\mathcal{K}_{ij} = \tilde{m}^i (\omega^i)^2, \qquad \text{for } i = j. \tag{A.13}$$

Since $[\boldsymbol{\Psi}]$ is orthonormal, it follows from eq. A.10 that

$$[\mathsf{K}] \equiv [\boldsymbol{\Psi}][\mathcal{K}][\boldsymbol{\Psi}]^\mathrm{T}. \tag{A.14}$$

APPENDIX B

EQUIVALENCE OF ENERGY AND HESSIAN METHODS

Consider a SWCNT oriented along the z axis with the origin of coordinate system located at the center of one of its ends. Imposing axial stretch on the SWCNT in the z direction gives the following displacement field

$$u_z^p = \epsilon z^p, \tag{B.1}$$

$$u_x^p = -\nu\epsilon x^p, \text{and} \tag{B.2}$$

$$u_y^p = -\nu\epsilon y^p, \tag{B.3}$$

where ϵ is the nominal strain, u_x^p, u_y^p, and u_z^p are respectively the x, y and z components of the pth atom and $p = 1 \ldots N$, N is the number of atoms in the SWCNT. Differentiating eq. B.1 with respect to u_z^p gives

$$\frac{\partial \epsilon}{\partial u_z^p} = \frac{1}{z^p}. \tag{B.4}$$

Re-arranging eq. 3.8,

$$\frac{\partial^2 \Phi}{\partial \epsilon^2} = V_0 Y. \tag{B.5}$$

Integrating this expression with respect to ϵ gives

$$\frac{\partial \Phi}{\partial \epsilon} = V_0 Y \epsilon + c_1, \tag{B.6}$$

where c_1 is a constant. At equilibrium, described by $\epsilon = 0$, the potential energy is a minimum and therefore the first derivative is zero, which results in $c_1 = 0$. Integrating once more with respect to ϵ gives

$$\Phi = \frac{1}{2}V_0 Y \epsilon^2 + c_2, \tag{B.7}$$

which represents the assumed quadratic nature of the potential energy near equilibrium. Integrating eq. 3.1 with respect to u_i^p, gives

$$\frac{\partial \Phi}{\partial u_i^p} = \mathsf{K}_{ij}^{pq} u_j^q + c_3. \tag{B.8}$$

In this expression, $\frac{\partial \Phi}{\partial u_i^p} = \mathsf{f}_i^p$ which represents the ith component of force on the pth atom ($i = x, y, z$ and p=1...N), and $c_3 = 0$ as dictated by equilibrium, which assumes zero forces for zero displacements for an elastic body. This gives,

$$\frac{\partial \Phi}{\partial u_i^p} = \mathsf{K}_{ij}^{pq} u_j^q \tag{B.9}$$

The z component of force on an atom p that lies at the edge of the SWCNT, given as f_z^p can be written using eq. B.7, as

$$\mathsf{f}_z^p = \frac{\partial \Phi}{\partial u_z^p} = \frac{\partial}{\partial u_z^p} \left(\frac{1}{2} V_0 Y \epsilon^2 + c_2 \right) \tag{B.10}$$

$$= V_0 Y \epsilon \frac{\partial \epsilon}{\partial u_z^p}. \tag{B.11}$$

Using eq. B.4, this can be rewritten as

$$\mathsf{f}_z^p = V_0 Y \epsilon \frac{1}{z^p}. \tag{B.12}$$

f_z^p can also be expressed using the atomistic Hessian matrix using eq. B.9, as

$$\mathsf{f}_z^p = \frac{\partial \Phi}{\partial u_z^p} = \mathsf{K}_{zj}^{pq} u_j^q. \tag{B.13}$$

Using the expression for f_z^p from eqs. B.12 and B.13 we have

$$\mathsf{f}_z^p = \frac{\partial \Phi}{\partial u_z^p} = \mathsf{K}_{zj}^{pq} u_j^q = V_0 Y \epsilon \frac{1}{z^p}. \tag{B.14}$$

Dividing by the area of cross-section A to get the axial traction T_z

$$T_z = \frac{\mathsf{f}_z^p}{A} = \frac{\mathsf{K}_{zj}^{pq} u_j^q}{A} = \frac{1}{A} V_0 Y \epsilon \frac{1}{z^p}. \tag{B.15}$$

The un-deformed volume $V_0 = Az^p$, therefore eq. B.16 can be written as

$$T_z = \frac{\mathsf{K}_{zj}^{pq} u_j^q}{A} = Y\epsilon, \tag{B.16}$$

which gives the linear elastic stiffness in extension

$$\frac{T_z}{\epsilon} = \frac{\mathsf{K}_{zj}^{pq} u_j^q}{A\epsilon} = Y. \tag{B.17}$$

Hence, theoretically, the energy method and the atomistic Hessian matrix based method are equivalent in evaluating the linear elastic stiffness in extension.

APPENDIX C

PREPARATION OF AMORPHOUS POLYMER STRUCTURE

To equilibrate the polymer at chosen temperature and pressure conditions, the methodology of [88] was adopted. In this method, a periodic model of the polymer at very low density is utilized as the starting structure. Temperature annealing cycles, interspersed with volume shrinkage steps cause the polymer model to undergo structural transitions. This is followed by dynamic equilibration of the model at the required temperature and pressure conditions for sufficient time, finally providing the necessary equilibrated sample. The polymer chosen was polyethylene (PE), having the structure $CH_3-(CH_2)_n-CH_3$, where n was taken to be 60.

The polymer chains were prepared using the polymer builder in MS Modeling [112] which was given the amorphous structure using the Amorphous Cell module in MS Modeling, starting with 8 straight chains of $CH_3-(CH_2)_{60}-CH_3$. The total number of atoms in the amorphous 3D periodic structure was 1456. These chains were enclosed in a periodic box with a prescribed starting density of 0.60g/cm^3. Charge Equilibration module in Cerius^2 [113] was used to equilibrate the charges in the model. The velocity-Verlet integration algorithm was employed for performing all of the dynamics runs and energy minimization was carried out using the Hessian-free truncated Newton method in LAMMPS. Fig. 56 shows the periodic structure of PE as modeled in molecular dynamics. The locations of individual atoms are represented by unique Cartesian coordinates in a simulation box and the periodicity of the structure is managed by the lattice constants of the box. For the atoms that fall outside of the unit cell (simulation box), a periodic image is replicated by utilizing the periodicity on the opposite side of the box, such that they fall inside
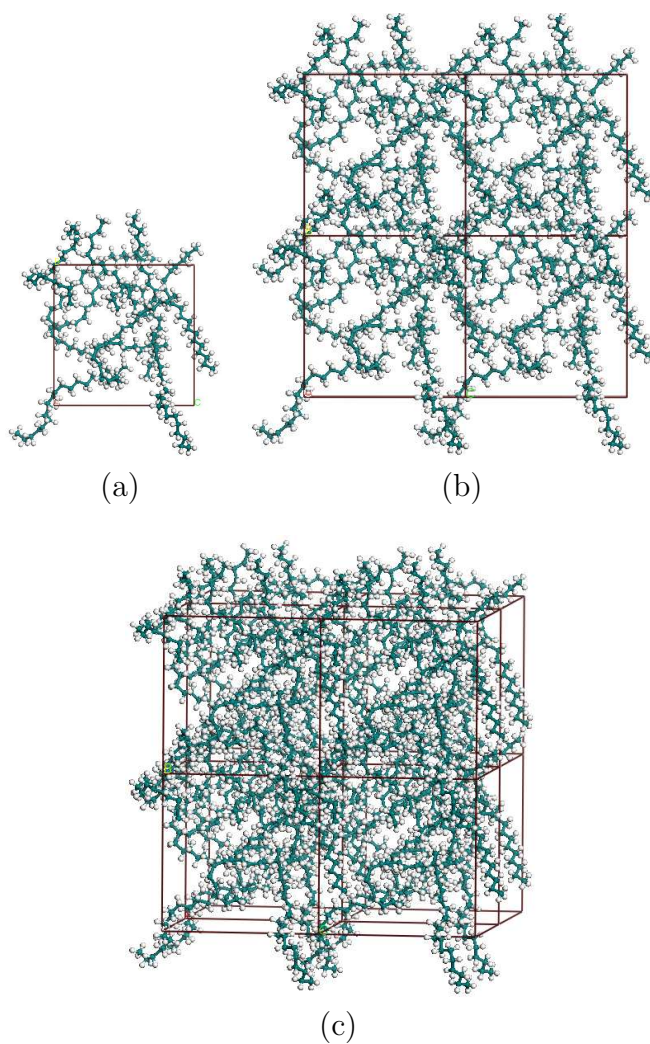
Fig. 56.: Periodic unit cell of amorphous polyethylene (PE), 56a: 3D periodic repeating unit, 56b: unit cell replicated in two directions and 56c: orthographic projection of the unit cell replicated by two cells in all three directions.

the simulation box. Similarly, during the course of MD simulation, any atoms that drift outside the unit cell, get represented inside the simulation box by utilizing the periodicity. Periodicity ensures that the total number of atoms are always conserved during the course of the simulation, as none of the atoms fall outside the unit cell. The main objective of utilizing periodicity is that, studies can be performed to represent properties of a bulk material. However, careful consideration must be given on the choice of the size of the system. For example, a periodic dimension smaller than the MD cutoff parameter will produce infinite images of all the constituent atoms. The size of the periodic box should be sufficiently large such that the effect of periodic edges is reduced to a minimum; such studies have been described in Sect. 1.
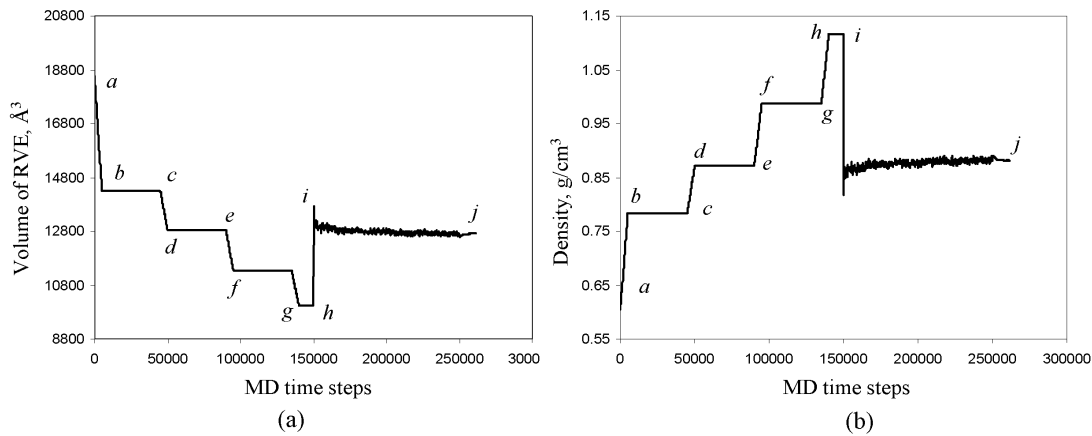
Fig. 57.: Volume and density equilibration. (a-b), (c-d), (e-f) and (g-h) are volume shrinkage steps; (b-c), (d-e), (f-g) and (h-i) are NVT equilibration steps; (i-j) is the NPT step giving the final volume.

PE was chosen to be equilibrated at a temperature of 100K, (which is well below its glass transition temperature (T_g) of about room temperature), and pressure of 1 atmosphere, which is about room-pressure. Annealing was performed by alternatively raising the temperature to 600K, well above the T_g and bringing it back to 100K. The

process of annealing followed by equilibration is shown in Fig. 57a and Fig. 57b. Point a represents the starting structure at a density of 0.60 g/cm³ which was subjected to volume shrinkage under the NVT ensemble, keeping the temperature at 100K. The volume was reduced by shrinking all sides of the rectangular periodic box by equal amounts at a uniform rate (point b) and the structure was minimized for energy. Point b – point c represents constant volume annealing, wherein the sample was subjected to two cycles of 600K and back to 100K. This was followed by volume reduction and subsequent energy minimization of the structure (point c – point d). This process of volume reduction and temperature annealing was carried out to a point little beyond the equilibrium density, where large fluctuations in temperature and pressure were noticed (point i). To obtain the desired structure, the NPT ensemble was employed at point i, prescribing the temperature to be 100K and pressure to be 1 atmosphere. This was carried out for a long time and is represented by point j at which it was assumed that the polymer was in equilibrium with the chosen conditions of temperature and pressure. At the end of the equilibration, the lattice parameter for each side of the periodic box had an average dimension of 23.34Å and the density stabilized at about 0.88g/cm². It should be noted that the density arising from this equilibration process may not exactly match experimental data (0.88 – 1.6g/cm² for PE), because the simulations ideally deal with a material free from mechanical defects. The simulations are also affected by the size of the computational domain and accuracy of the parametrization in the potential (force-field). Charge equilibration may also introduce errors. Nevertheless, we perform the bulk tests and separation tests on this sample as a first approximation.

Tensile test: uniaxial loading with stepwise deformation

Tensile tests were carried out by loading the polymer along one of the axes. This was done by extending the length of the box size in steps of 0.25% longitudinal strain. Along other directions, the pressure was kept fixed at a very low level of 1 atm (Fig. 58). The system was re-minimized, keeping the box size temporarily fixed, and then subjected to a long dynamics run at constant temperature to equilibrate the stresses. In all the simulations, the stresses were calculated by the virial definition [117].

This process of straining the box was re-performed over a few strain levels, with the incremental value of 0.25%. Fig. 58 shows the last 20ps of the dynamics run vs. the tensile stress in the system for a few strain levels. The average of the 20ps stress response is used to graph the inset in Fig. 58. The slope, obtained by curve fitting this response provides the estimate of the Young's Modulus E_Y of the polymer. The value hence calculated is about 2GPa. Experimentally, PE exhibits a Young's Modulus in the range 0.8GPa-1.6GPa.

Volumetric deformation tests

This exercise was carried out to evaluate the bulk modulus of the polymer. The sample was compressed and expanded hydrostatically to measure the volumetric response. The procedure is shown in Fig. 59 where the computational domain was subjected to equal tensile and compressive pressures on all the faces. The tensile and compressive loading conditions were incrementally applied one at a time, starting with room pressure conditions. In the given description, pressure was assumed to be negative for compressive loading and positive for tensile. In the simulations, the system was allowed to equilibrate for 10ps at a fixed pressure. The temperature was
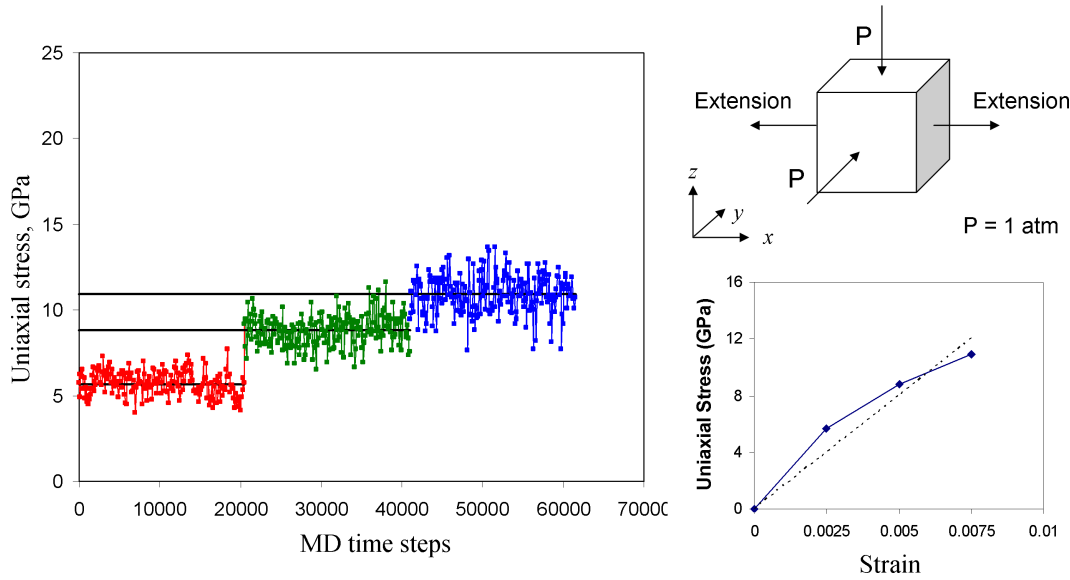
Fig. 58.: Uniaxial tensile test with stepwise deformation.

kept at 100K as before. It was observed that the density decreased with application of tensile pressure and increased for the case of compressive. To evaluate the bulk modulus, the following relationship was used:

$$K = -\rho \left(\frac{\partial p}{\partial \rho} \right) \tag{C.1}$$

where ρ is the equilibrium value of density at room pressure and given temperature (100K). The linear part of the response, approximated as the line AB in Fig. 59 was used to provide the slope at small deformation. Using the equilibrium value of density ρ as $0.88\mathrm{g/cm}^2$, the bulk modulus was evaluated to be about 7.5GPa.

Experimentally, PE exhibits a bulk modulus of about 3Gpa. The procedure we used here was similar to [88] in which a similar discrepancy between the theoretical and experimental values of bulk properties is mentioned. The main reason is attributed to the fact that in MD we are using a defect free system whereas a real sample may consist of several inhomogeneities that cannot be fully captured by the
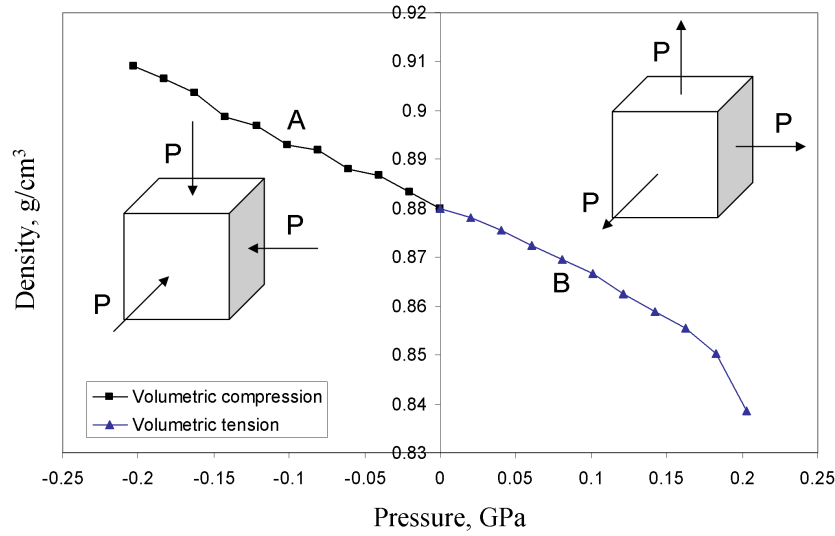
Fig. 59.: Volumetric extension and compression tests and evaluation of bulk modulus near the linear regime.

MD tests.

Assuming that the polymer sample be isotropic, using the values of Young's modulus and bulk modulus, the Poisson's ratio can be evaluated using

$$\nu = \frac{3K - E}{6K} \tag{C.2}$$

as 0.46.

The calculation of equilibrium density and investigation of mechanical tests gives us a confidence over the simulations, since they predict properties which are the same order of magnitude as experimental results. This is important, as the later investigation of interface properties will have significant credibility. This is attributed to the full force field that was as well as stepwise deformation method that was chosen for all the simulations.

APPENDIX D

EQUILIBRATION OF INTERFACIAL SYSTEM
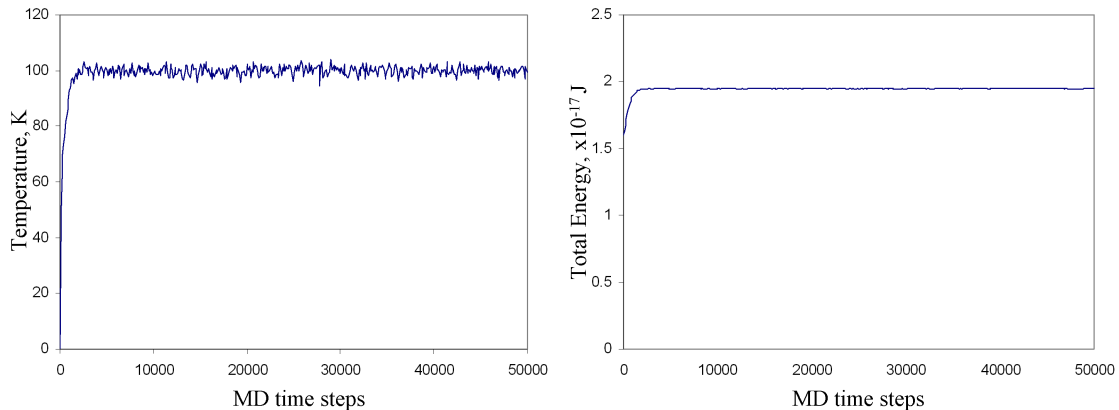
Fig. 60.: Temperature and energy profiles for interfacial system, during dynamical equilibration.

After introducing the graphene layer adjacent to the polymer, the graphene-polymer system was statically equilibrated (energy minimization at 0K), and thereafter subjected to dynamic equilibration at 100K. Fig. 60 shows the temperature and energy profiles for the graphene-polymer system monitored up to 50,000 MD steps which actually represent 50 picoseconds in real-time (a single MD step is 1 femtosecond in duration). It can be inferred that the system reached a steady state at the end of 50 picoseconds and could be used to perform separation tests. Moreover, the trends indicate that the system had already equilibrated within the first 10 picoseconds (10,000 MD steps). Therefore, subsequent MD simulations of separation were carried out for 10 picoseconds only.

APPENDIX E

CVFF PARAMETERS

Table XII.: CVFF parameters used in the graphene-polymer system

Masses		
Atom	Atomic Mass (amu)	
C	12.011150	
H	1.007970	
Bond Parameters		
Bond type	r_0	K_B
	(Å)	(Kcal/mole)
C-H (PE)[1]	1.105	340.6175
C-C (PE)	1.526	322.7158
C-C (graphene)	1.3400	480.0000
Angle Parameters		
Angle type	θ_0	K_A
	(degrees)	(Kcal/mole)
C-C-C (PE)	110.5	46.6
H-C-C (PE)	110.0	44.4
H-C-H (PE)	106.4	39.5
C-C-C (graphene)	120.0	90.0
Torsion Parameters		
Angle type	ϕ_0 $\quad$ n	K_T
	(degrees)	(Kcal/mole)
–C–C– (PE)	0 $\quad$ 3	0.158
–C–C– (graphene)	180 $\quad$ 2	3.000
Van der Waals Parameters		
Atom type	A	B
C(PE)	1,981,049.2250	1,125.99800
H(PE)	7,108.4660	32.87076
C(graphene)	2,968,753.3590	1,325.70810
Cut-off distance in all simulations = 10Å		

LAMMPS uses the Van der Waals energy expression $E_{pair_{VDW}} = 4\epsilon \left[\left(\frac{\sigma}{r} \right)^{12} - \left(\frac{\sigma}{r} \right)^6 \right]$. Expressing σ and ϵ in terms of CVFF parameters (refer 2.4): $\sigma = \left(\frac{A_i A_j}{B_i B_j} \right)^{1/12}$ and $\epsilon = \frac{1}{4} \frac{B_i B_j}{\sqrt{A_i A_j}}$.

---

[1]Polyethylene

APPENDIX F

PREPARATION OF NETWORK POLYMER STRUCTURE

In this section, details are presented pertaining to the the preparation of network polyethylene (PE). The network polymer described here is a 3D structure of cross linked PE. A schematic is shown in Fig. 61 which is a 2D projection of the 3D structure, shown for clarity.
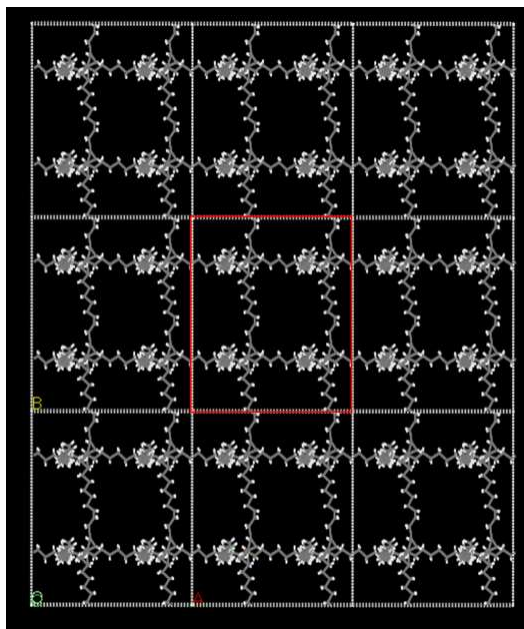
Fig. 61.: Schematic of network polymer.

The whole structure consists of a periodically repeating unit, shown in the boxed frame which is a 3D periodic unit. To create this periodic unit, we begin with two horizontal straight chains of PE. These chains were cross linked by adding two vertical PE chains. This structure was repeated in the plane of the figure to generate an additional set of cross linked chains similar to the first one. The two sets were

joined by PE chains to create a 3D network. In order to make the whole structure periodic, additional chains were added to the structure at the junction atoms such that periodicity was ascertained. The resulting 3D periodic structure was replicated in all the 3 directions to obtain the final structure is shown in Fig. 62.
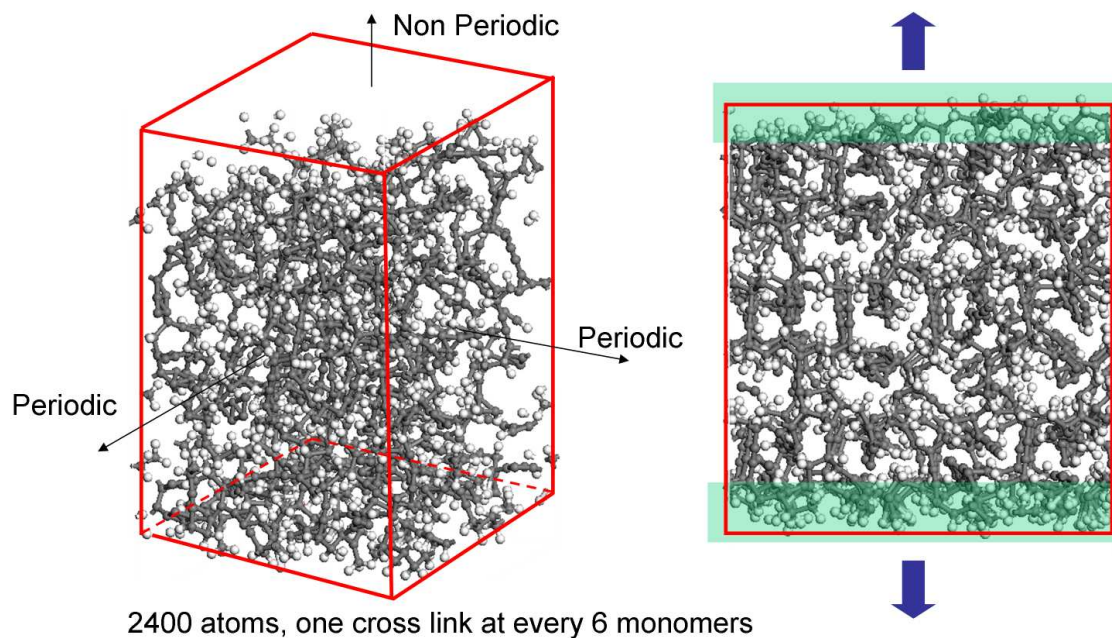
Fig. 62.: Network polyethylene in 3D periodic geometry.

This structure consisted of about 2400 atoms and had one cross link at every 6 monomer units.

APPENDIX G

REAXFF FORCE FIELD PARAMETERS

Table XIII.: ReaxFF force field file used by LAMMPS. Set I.

Serial No.	Description	Parameter
1	Overcoordination parameter	50.0000
2	Overcoordination parameter	9.5469
3	Valency angle conjugation parameter	127.8302
4	Triple bond stabilisation parameter	3.0000
5	Triple bond stabilisation parameter	6.5000
6	C2-correction	0.0000
7	Undercoordination parameter	1.0496
8	Triple bond stabilisation parameter	9.0000
9	Undercoordination parameter	11.5054
10	Undercoordination parameter	13.4059
11	Triple bond stabilization energy	0
12	Lower Taper-radius	0
13	Upper Taper-radius	10
14	Not used	2.8793
15	Valency undercoordination	33.8667
16	Valency angle/lone pair parameter	7.0994
17	Valency angle	1.0563
18	Valency angle parameter	2.0384
19	Not used	6.1431
20	Double bond/angle parameter	6.929
21	Double bond/angle parameter: overcoord	0.3989
22	Double bond/angle parameter: overcoord	3.9954
23	Not used	-2.4837
24	Torsion/BO parameter	5.7796
25	Torsion overcoordination	10
26	Torsion overcoordination	1.9487
27	Conjugation 0 (not used)	-1.2327
28	Conjugation	2.1645
29	vdWaals shielding	1.5591
30	Cutoff for bond order (*100)	0.1
31	Valency angle conjugation parameter	2.0038
32	Overcoordination parameter	0.6121
33	Overcoordination parameter	1.2172
34	Valency/lone pair parameter	1.8512
35	Not used	0.5
36	Not used	20
37	Molecular energy (not used)	5
38	Molecular energy (not used)	0
39	Valency angle conjugation parameter	3.6942

Table XIV.: ReaxFF force field file used by LAMMPS. Set II.

	cov.r	valency	a.m	Rvdw	Evdw	gammaEEM	cov.r2	# alfa
	gammavdW	valency	Eunder	Eover	chiEEM	etaEEM	n.u.cov r3	Elp
	Heat inc.	n.u.	n.u.	n.u.	n.u.ov/un	val1	n.u.	val3,vval4
C	1.3763	4	12	1.8857	0.1818	0.8712	1.2596	4
	9.5928	2.0784	4	22.6732	79.5548	5.7254	6.9235	0

	1.2065	0	-0.8579	4.9417	28.3475	11.9957	0.8563	0
	-2.8846	4.159	1.0564	4	2.9663	0	0	0
H	0.6646	1	1.008	1.603	0.06	0.7625	-0.1	1
	9.3951	4.4187	1	0	121.125	3.8196	9.8832	1
	-0.1	0	-0.1339	3.5803	2.8733	1	1.0698	0
	-13.0615	3.0626	1.0338	1	2.8793	0	0	0

Table XV.: ReaxFF force field file used by LAMMPS. Set III.

	Edis1 LPpen n.u. pbe1 pbo5 13corr pbo6 pbe2 pbo3 pbo4 n.u. pbo1 pbo2 ovcorr
C C	145.4070 103.0681 73.7841 0.2176 -0.7816 1.0000 28.4167 0.3217 0.1111 -0.1940 8.6733 1.0000 -0.0994 5.9724 1.0000 0.0000
C H	167.1752 0.0000 0.0000 -0.4421 0.0000 1.0000 6.0000 0.5969 17.4194 1.0000 0.0000 1.0000 -0.0099 8.5445 0.0000 0.0000
H H	188.1606 0.0000 0.0000 -0.3140 0.0000 1.0000 6.0000 0.6816 8.6247 1.0000 0.0000 1.0000 -0.0183 5.7082 0.0000 0.0000

Table XVI.: ReaxFF force field file used by LAMMPS. Set IV.

	Ediss	Ro	gamma	rsigma	rpi	rpi2
C H	0.0455	1.7218	10.4236	1.0379	-1.0000	-1.0000

Table XVII.: ReaxFF force field file used by LAMMPS. Set V.

	Thetao	o	ka	kb	pv1	pv2	
C C C	70.0265	13.6338	2.1884	0.0000	0.1676	26.3587	1.0400
C C H	69.7786	10.3544	8.4326	0.0000	0.1153	0.0000	1.0400
H C H	74.6020	11.8629	2.9294	0.0000	0.1367	0.0000	1.0400
C H H	0.0000	0.0000	6.0000	0.0000	0.0000	0.0000	1.0400
C H C	0.0000	3.4110	7.7350	0.0000	0.0000	0.0000	1.0400
H H H	0.0000	27.9213	5.8635	0.0000	0.0000	0.0000	1.0400

Table XVIII.: ReaxFF force field file used by LAMMPS. Set VI.

	V1	V2	V3	V2(BO)	vconj	n.u	n
C C C C	0.0000	23.2168	0.1811	-4.6220	-1.9387	0.0000	0.0000
C C C H	0.0000	45.7984	0.3590	-5.7106	-2.9459	0.0000	0.0000
H C C H	0.0000	44.6445	0.3486	-5.1725	-0.8717	0.0000	0.0000
ϕ C H ϕ	0.0000	0.0000	0.0000	0.0000	0.0000	0.0000	0.0000
ϕ H H ϕ	0.0000	0.0000	0.0000	0.0000	0.0000	0.0000	0.0000

VITA

Amnaya P. Awasthi

Materials Science and Engineering

3003 TAMU

Texas A&M University

College Station, TX 77843 USA

Amnaya P. Awasthi is a native of the state Uttar Pradesh in India. He got his B. Tech. degree in mechanical engineering from Indian Institute of Technology Guwahati in the year 2000. During his bachelor studies he performed research on the vibration behavior of helicopter blades and co-authored the B. Tech. Project Report entitled *Free Vibration Analysis of a Rotating Shear Deformable Composite Beam* under the guidance of Dr. Naresh Chandiramani. He worked on the finite element analysis of helicopter blades as a Research Associate in the Department of Aerospace Engineering at Indian Institute of Technology Kanpur for a year after his graduation. He joined the Materials Science and Engineering program at Texas A&M University in 2004 and developed a broad interest in atomistic modeling of carbon nanotubes and interfaces in nanocomposites. He has experience with computational chemistry based tools that are currently utilized for analyzing the mechanical behavior in these nanosystems. His interests include molecular dynamics and quantum mechanical atomistic simulations, analysis of nanoscale interface behavior, multiscale modeling of nanocomposite properties and development of cohesive laws for nanocomposites. He got his doctoral degree in materials science and engineering at Texas A&M University in December 2009. The current curriculum vitae of Amnaya containing updated publications and conference presentations can be obtained by emailing him at Amnaya@gmail.com.